Dissertation

Classical molecular dynamics simulations of carbon nanomembranes using LAMMPS

Methods for mechanical properties, internal structure and permeation studies

by

Julian Ehrens

submitted to

University of Bielefeld

Faculty of Physics

in partial fulfillment of the requirements for the degree of
doctor rerum naturalium
(Dr. rer. nat.)
on October 21, 2021

Advisor &   1. Reviewer: Prof. Dr. Jürgen Schnack
2. Reviewer: Prof. Dr. Armin Gölzhäuser

"We always find a way
To free ourselves from yesterday
Love, lies, then anger faint
The silence, it vibrates
In the end we are human
Lost in illusions
But forever we move on
Forever we move on"

Phuture Noize,
A Fantastic Vibration

Contents

Abbreviations

2D Two-dimensional
3D Three-dimensional

ACC All-carbon capacitor
AFM Atomic force microscopy
AIREBO Advanced interatomic reactive empirical bond order
AMBER Assisted model building with energy refinement

BE Binding energy
BPT 1,1'-Biphenyl-4-thiol, biphenylthiol

CNM Carbon nanomembrane
CNT Carbon nanotube
CP-AFM Conductive probe atomic force microscopy
CPU Central processing unit
CPUh CPU hours (total time spent on all CPUs)

DFS Depth first search
DFT Density functional theory

EDIP Environment dependent interatomic potential
EGaIn Eutectic Ga-In

FEM Finite-element method

GAP Gaussian approximation potential

HIM Helium ion microscopy
HREELS High resolution electron energy loss spectroscopy

IR Infrared
IRRAS Infrared reflection absorption spectroscopy

KE Kinetic energy

LAMMPS Large atomic/molecular massively parallel simulator
LRZ Leibniz Rechenzentrum

MD Molecular dynamics

NBPT 4'-nitro-1,1'-biphenyl-4-thiol
NEXAFS Near edge X-Ray absorption fine structure
NPH Isothermal-isenthalpic ensemble
NPT Isothermal-isobaric ensemble
NPTH 2-Naphthalenethiol, napthalenethiol

NVE Microcanonical ensemble
NVT Canonical ensemble

ODT 1-Octadecanethiol
OPLS Optimized potentials for liquid simulations

PGC Pyrolyzed graphitic carbon
PMMA Poly(methyl methacrylate)

SAM Self-assembled monolayer
SEM Scanning electron microscopy
SPC Simple point-charge water model
STM Scanning tunneling microscopy

Tcl Tool command language (programming language)
TDS Thermal desorption spectroscopy
TEM Transmission electron microscopy
TIPNP Transferable intermolecular potential with N sites
TPT 1,1',4',1"-Terphenyl-4-thiol, terphenylthiol

VMD Visual Molecular Dynamics

XPS X-Ray photoelectron spectroscopy

Publications and related work

Peer-reviewed papers

- **Julian Ehrens**, Florian Gayk, Patrick Vorndamme, Tjark Heitmann, Niklas Biere, Dario Anselmetti, Xianghui Zhang, Armin Gölzhäuser, and Jürgen Schnack. Theoretical formation of carbon nanomembranes under realistic conditions using classical molecular dynamics. Physical Review B, 103(11):115416, 2021, Ref. [1]

- Florian Gayk, **Julian Ehrens**, Tjark Heitmann, Patrick Vorndamme, Andreas Mrugalla, and Jürgen Schnack. Young's moduli of carbon materials investigated by various classical molecular dynamics schemes. Physica E: Low-dimensional Systems and Nanostructures, 99:215 – 219, 2018, Ref. [2]

Talks and posters

- DPG SKM 2019 - Short talk: Molecular dynamics investigation of Young's moduli of carbon nanomembranes (CNMs)

- DPG SKM 2021 - Virtual conference poster: Molecular dynamics simulations of carbon nanomembranes (CNMs)

- Various collaborative talks in experimental groups working on CNMs or related topics at Bielefeld University

Disclaimer

This work is based on theoretical investigations of carbon nanomembranes initiated by Jürgen Schnack and Florian Gayk whose results have been summarized in the form of Florian Gayk's Master's thesis [3]. The study of Young's moduli by Florian Gayk has been augmented by me and was published as a summary on theoretical investigations of CNMs in Ref. [1]. Further research has been conducted as a group effort between Florian Gayk, Patrick Vorndamme, Tjark Heitmann, Andreas Mrugalla, Jürgen Schnack and me which was published in Ref. [2].

Parts of this thesis are closely following or have been quoted verbatim from the above mentioned publications.

Acknowledgements

Let me use this opportunity to express my gratitude to all the people that accompanied me on my way, for what they added to my life.

First and foremost, I would like to thank my father Ewald and already deceased mother Adelheid for their enduring and loving support enabling my studies. Without you, I would not be at this point in life.
To my girlfriend Maria-Bernadette Riedl, whom I first met in my office on floor E5 when she began her Bachelor's thesis, for her daily emotional support and honest interest in my work. Thank you for accepting me for who I am, your trust and unconditional love.

To my former professors and teachers in particular the high school teachers Christine Haese and Dirk Hanke for their inspiration and motivation to study physics as well as their continuing support. It is always a pleasure to meet you at the Tag der offenen Tür at the Thomas-Morus-Gymnasium in Oelde.
To Heiner Kriener, pensioned English teacher and one of the most inspiring people I have ever met, for his time, effort and motivation from during my school years up until today as a good friend. I hope my handwriting improved.

This thesis would not be possible without my advisor Prof. Dr. Jürgen Schnack. His individual approach to teaching and encouraging support helped me through uncertainties and shaped my work attitude.
Also, I would like to thank Prof. Dr. Armin Gölzhäuser for being the second reviewer of my thesis as well as the discussions with him and all of his group members working on carbon nanomembranes experimentally, especially but not limited to Dr. Xianghui Zhang and Florian Paneff.
Furthermore, international collaboration and fruitful discussion with the Australians Prof. Nigel Marks and PhD candidate Filip Vukovic stimulated my thoughts on some aspects of this thesis and sharing of the details of Marks' EDIP is gratefully acknowledged.
I appreciate the time with my former office colleagues Michael Czopnik and Christian Beckmann in our shared offices and at conferences.
I would like to acknowledge the extensive work of the secretaries Anja Deuchars, Susi von Reder and especially the emotional support from Hannelore Litschewsky means a lot to me. I wish you happiness and good health on all the days of your retirement.
I should not forget my fellow students Patrick Vorndamme, Tjark Heitmann and Florian Gayk for collaborations and discussions.

There are many more people to thank, including but not limited to and in no particular order Melissa Savma, Hannah Topmöller, Jenny Fjodorova, Dennis Bollweg, Nicholas Junge, Julian Cremer and Tomasz Checinski for their time and open ears.
To my cat Henri 🐾 who is purring calmly in my lap while writing this.

1. Introduction

Many fascinating and technologically relevant carbon-based materials, see e.g. Refs. [4, 5, 6, 7, 8, 9], cannot be simulated by quantum mechanical means, not even by density functional theory (DFT), since they are either too extended or not regular. The latter is for instance the case for nanometer thin carbon nanomembranes (CNMs) of macroscopic lateral size, which are produced from molecular precursors [4, 10, 11, 12, 5, 7, 8]. Although the precursor molecules such as the aromatic biphenyl-, terphenyl- and naphtalene-thiols (refer to Appendix A.1 for details) are well-characterized, not much is known about the internal structure of such nanomembranes [13]. The reason is that existing characterization methods fail to deliver accurate results mainly due to the nanometer size thickness and the tiny weight, which, for example, does not allow accurate X-ray structure determination. In addition to that, the material is very likely highly disordered, which renders an X-ray structure determination nearly impossible. On the other hand, the material can be produced to macroscopic extensions, and it is mechanically stable. Therefore, mechanical properties, such as Young's moduli, can be determined for such membranes [14]. The moduli of membranes from aromatic self-assembled monolayers (SAMs) turn out to be of the order of 10 GPa [14], i.e. the material is astonishingly soft compared to e.g. graphene (1000 GPa [15]). Recent studies on membranes from aliphatic SAMs determined even smaller moduli of around 0.5 GPa [16].

It is also possible to study water permeation [17, 18] as well as electrical properties [19] in order to further characterize the membranes. Investigation by means of near edge X-ray absorption fine structure (NEXAFS) is possible, too, which allows to estimate the aromaticity, i.e. the amount of intact aromatic carbon rings, still present in the CNM [20]. Other methods like infrared reflection absorption spectroscopy (IR-RAS) and thermal desorption spectroscopy (TDS) can resolve the molecular composition and describe changes between a SAM and the resulting CNM, thus indicating a cross-linking process [20, 21]. Atomic force microscopy (AFM) and scanning tunneling microscopy (STM) deliver topographic images of CNMs deposited on substrate material [18]. This allows to infer information of membrane structure on mesoscopic (nm) lateral scales, i.e. the sizes and distribution of holes and voids across the membrane which is closely related to transport properties of gases and liquids through the membrane.

In this thesis, methods for realistic and large-scale theoretical simulations of CNMs will be presented. Although CNMs have been studied experimentally for a long period of time, the number of computer simulations on this topic has been scarce due to computational restrictions as well as difficulties in comparison with experimental results:

1. To adequately study the properties of CNMs with computer simulations, dimensions of the model system have to be large enough to describe a realistic membrane. For that, thousands to hundred thousands of atoms have to be in-

corporated in the simulation, which for quantum mechanical simulations is not at all feasible. Thus, a classical molecular dynamics approach was chosen for the simulations, which is unavoidably an approximation. This holds in particular for the classical carbon-carbon interaction [2]. Electronic properties are unavailable in classical molecular dynamics as well, further limiting possibilities.

2. The CNM will be in a disordered metastable state, i.e. a local minimum in a huge configuration space with potential correlations between SAM and CNM. The true ground state of the material, which consists of pure carbon, would be a flake of graphite. It is very likely that a large number of disordered metastable states is actually equivalent in so far that they all constitute mechanically stable membranes.

3. Classification of simulated membranes and comparison with experimental results is limited to indirect observables such as the Young's modulus, topographic images, aromaticity and permeation properties [17, 18] due to the lack of experimental structural information. The latter is readily available in molecular dynamics simulations.

For the simulations in this thesis, classical molecular dynamics as implemented in the publicly available large atomic/molecular massively parallel simulator (LAMMPS) [22] is employed. Previous studies showed that the potentials and algorithms implemented in LAMMPS are accurate to a large extent for other carbon-based systems as e.g. diamond, graphene or nanotubes [2]. Additionally, the EDIP potential by Marks [23, 24], not included in the public release of LAMMPS, has been implemented in the local version due to its known-good performance.

A simulated production process of CNMs is set up to mimic gross features of the formation of a CNM as a dynamical process that consists of excitation, compression as well as expansion and equilibration, which goes far beyond the more quasistatic approach of Ref. [13] used earlier. The main focus lies on CNMs created from SAMs consisting of experimentally favoured aromatic precursor molecules such as BPT, TPT and NPTH. Simulation of recently discovered aliphatic membranes will be discussed with the example of 1-Octadecanethiol (ODT) as well.

The experimental observation of loss of aromaticity will be covered by ring statistics for the simulated membranes. Membranes created by the model irradiation procedures are checked for mechanical stability by determination of the Young's modulus. For this, three different approaches to the theoretical determination of the modulus are presented that can be split into static and dynamic approaches. The static method is implemented in LAMMPS and determines the Young's modulus from the curvature of the potential energy. The dynamic methods developed for this thesis exploit the property of linear elasticity with a stress-strain approach on the one hand and a barostat method on the other. Differences and strengths of the methods will be discussed. Additionally, determination of the Young's modulus by means of nanoindentation will be modeled. In an effort to describe the permeation properties of CNMs, large-scale explicit solvent water simulations will be carried out. For that purpose, holes in the membrane are identified with a brute-force algorithm. Hole identification is done using atomic force microscopy in the experiment which is limited in resolution. An artistic approach to simulating AFM images from exact atom positions as available in molecular dynamics will be presented for qualitative comparison.

2. Classical molecular dynamics theoretical background

Molecular dynamics is an umbrella term for computational physics simulations modeling atomic and molecular dynamics in materials science. There exist many variations of simulation schemes which can mainly be divided into classical and quantum ab-initio methods. Both methods numerically compute the classical, i.e. Newtonian time evolution of point-like atoms or molecules composed of such atoms. The main difference between the two is hidden in the calculation of interatomic forces. For ab-initio molecular dynamics, the force on each atom is evaluated each timestep, e.g. using density functional theory (DFT), solving the Schrödinger equation and minimizing the energy for the given configuration [25]. This computationally very expensive calculation becomes unviable quickly when exceeding hundreds to low-thousands of atoms while delivering very high accuracy down to the quantum level [26].

The size limitation is mended by classical molecular dynamics by introducing predefined effective interatomic potentials, sometimes called force field that are used to evaluate the force on each atom by evaluating the gradient of said potential. Accuracy of the classical method boils down to the performance of the effective potential which has to be carefully tweaked for every type of atom and composites thus often limiting the applicability of a potential to very few materials by verification with observables from experiments or, where possible, ab-initio calculations [27].

There is a vast amount of interatomic potentials available, all performing somewhat different with respect to how and for what they have been tailored. Some potentials such as AMBER [28] or OPLS [29] might be concerned more with biomolecular processes, e.g. how a protein docks in a pore of a cell, while others try to best describe the interactions of e.g. carbon atoms such as Tersoff [30], Brenner [31], AIREBO [32], or EDIP [23]. The latter group is of most interest for this thesis, and details will be presented in the following chapter.

For the simulations presented later on, classical molecular dynamics as implemented in the publicly available large atomic/molecular massively parallel simulator (LAMMPS) [22], is employed. An overview of the theoretical physics behind molecular dynamics as well as simulation algorithms, constraints and best practices is given in Ch. 2.2ff.

2.1. Effective interatomic potentials

A realistic classical carbon-carbon interaction must be able to account for the various sp^n-binding modes of carbon as depicted in Fig. 2.1 which ab-initio methods would compute on the fly. sp^1 hybridization is e.g. prevalent in long chains of carbon atoms, while sp^2 orbitals are found in 2D structures such as graphene. Diamond structure is an example of sp^3 hybridization [2].

(a) sp^1 hybrid orbital, taken from Ref. [33].

(b) sp^2 hybrid orbital, taken from Ref. [34].
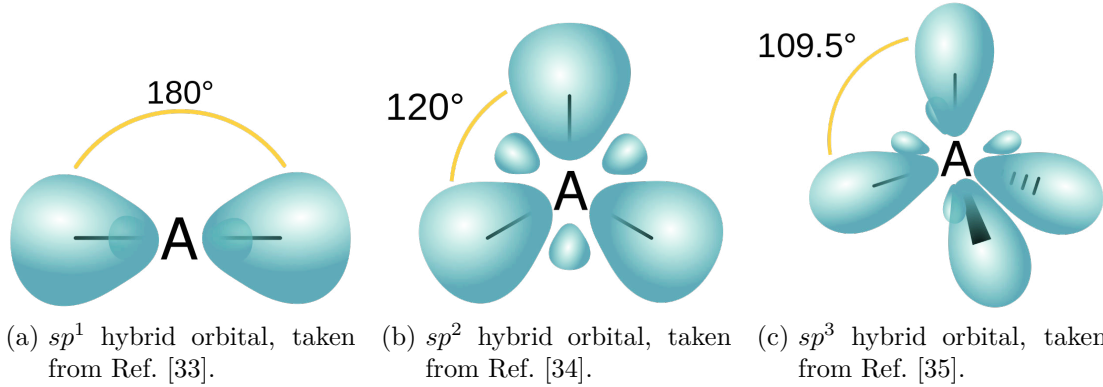
(c) sp^3 hybrid orbital, taken from Ref. [35].

Figure 2.1.: Schematic representation of hybridization orbitals.

The molecular dynamics package LAMMPS offers several of such potentials, among them those developed by Tersoff and Brenner in various versions [30, 31, 36] as well as new extensions built on the original potentials. More recently, machine learning has been involved in systematically finding the best parameters for potentials such as the Gaussian Approximation Potentials (GAP) framework based on quantum mechanical data [37].

In addition to the implemented potentials, the improved (carbon only) EDIP potential by Marks [23, 24] is used for some of the simulations presented in this thesis. The potential is so far not included in standard versions of LAMMPS and has been shared in private communication by Marks which is thankfully acknowledged. Taking this potential as an example, one can qualitatively explain how such potentials work. These potentials are comprised of density-dependent two- and three-body potentials, U_2 and U_3 in this example respectively,

$$U\left(\vec{R}_1, \ldots, \vec{R}_N\right) = \sum_{i=1}^{N} \left\{ \sum_{\substack{j=1 \\ j \neq i}}^{N} U_2(R_{ij}, Z(i)) \right. \tag{2.1}$$
$$\left. + \sum_{\substack{j=1 \\ j \neq i}}^{N} \sum_{\substack{k=j+1 \\ k \neq i}}^{N} U_3(R_{ij}, R_{ik}, \theta(i,j,k), Z(i)) \right\}$$

which account for the various binding modes. This is achieved by an advanced parametrization in terms of a smooth coordination variable $Z(i)$ as well as by appropriate angle dependencies $\theta(i, j, k)$. The EDIP potential employs a cutoff of 3.2 Å and a dihedral penalty.

These major components highly effect the performance of the effective potential by directly influencing the resulting equilibrium distance of carbon atoms [13] as depicted in Fig. 2.2 which should ideally be close to the experimental value of 1.42 Å [38].
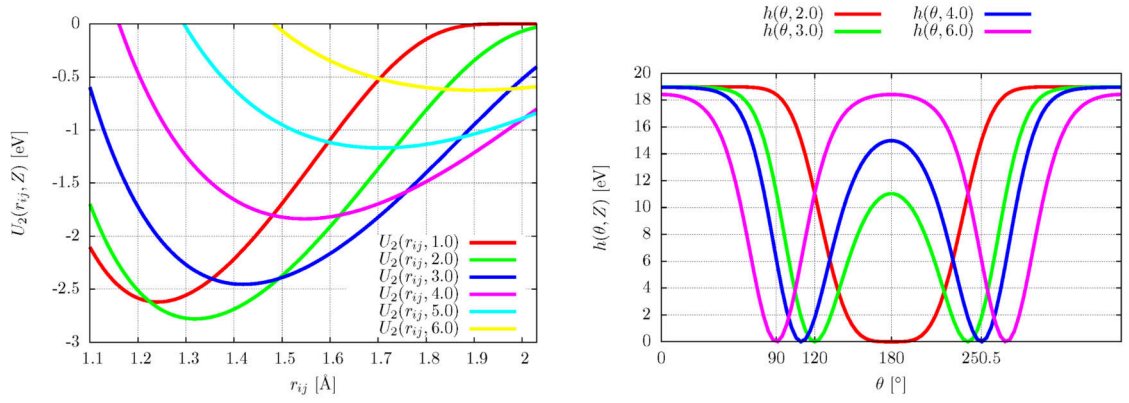
Figure 2.2.: Influence of the parametrization on the two- and three-body potentials, taken from Ref. [13].

Another popular option for carbon-carbon (C-C) interactions is AIREBO [32], which also includes the necessary implementation for carbon-hydrogen (C-H) interactions.

Since the performance of a potential cannot be directly transferred to all kinds of simulation setups by checking its performance on one material and extrapolating its applicability to all other materials made from the same atom type, one has to be careful in choosing the right potential for the material under test. This might even be true for different observables to be calculated with the same potential versus another. Therefore, preliminary studies have been made in order to benchmark possible carbon-carbon potentials for previous work on the topic of CNMs [2].

Most of the tested potentials performed well when confronted with known materials such as carbon nanotubes, graphene or diamond. EDIP performed especially well and has additionally been previously tested by its authors for the potential in describing disordered carbon systems created from randomized quenching processes [39].

2.2. Simulation constraints and specifics

Molecular dynamics simulations are fundamentally limited by the scalability, often given in "Big O Notation" $O(n)$ of the algorithms for e.g. force field evaluation, time integration or granularity of solvent models with n being the number of particles in the simulation. Most classical molecular dynamics codes, e.g. the algorithms implemented in LAMMPS [22] as used for this thesis are designed to be highly parallel, i.e. the workload can be split between multiple CPU cores and even multiple networked machines. The most computationally expensive calculation is the evaluation of the potential, which scales with $O(n^2)$ when long-range interactions are included [40]. Clever binning of neighboring interactions, called neighbor list [22] can improve the performance to some extent, allowing for millions of particles to be simulated.

For ab-initio methods, e.g. DFT, the scaling is much worse and thus limits this group of simulations to several hundred or at most thousands of particles. Molecular dynamics simulations, depending on the complexity and size, can take seconds on a single (multicore) CPU machine and up to several hundred thousand CPUh on supercomputers such as LRZ's SuperMUC as can be witnessed from yearly LRZ high performance computing reviews, e.g. Ref. [41].

Simulation duration is inherently bound to the timescale on which the physics occur, e.g. femtoseconds for interactions of carbon atoms in a carbon nanomembrane. This inherent timescale is a physical property of the underlying dynamics which leads to the necessity of careful selection of timestep length for molecular dynamics simulations to avoid unphysical behavior or unnecessarily long simulation times.

An upper limit of timestep length can be found using the Nyquist-Shannon theorem, which states [42]:

"If a function $x(t)$ contains no frequencies higher than B hertz, it is completely determined by giving its ordinates at a series of points spaced $1/(2B)$ seconds apart.", where B is related to the quickest dynamics of the system.

Overall, this means that several millions of timesteps would have to be performed to describe nanosecond phenomena, which is computationally expensive or simply not feasible. Therefore, many simulated processes are artificially accelerated e.g. by exaggerated force, velocity or momentum when modeling a physical process to be able to complete the simulation in reasonable time. This holds for many of the simulations performed for this thesis, ranging from electron momentum transfer in the process of carbon nanomembrane formation to pressure in explicit solvent permeation studies. The latter of which might take several minutes or hours in the experiment [17], which is prohibitively long for molecular dynamics simulations.

The basic constraints of a molecular dynamics simulation lie in the choice of boundary conditions and the (thermodynamic) ensemble, determining whether bulk or fixed size properties are computed for given conditions, e.g. temperature and pressure. Appropriate LAMMPS commands will be given alongside the discussions in the following chapters.

2.3. Boundary conditions

An overview of typical boundary conditions for molecular dynamics simulations can be found in the LAMMPS documentation [43]. Boundary conditions can have a huge impact on the quality of the simulation, especially when concerned with finite-size effects.

2.3.1. Non-periodic boundary conditions

This is especially true for fixed boundary conditions (*boundary f* in LAMMPS), where a particle inside the simulation box is not allowed to move from one side of the box to the other side or to interact with atoms across the boundary [43]. The side lengths of the initially created box stay the same during the simulation with atoms potentially escaping the box during a timestep either counted as lost and deleted or the simulation run failing. Fixed boundary conditions are suitable for bigger systems without periodicity.

Other non-periodic boundary conditions are shrinkwrapped and limited shrinkwrapped conditions. Shrinkwrapped boundary conditions (*boundary s* in LAMMPS) size the simulation box such that at every timestep all atoms are contained, which e.g. is used in electron irradiation simulations as presented in Ch. 6 to allow atoms to move and even escape the membrane. Limited shrinkwrapping (*boundary m* in LAMMPS) defines the initial box size as a minimum for shrinkwrapping, i.e. the box will never get smaller than the set minimum even though the system is smaller than the simulation box, which is e.g. used for evaporation studies [43].

2.3.2. Periodic boundary conditions

Periodic boundary conditions (*boundary p* in LAMMPS) allow interactions across boundaries as well as particles to cross the boundary or replication of the simulation box at all sides. However, this does not imply that the simulation box size stays the same as e.g. simulation in an isothermal-isobaric (NPT) ensemble allows the box to deform under pressure (*fix npt* or *fix deform* in LAMMPS). Periodic boundary conditions can be used to calculate bulk properties thus limiting finite-size effects but potentially imprinting unwanted periodicity onto the system. This is especially true for ab-initio molecular dynamics, where periodicity is often used for large systems to even be able to run the computationally expensive simulation. An example of this is the modeling of CNM formation using first-principles DFT calculations in Ref. [44].

Boundary conditions may be chosen differently for all three cartesian axes of the simulation box.

2.4. Molecular dynamics ensembles

Molecular dynamics ensembles are closely related to thermodynamic ensembles, such as microcanonical, canonical and grandcanonical or isothermal-isenthalpic ensembles. The difference lies in technical details of the integration of the equations of motion and how temperature as well as pressure are defined, calculated and influenced.

2.4.1. Microcanonical (NVE) ensemble

The microcanoncial ensemble is defined by adiabatic conditions, i.e. no energy or mass exchange and constant volume as characterized by the conserved number of particles N, conserved volume V and conserved energy E. Thus, total energy conservation between potential and kinetic energy can be used to calculate the trajectories of particles in the simulation by solving Newton's equation of motion with appropriate integrators as presented in Ch. 2.5. The LAMMPS command *fix nve* [45] sets up the simulation in said ensemble and uses velocity Verlet integrators to obtain trajectories.

2.4.2. Canonical (NVT) ensemble

The canonical ensemble differs from the microcanonical ensemble in that energy exchange is allowed and temperature T is conserved instead of energy E. In molecular dynamics simulations this can be achieved by using thermostats that enable heat exchange of the system through various means such as coupling to virtual heat baths or simple temperature scaling through velocity scaling. These thermostats may not only be used to keep the system at constant temperature trying to obtain a physical canonical ensemble, but also for the study of temperature-dependent processes. Thermostat algorithms employ hugely different approaches as presented in detail in Ch. 2.8, easily resulting in non-physical behavior. LAMMPS offers a variety of thermostats, e.g. Nosé-Hoover with time-integration using the *fix nvt* command [46] or Berendsen without time-integration, *fix temp/berendsen* [47], which would mandate time integration using e.g. *fix nve*. This also indicates that the meaning of molecular dynamics ensembles is slightly different from thermodynamic ensembles. Another choice is the stochastic Langevin thermostat using the *fix langevin* command [48].

2.4.3. Isothermal-isobaric (NPT) ensemble

For an isothermal-isobaric (NPT) ensemble, number of particles N, pressure P and temperature T are conserved, thus allowing volume and energy to change. Conservation of pressure and temperature are achieved by combining thermostats and barostats. Barostats are closely related to thermostats and may not only be used to obtain a physical isothermal-isobaric ensemble, but to study pressure-dependent processes such as the determination of elasticity presented in Ch. 6.8. Similar to thermostats, there are barostats that include time integration such as *fix npt* [49] and those that do not include time integration, e.g. *fix press/berendsen* [50]. There is also the *fix nph* command [51] which would only affect pressure without a thermostat in place, potentially leading to an isothermal-isenthalpic (NPH) ensemble.

2.5. Equations of motion and time integration

The most time-consuming part of molecular dynamics simulations is the calculation of the forces between particles [40] as defined by the gradient of the effective potential $U(\vec{r}_1, ..., \vec{r}_N)$ also known as the Newton's equation of motion [52]:

$$m_i \cdot \ddot{\vec{r}}_i = \vec{F}_i = -\nabla_{r_i} U(\vec{r}_1, ..., \vec{r}_N) \, , \qquad (2.2)$$

where m_i is the mass of particle i, $\vec{r}_i$ its position and $\vec{F}_i$ the force on the particle.

To determine the time evolution of the particles, the equations of motion have to be solved by an appropriate numeric procedure. Common, fast and simple algorithms for this are "velocity Verlet" and "leap-frog" integrators [53] with few differences between the two as explained in detail further on. The following derivation of the velocity Verlet algorithm by Taylor expansion of the atom positions is adapted from Refs. [54, 40]:

$$r(t + \Delta t) = r(t) + v(t)\Delta t + \frac{F(t)}{2m}\Delta t^2 + \frac{\Delta t^3}{3!}\dddot{r} + \mathcal{O}\left(\Delta t^4\right) \qquad (2.3)$$

$$\text{and } r(t - \Delta t) = r(t) - v(t)\Delta t + \frac{F(t)}{2m}\Delta t^2 - \frac{\Delta t^3}{3!}\dddot{r} + \mathcal{O}\left(\Delta t^4\right) \, , \qquad (2.4)$$

where $F(t)$ is the shorthand form of $F(r_1(t), ..., r_N(t))$. Adding Eqn. 2.4 to Eqn. 2.3 without shifting equation 2.4 by $t \to t + \Delta t$ would give the Verlet integrator result for the position, i.e.

$$r(t + \Delta t) + r(t - \Delta t) = 2r(t) + \frac{F(t)}{m}\Delta t^2 + \mathcal{O}\left(\Delta t^4\right) \qquad (2.5)$$

$$\to r(t + \Delta t) \approx 2r(t) - r(t - \Delta t) + \frac{F(t)}{m}\Delta t^2 \, , \qquad (2.6)$$

which would be inconvenient for computer simulations due to the dependence on the current and previous timestep as opposed to only the current timestep which is the case for velocity Verlet using the mentioned shift:

$$r(t + \Delta t) = r(t) + v(t)\Delta t + \frac{F(t)}{2m}\Delta t^2 \, . \qquad (2.7)$$

Velocities in the Verlet scheme would have the same issue:

$$r(t + \Delta t) - r(t - \Delta t) = 2v(t)\Delta t + \mathcal{O}\left(\Delta t^3\right) \qquad (2.8)$$

$$\to v(t) = \frac{r(t + \Delta t) - r(t - \Delta t)}{2\Delta t} + \mathcal{O}\left(\Delta t^2\right) \, , \qquad (2.9)$$

which is also avoided by the velocity Verlet variant, leading to:

$$v(t + \Delta t) = v(t) + \frac{F(t + \Delta t) + F(t)}{2m} \cdot \Delta t \, . \qquad (2.10)$$

Velocity Verlet is thus ideal with regard to both spatial, i.e. memory usage, and time complexity, the implications of which can be outlined with the following update scheme that is applied at each timestep of length δt [40]:

- Update particle locations for the next timestep t_{n+1}: $r(t_{n+1}) = v(t_n) \cdot \delta t + \frac{F(t_n)}{2m} \cdot \delta t^2$

- Evaluate forces for the next timestep t_{n+1}: $F(t_{n+1}) = -\nabla U \left(r_1(t_{n+1}), ..., r_N(t_{n+1}) \right)$

- Update velocities for the next timestep t_{n+1}: $v(t_{n+1}) = v(t_n) + \frac{F(t_n)}{2m} \cdot \delta t + \frac{F(t_{n+1})}{2m} \cdot \delta t$

The main difference to the also popular leap-frog algorithm lies in when coordinates and velocities are evaluated, i.e. velocity Verlet computes $x(t)$ and $v(t)$ at timesteps $t = 0, 1, 2, ...$. Leap-frog on the other hand computes $x(t)$ at $t = 0, 1, 2, ...$ but $v(t)$ at $t = 0 + \frac{1}{2}, 1 + \frac{1}{2}, 2 + \frac{1}{2}, ...$ thus shifted by half of a timestep (which is why the term "leap-frog" is used) [55]. Velocity Verlet is thus beneficial in that both positions and velocities are calculated at the same timestep which allows for simultaneous calculation of potential and kinetic energy.

2.6. Temperature

One way to derive the definition of temperature is by using the equipartition theorem which relates temperature to average energies of the system. The most general formulation of the equipartition theorem can be found in many textbooks, e.g. by K. Huang [56] and R. K. Pathria [57].

Derivations using the equipartition theorem make use of the Hamiltonian function of the system and the property of the expectation value

$$\left\langle x_i \frac{\partial H}{\partial x_j} \right\rangle = k_B T \delta_{ij} \tag{2.11}$$

for generalized coordinates $x_k \in \{q_k, p_k\}$, where q_k and p_k are coordinates and momenta respectively, k_B being the Boltzmann constant. In particular, the following relation with d the dimension of the system and N the number of particles,

$$\left\langle \sum_{i=1}^{d \cdot N} p_i \frac{\partial H}{\partial p_i} \right\rangle = \left\langle \sum_{i=1}^{d \cdot N} p_i \dot{q}_i \right\rangle = dN k_B T , \tag{2.12}$$

holds when looking at the momenta, i.e. $x_i = p_i$ and using the Hamiltonian relation $\frac{\partial H}{\partial x_i} = \frac{\partial H}{\partial p_i} = \dot{q}_i$. For many systems, especially molecular dynamics solving the Newtonian equations, constraints are scleronomic and holonomic, i.e. independent of time and the particles' velocity, respectively [58]. Thus, the kinetic energy E_{kin} of the system can be expressed as a homogeneous quadratic function of its generalized momenta:

$$E_{kin} = \sum_{i,j} a_{ij} p_i p_j . \tag{2.13}$$

Therefore also immediately follows that

$$\left\langle \sum_{i=1}^{d \cdot N} p_i \frac{\partial H}{\partial p_i} \right\rangle = \left\langle \sum_{i=1}^{d \cdot N} \sum_{j,k} p_i \frac{\partial a_{jk} p_j p_k}{\partial p_i} \right\rangle \tag{2.14}$$

$$= \left\langle \sum_{i=1}^{d \cdot N} \sum_{j,k} p_i a_{jk} \left(\delta_{ij} p_k + \delta_{ik} p_j \right) \right\rangle = 2 \left\langle E_{kin} \right\rangle , \tag{2.15}$$

and by rearranging Eqn. 2.12, the temperature is proportional to the average kinetic energy of the system:

$$T = \frac{2 \left\langle E_{kin} \right\rangle}{dN k_B} , \tag{2.16}$$

where $d \cdot N$ is the total number of degrees of freedom, i.e. every independent quadratic term of the Hamiltonian.

2.7. Pressure

The derivation of pressure follows the same principle as the derivation of temperature, the difference lying in the calculation being focused on the coordinates q_i and the corresponding Hamiltonian equation $\frac{\partial H}{\partial q_i} = -\dot{p}_i$ leading to:

$$\left\langle \sum_{i=1}^{d \cdot N} q_i \frac{\partial H}{\partial q_i} \right\rangle = - \left\langle \sum_{i=1}^{d \cdot N} q_i \dot{p}_i \right\rangle , \tag{2.17}$$

where the term $\left\langle \sum_{i=1}^{d \cdot N} q_i \dot{p}_i \right\rangle$ can be identified with the virial $W = -dNk_\mathrm{B}T$. A detailed definition of how it is implemented by LAMMPS for a particular potential is described in Refs. [3, 59]. An integral component of a molecular dynamics simulation is the simulation box with surface normal $\mathrm{d}\vec{S}$ which can impose forces on the atoms depending on the chosen boundary conditions. Therefore one has to differentiate the forces imposed by the simulation box and forces between atoms caused by interaction between them. To express the work done by the simulation box alone, one can express that part of the virial in the following way with N_0 the number of atoms located at the edge of the simulation box [3]:

$$W_0 = \left\langle \sum_{l=1}^{N_0} \vec{r}_l \vec{F}_l \right\rangle = -P \oint \vec{r} \cdot \mathrm{d}\vec{S} = -P \int_V \nabla \vec{r} \mathrm{d}V = -d \cdot PV \,. \tag{2.18}$$

With W_in being the internal part of the virial and since $W = W_0 + W_\mathrm{in}$ holds for the total work, the pressure can be expressed by simple rearrangement and substitution similar to the derivation of the temperature:

$$-dNk_\mathrm{B}T = W = W_0 + W_\mathrm{in} = -d \cdot PV + W_\mathrm{in} \tag{2.19}$$

$$P = \frac{Nk_\mathrm{B}T}{V} + \frac{W_\mathrm{in}}{Vd} \tag{2.20}$$

$$P = \frac{Nk_\mathrm{B}T}{V} + \frac{\left\langle \sum_{i=1}^{N} \vec{r}_i \cdot \vec{F}_i \right\rangle}{Vd} \,. \tag{2.21}$$

2.8. Thermo- and barostats

Thermo- and barostats are essential when one wants to simulate the behavior in an NVT- or NPT-ensemble respectively or to control temperature and pressure in an NVE simulation. Both are quite similar to each other when it comes to their algorithmic implementation in molecular dynamics simulations. The following discussion is therefore limited to thermostats and barostats as implemented by LAMMPS, whereas thermostats will be discussed in detail with differences to the corresponding barostats pointed out. Thermostat usage can be motivated by various reasons, e.g. but not limited to, to match an experimental setup or study temperature dependent processes [60]. Their most naive application is to scale variables, i.e. barostats scale lengths and thermostats scale velocities in order to reach a desired value or keep it steady at a given timestep. The latter usecase is also important to combat potential energy drift, e.g. caused by numerical errors [60].

No matter how individual thermostats are implemented, all thermostat algorithms require a modification of Newton's second law [60]:

$$\ddot{\mathbf{r}}_i(t) = m_i^{-1}\mathbf{F}_i(t) \ \rightarrow \ \ddot{\mathbf{r}}_i(t) = m_i^{-1}\mathbf{F}_i(t) - \gamma_i(t)\dot{\mathbf{r}}_i(t) + m_i^{-1}\mathbf{R}_i(t)\,, \tag{2.22}$$

where $\mathbf{R}_i(t)$ is a stochastic force, e.g. used in a Langevin thermostat, and $\gamma_i(t)$ a friction coefficient, e.g. used in Nosé-Hoover dynamics, while not all terms might be used at the same time by all thermostat algorithms [60]. For a very basic thermostat this would mean that given the temperature $T(t)$ at a specific time t the resulting change in temperature towards the desired temperature T_0 by velocity scaling with parameter λ is given by:

$$\Delta T = 2\sum_{i=1} \frac{\frac{1}{2}m_i\left(\lambda\dot{\mathbf{r}}_i\right)^2}{Nk_{\mathrm{B}}} - 2\sum_{i=1} \frac{\frac{1}{2}m_i\dot{\mathbf{r}}_i^2}{Nk_{\mathrm{B}}} \tag{2.23}$$

$$= \left(\lambda^2 - 1\right)T\left(t\right) \ \text{with} \ \lambda = \sqrt{T_0/T\left(t\right)}\,. \tag{2.24}$$

One might consider this method to be of strong-coupling type as opposed to the other methods outlined in the following, because the temperature is just multiplied at each timestep not allowing for any type of naturally occurring fluctuations as e.g. a Nosé-Hoover or Langevin type would include. Thermostats of this category are able to correct this shortcoming by virtual coupling to a heat bath or a virtual mass for the coupling interaction. Berendsen introduced the formulation of a thermostat based on a first-order relaxation equation [61], while Nosé and with later improvements by Hoover introduced the extended system method [62, 63]. There are also stochastic methods such as the Langevin thermostat based on Langevin dynamics whose type is often considered to be the most physically correct choice of thermostats due to its random and fluctuating nature [60].

2.8.1. Berendsen thermostat

The Berendsen thermostat is a first-order equation means of temperature relaxation by weak coupling aiming to couple a system with an average temperature $\overline{T}$ to an external heat bath with temperature T_0 [60]. The rate of change of the instantaneous temperature then obeys the proportionality

$$\frac{\mathrm{d}T\left(t\right)}{\mathrm{d}t} = \frac{1}{\tau_{\mathrm{B}}}\left(T_0 - T\left(t\right)\right)\,, \tag{2.25}$$

where τ_B is a coupling parameter between system and bath that should follow the principle of least local perturbation [60]. For a discrete timestep δt this would result in a temperature change of

$$\Delta T = \frac{\delta t}{\tau_B} \left(T_0 - T(t) \right) . \tag{2.26}$$

This would allow velocities to be scaled like $\vec{v}_i \rightarrow \lambda \cdot \vec{v}_i$ where $\lambda(t, \delta t)$ is a time- and timestep-dependent velocity scaling factor defined by [60]

$$\lambda = \left[1 + \frac{\delta t}{\tau_B} \left(\frac{T_0}{T} - 1 \right) \right]^{1/2} . \tag{2.27}$$

Thus if the relaxation time of the Berendsen thermostat τ_B is close to the timestep δt, the coupling is strong and converges towards the naive scaling method.

2.8.2. Berendsen barostat

The Berendsen barostat is very similar to its thermostat counterpart. It is again a first-order equation means, but this time a differential equation with regard to pressure [64]:

$$\frac{dP(t)}{dt} = \frac{1}{\tau_{B_P}} \left(P_0 - P(t) \right) , \tag{2.28}$$

or as expressed for a timestep δt:

$$\Delta P = \frac{\delta t}{\tau_{B_P}} \left(P_0 - P(t) \right) , \tag{2.29}$$

where P_0 is the target pressure and τ_{B_P} the coupling parameter. Lengths will be scaled according to $\vec{r}_i/L \rightarrow (\mu\vec{r}_i)/(\mu L)$ with a scaling factor defined as [64]

$$\mu = \left[1 + \frac{\delta t}{\tau_{B_P}} \left(P - P_0 \right) \right]^{1/3} . \tag{2.30}$$

2.8.3. Nosé-Hoover thermostat

Implementation of the extended-system method proposed by Nosé [62] and later improved by Hoover [65] is not as straightforward as the Berendsen method. The general idea is to extend the real system with an artificial dynamic variable $\tilde{s}$ and velocity $\dot{\tilde{s}}$ which is associated with a "mass" $Q > 0$ [60]. This would lead to a stretching of the timescale in the extended system, i.e. $dt = \tilde{s}^{-1}(\tilde{t})d\tilde{t}$, which is problematic for trajectory sampling in molecular dynamics simulations due to uneven time intervals. The derivation presented in the following describes the original formulation with the necessary changes for transformation into real-system variables avoiding uneven time intervals [60]. For atomic coordinates $\mathbf{r}$ and velocities $\dot{\mathbf{r}}$ as well as the new variable $\tilde{s}$, the time-scaling definition would lead to

$$\tilde{\mathbf{r}} = \mathbf{r}, \; \dot{\tilde{\mathbf{r}}} = \tilde{s}^{-1}\dot{\mathbf{r}}, \; \tilde{s} = s, \text{ and } \dot{\tilde{s}} = \tilde{s}^{-1}\dot{s} , \tag{2.31}$$

with the Lagrangian for the extended system:

$$\mathcal{L}_e(\tilde{\mathbf{r}}, \dot{\tilde{\mathbf{r}}}, \tilde{s}, \dot{\tilde{s}}) = \frac{1}{2} \sum_{i=1}^{N} m_i \tilde{s}^2 \dot{\tilde{r}}_i^2 - \mathcal{U}(\tilde{\mathbf{r}}) + \frac{1}{2} Q \dot{\tilde{s}}^2 - g k_B T_0 \ln \tilde{s} , \tag{2.32}$$

where $g = N_{df}$ is the number of degrees of freedom of the real system [60]. The last two terms describe the kinetic energy of the extended system with mass Q and potential energy term in $\tilde{s}$ such that the described ensemble stays canonical [60]. The Lagrangian equations of motion for the extended system are

$$\ddot{\tilde{\mathbf{r}}}_i = m_i^{-1}\tilde{s}^{-2}\tilde{\mathbf{F}}_i - 2\tilde{s}^{-1}\dot{\tilde{s}}\dot{\tilde{\mathbf{r}}}_i \tag{2.33}$$

$$\text{and} \ \ \ddot{\tilde{s}} = Q^{-1}\tilde{s}^{-1}\left(\sum_{i=1}^{N}m_i\tilde{s}^2\dot{\tilde{r}}_i^2 - gk_BT_0\right), \tag{2.34}$$

with the latter being a second order differential equation, which may lead to oscillatory behavior in the form of heat flowing in and out of the system, thus potentially leading to temperature fluctuations [60]. Consequently, this would mandate careful choice of the virtual mass Q to achieve realistic temperature fluctuations. Instead, an effective relaxation time

$$\tau_{NH} = (N_{df}k_BT_0)^{-1/2}\,Q^{1/2} \tag{2.35}$$

is introduced to characterize the coupling strength to the virtual heat bath in the case where real-system velocities are initialized with a Maxwell-Boltzmann distribution [60]. To avoid the problem of a stretched timescale, the equations of motion can be reformulated with sampling compatible with molecular dynamics by means of the following transformations [60]:

$$\begin{aligned}
&s = \tilde{s}, \ \dot{s} = \tilde{s}\dot{\tilde{s}}, \ \ddot{s} = \tilde{s}^2\ddot{\tilde{s}} + \tilde{s}\dot{\tilde{s}}^2 \\
&\mathbf{r} = \tilde{\mathbf{r}}, \ \dot{\mathbf{r}} = \tilde{s}\dot{\tilde{\mathbf{r}}}, \ \ddot{\mathbf{r}} = \tilde{s}^2\ddot{\tilde{\mathbf{r}}} + \tilde{s}\dot{\tilde{s}}\dot{\tilde{\mathbf{r}}} \\
&p_s = \tilde{s}^{-1}\tilde{p}_s, \ \dot{p}_s = \dot{\tilde{p}}_s - Q^{-1}\tilde{s}^{-1}\tilde{p}_s^2 \\
&\mathbf{p} = \tilde{s}^{-1}\tilde{\mathbf{p}}, \ \dot{\mathbf{p}} = \dot{\tilde{\mathbf{p}}} - Q^{-1}\tilde{s}^{-1}\tilde{p}_s\tilde{\mathbf{p}} \\
&\mathbf{F} = \tilde{\mathbf{F}}\,.
\end{aligned} \tag{2.36}$$

Defining $\gamma = s^{-1}\dot{s} = Q^{-1}sp_s$, the equations of motion can be brought into the form

$$\ddot{\mathbf{r}}_i = m_i^{-1}\mathbf{F}_i - \gamma\dot{\mathbf{r}}_i\,, \tag{2.37}$$

with $\dot{\gamma} = -k_BN_{df}Q^{-1}T\left(\frac{g}{N_{df}}\frac{T_0}{T} - 1\right)$ which is similar to the prototype equation used for almost all thermostats [60].

2.8.4. Andersen barostat

The Andersen barostat is an extended-system method similar to but pre-dating the extended-system thermostat by Nosé and Hoover and makes use of a fictitious pressure "bath" which has a physical interpretation of a piston pressurizing the system [66]. To achieve a trajectory average equal to an NPH ensemble average, atom positions $\mathbf{r}_i$ have to be replaced by scaled coordinates $\rho_i = \mathbf{r}_i/V^{1/3}$, where V is the box volume the atoms are placed inside [66]. The Lagrangian of the extended system is

$$\mathcal{L}_e(\tilde{\rho}, \dot{\rho}, Q, \dot{Q}) = \frac{1}{2}Q^{2/3}\sum_{i=1}^{N}m_i\dot{\rho}^2 - \sum_{i<j=1}^{N}\mathcal{U}\left(Q^{1/3}\rho_{ij}\right) + \frac{1}{2}M\dot{Q}^2 - \alpha Q\,, \tag{2.38}$$

where the new variable Q can be interpreted as volume V and M as a mass determining the relaxation times [66]. The first two terms are the kinetic and potential energy of

the system in its new variables. The third term is a kinetic and the fourth a potential energy term in Q. Furthermore, α and M are constants that can be given a physical meaning, when the system is considered to be in a container of variable volume that can be compressed by a piston [66]. Q would be the position of the piston, αV is a potential term of the form pV, with external pressure α and M is the mass of the piston [66]. The equations of motion can be derived analogously to the previously described Nosé-Hoover thermostat. After transformation from the scaled to the original coordinates, the equations of motion are [66]:

$$\frac{\mathrm{d}\mathbf{r}_i}{\mathrm{d}t} = \frac{\mathbf{p}_i}{m_i} + \frac{1}{3}\mathbf{r}_i \frac{\mathrm{d}\ln V}{\mathrm{d}t} \tag{2.39}$$

$$\frac{\mathrm{d}\mathbf{p}_i}{\mathrm{d}t} = -\sum_{j(\neq i)=1}^{N} \hat{r}_{ij}\,\mathcal{U}'(r_{ij}) - \frac{1}{3}\mathbf{p}_i \frac{\mathrm{d}\ln V}{\mathrm{d}t} \tag{2.40}$$

$$\frac{M\mathrm{d}^2 V}{\mathrm{d}t} = -\alpha + \left(\frac{2}{3}\sum_{i=1}^{N}\frac{\mathbf{p}_i^2}{2m} - \frac{1}{3}\sum_{i<j=1}^{N} r_{ij}\,\mathcal{U}'(r_{ij}) \right) / V\,. \tag{2.41}$$

2.8.5. Parrinello-Rahman barostat

The method by Andersen was extended by Parrinello and Rahman to allow for a change of shape of the simulation box under pressure, whereas previously only volume could change that inhibited crystal structure transformations dependant on change in shape [67]. Assuming the simulation box volume is spanned by three vectors $\mathbf{a}, \mathbf{b}$ and $\mathbf{c}$, the corresponding volume can be determined by the scalar triple product $V = \det \mathbf{h} = \mathbf{a} \cdot (\mathbf{b} \times \mathbf{c})$ with which the position $\mathbf{r}_i$ of a particle can be expressed [67]:

$$\mathbf{r}_i = \mathbf{h}\mathbf{s}_i = \zeta_i \mathbf{a} + \eta_i \mathbf{b} + \xi_i \mathbf{c}\,, \tag{2.42}$$

where $\mathbf{s}_i$ is a column vector and $0 < \zeta_i, \eta_i, \xi_i < 1$. This allows to define the distance

$$r_{ij}^2 = (\mathbf{s}_i - \mathbf{s}_j)^{\mathsf{T}}\mathbf{G}(\mathbf{s}_i - \mathbf{s}_j)\,, \tag{2.43}$$

where $\mathbf{G} = \mathbf{h}^{\mathsf{T}}\mathbf{h}$ is the metric tensor. Finally, the modified extended-system Lagrangian is

$$\mathcal{L}_e = \frac{1}{2}\sum_{i=1}^{N} m_i \dot{\mathbf{s}}_i^{\mathsf{T}}\mathbf{G}\dot{\mathbf{s}}_i - \sum_{i=1}^{N}\sum_{j>i}^{N} U(r_{ij}) + \frac{1}{2}W\mathrm{Tr}\,\dot{\mathbf{h}}^{\mathsf{T}}\dot{\mathbf{h}} - pV\,, \tag{2.44}$$

of which the equations of motion can be derived similar to the method described by Anderson. Parrinello and Rahman also derived the equations for the case of general, i.e. non-isotropic, stress [67].

2.8.6. Nosé-Hoover barostat

The method by Andersen extended by Parrinello and Rahman was further improved by Nosé and Hoover to treat molecular systems and include long-range charge-charge interactions [68]. It is the method used in LAMMPS when a *fix npt* or *fix nph* thermo- and/or barostat are in place. The method uses the same coordinates as described by Anderson, but modifies the Lagrangian as explained for short-ranged site-site interactions [68]:

$$\mathcal{L}_e = \frac{1}{2}\sum_{i=1}^{N} m_i \dot{\mathbf{s}}_i^{\mathsf{T}}\mathbf{G}\dot{\mathbf{s}}_i + \frac{1}{2}\sum_i \omega_i^{\mathsf{T}}\mathbf{I}_i\omega_i - \sum_{i=1}^{N}\sum_{j>i}^{N}\mathcal{U}(r_{ij}, \alpha_i, \alpha_j) + \frac{1}{2}W\mathrm{Tr}\dot{\mathbf{h}}^{\mathsf{T}}\dot{\mathbf{h}} - pV\,, \tag{2.45}$$

where the second term has been added by Nosé and Hoover. It describes the kinetic energy of molecular rotations with angular velocity ω_i and inertia tensor $\mathbf{I}_i$. The third term has been modified to depend on molecular orientations α_i [68]. Equations of motion for translational degrees of freedom can be derived as follows [68]:

$$\frac{\mathrm{d}}{\mathrm{d}t}\frac{\partial \mathcal{L}_e}{\partial \dot{\mathbf{s}}_i} = \mathbf{h}^{\mathsf{T}}\mathbf{f}_i \, , \tag{2.46}$$

where forces are defined as $\mathbf{f}_i = \sum_k \mathbf{f}_i^k = \sum_k \sum_{j\neq i} \sum_l \mathbf{f}_{ij}^{kl} = -\sum_k \sum_{j\neq i} \sum_l \partial \mathcal{U}_{ij}^{kl}/\partial \mathbf{r}_{ij}^{kl}$ with k and l enumerating the cartesian directions x, y and z. The resulting equations of motion for translational degrees of freedom are [68]:

$$m_i\ddot{\mathbf{s}}_i = \mathbf{h}^{-1}\mathbf{f}_i - m_i\mathbf{G}^{-1}\dot{\mathbf{G}}\dot{\mathbf{s}}_i \, . \tag{2.47}$$

The equations for angular coordinates, equivalent to those obtained by the constant volume method, are:

$$\frac{\mathrm{d}}{\mathrm{d}t}\mathbf{M}_i = \sum_k \mathbf{p}_i^k \times \mathbf{f}_i^k = \mathbf{N}_i \, , \tag{2.48}$$

where $\mathbf{M}_i$ is the angular momentum of a particle and $\mathbf{N}_i$ is the torque acting on it [68]. Derivation of the equations of motion of simulation box vectors leads to:

$$W\ddot{\mathbf{h}}_{\alpha\beta} = \frac{\partial \mathcal{L}_e}{\partial h_{\alpha\beta}} = \sum_\nu (\Pi_{\alpha\gamma} - p\delta_{\alpha\gamma})\sigma_{\gamma\beta} \, , \tag{2.49}$$

with $\sigma_{\alpha\beta} = \partial V/\partial h_{\alpha\beta} = V(h^{-1})_{\alpha\beta}$ for cartesian directions α, β and γ. Π is the internal stress tensor defined by [68]:

$$\Pi_{\alpha\gamma} = \frac{1}{V}\left\{\sum_i m_i\left(\mathbf{h}\dot{\mathbf{s}}_i\right)_\alpha^{\mathsf{T}}\left(\mathbf{h}\dot{\mathbf{s}}_i\right)_\gamma + \sum_i \sum_k \sum_{j>i} \sum_l \left(\mathbf{f}_{ij}^{kl}\right)_\alpha \left(\mathbf{h}\left(\mathbf{s}_i - \mathbf{s}_j\right)\right)_\gamma\right\} \, . \tag{2.50}$$

Equations 2.49 and 2.50 show that the simulation box can change shape under the imbalance between internal stress and external pressure [68].

2.8.7. Langevin thermostat

The Langevin thermostat makes use of both a stochastic force $\mathbf{R}_i(t)$ and a friction coefficient $\gamma_i(t)$, i.e. the full Langevin equations of motion:

$$\ddot{\mathbf{r}}_i(t) = m_i^{-1}\mathbf{F}_i(t) - \gamma_i(t)\dot{\mathbf{r}}_i(t) + m_i^{-1}\mathbf{R}_i(t) \, , \tag{2.51}$$

where the stochastic forces $\mathbf{R}_i$ have to fulfill the following properties [60]:

- No correlation with velocities $\dot{\mathbf{r}}_i$ and systematic forces $\mathbf{F}_i(t')$ at previous timesteps $t' < t$.

- Vanishing time-average results.

- Random values drawn from a Gaussian distribution with variance $\sigma_i^2 = 2m_i\gamma_i k_{\mathrm{B}}T_0/\delta t$, where δt is the timestep.

- $\langle R_{i\mu}(t)R_{j\nu}(t')\rangle = 2m_i\gamma_i k_{\mathrm{B}}T_0\delta_{ij}\delta_{\mu\nu}\delta(t'-t)$, i.e. no correlation along different cartesian axes μ and ν as well as different times t' and t.

Trajectories generated by Langevin dynamics are able to produce a canonical distribution at temperature T_0 where the energy transfer can be viewed as frictional interaction with a surrounding fluid, the frictional coefficient γ_i of which has to be chosen carefully to avoid long simulation times and systematic energy drift through numerical errors, whereas a too tight coupling would perturb the dynamics of the system [60].

In the limit of $\gamma_i \to 0$, the Langevin dynamics converge towards the classical Hamiltonian dynamics in a microcanonical ensemble.

2.8.8. Other methods

The Andersen thermostat, not implemented in the default version of LAMMPS, is another stochastic method that draws a random velocity from a Maxwell-Boltzmann distribution and applies it directly to a particle depending on the specified Andersen frequency between 0 and 1 [66]. For that, a random number is drawn and if less than the frequency, the new velocity is applied to the particle [66]. This is, just like the previously mentioned naive scaling, a strong-coupling method that potentially introduces unphysical behavior by trapping particles in the configuration space where they cannot leave in an infinitely long timescale as observed by Andersen for Monte-Carlo simulations [66]. Thus, the Anderson thermostat is only recommended for small systems.

As for barostats, there is also a naive scaling method, where the system's box volume is scaled to reach a target pressure [69]. This method will not be discussed, as it is not relevant due to its very rare application.

2.9. Solvent and water models

The topic of water or more generally solvent simulations is vast and a research field on its own [70, 71], with recent emerges in the application of machine learning to improve the quality of simulations and lower the computational power requirements [72]. Fundamentally, solvent models can be broken down into two major categories: Fine- or coarse-grained explicit and implicit solvents, both trying to approximate thermodynamic properties of liquids [70]. The largest field of solvent molecular dynamics is in

(a) Explicit fluid simulation with rigid H_2O-molecules (red and white spheres) permeating the pores of a CNM (gray spheres).

(b) Schematic representation of an implicit fluid simulation (surrounding blue volume) with particles in solution (colored spheres) permeating a CNM (gray spheres).
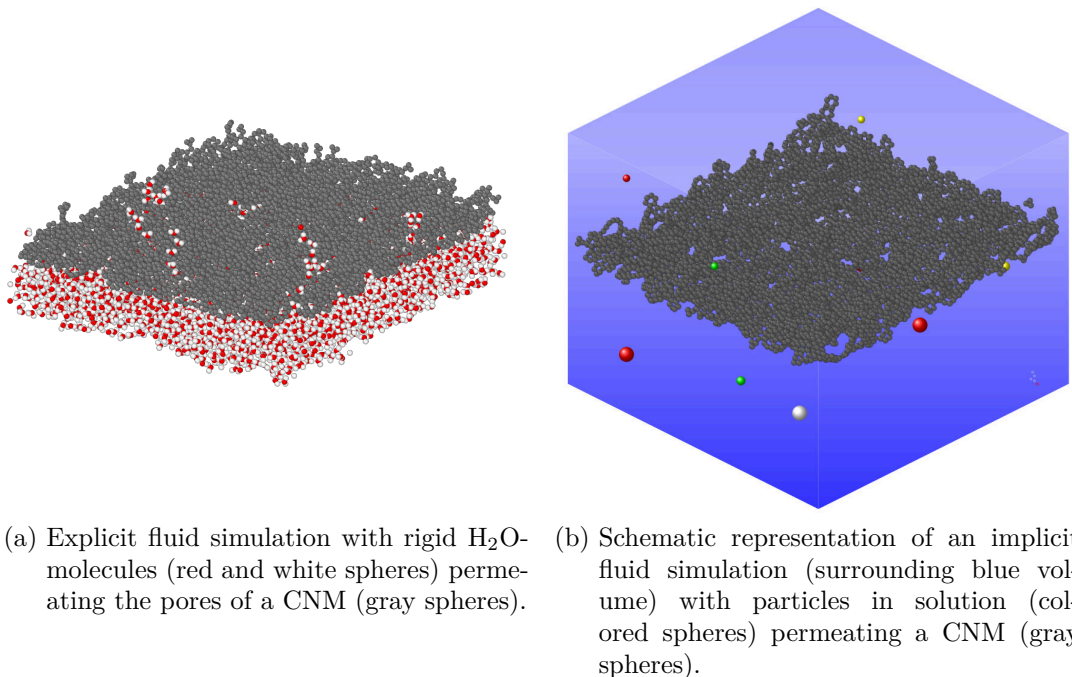
Figure 2.3.: Qualitative comparison of explicit and implicit solvent models.

the simulation of water, e.g. using SPC [73] and TIPNP [74] water models in various parametrizations. Explicit models of solvents, e.g. water, simulate the interaction of atomic components of the solvent, e.g. hydrogen and oxygen for water molecules and their electrostatic potential with the rest of the system, e.g. the carbon atoms in a carbon nanomembrane.

For this type of simulation, detailed knowledge of Coulombic interaction strengths as well as bond angles is essential. For the mentioned example this would mandate parameters for C-C, C-H, C-O, H-H, H-O and O-O interactions as well as long-range electrostatic interactions and dipolar moments of the solvent molecules. These parameters would have to be calculated, e.g. using ab-initio methods or determined experimentally to create the necessary effective potential. As this is often not feasible or data is just not available, one has to resort to mixing various potentials, so called hybrid potentials (*pair_style hybrid* command in LAMMPS) with the need for proper parameters for the mixing contributions [75]. A simplifying reduction in needed computational power can be achieved by coarse-graining through fixing the position of the atoms of everything except the solvent and to consider the solvent molecules as rigid molecules. For this, the interaction between the rigid solvent molecules and the rest of the system is described by electrostatic or Lennard-Jones-like interactions, e.g.

the dipolar electrostatic potential of water interacting with carbon atoms of a carbon nanomembrane. A weaker formulation would allow all but the solvent molecules to move thus allowing for a pressurized system to change shape, bulge or tear apart which again is more computationally expensive. Also, individual solvent molecules might be considered as non-rigid.

These aspects are all well-covered by the SPC and TIPNP models, but differ in details of the parametrization. The SPC water model specifies a 3-site rigid water molecule with charges and Lennard-Jones parameters for each of the three atoms [76], which can be either kept rigid or flexible (*fix shake* command in LAMMPS). The Lennard-Jones and Coulomb terms employ a cutoff of 9 Å [73], but long-range interactions can be included using particle-particle-particle mesh (PPPM) or Ewald summation [76].

TIPNP models are rigid water models defined for a wide range of number of sites N, e.g. a 3-site rigid water molecule for TIP3P similar to the rigid SPC model but with different parameters [77], a 4-site model including one negatively charged dummy atom near the oxygen for TIP4P [78] and a 5-site model with negative charge on dummy atoms representing the lone pair of oxygen atoms for TIP5P [79]. Explicit solvent models are of most interest for permeation studies. Individual solvent molecules are able to interact with the electrostatic potential of e.g. nanopores and channels, therefore allowing to study even the most minuscule flow, e.g. in single-file capillaries where solvent molecules diffuse into a pore and have no possibility to change their relative order thus forming chains of permeating molecules [80].

The other end of the solvent model spectrum is formed by implicit or continuum solvent models. As the name implies, there are no individual molecules or atoms of the solvent, but a continuum volume with similar bulk properties by estimating the free energy of interactions between the solvent and the rest of the system [70]. Examples of these methods are the accessible surface area-based (ASA) method [81] and polarizable continuum model (PCM) [82]. The main purpose of continuum solvent models lies in simulation of solvations in organic and biological systems, e.g. protein transport [81] or multiscale simulations that couple molecular dynamics and hydrodynamics as done for DNA translocation [83].

The permeation study presented in Ch. 10 has been performed using an explicit solvent model.

3. Self-assembled monolayers (SAMs)

The starting point for every carbon nanomembrane is a self-assembled monolayer that allows to tailor thickness and density of the membrane [84]. Self-assembled monolayers are highly ordered aggregations of organic molecules on a substrate [85]. The assembly of the so called precursor molecules is self-initiating and ends by chemisorbtion on a surface with the resulting structure being of the same height as the molecules of around a few nanometers [85]. The SAM on its own would not be mechanically stable when the substrate is removed, e.g. by etching of the substrate.

A broad selection of precursor molecules allows to tailor the monolayer to a specified thickness and purpose. For carbon nanomembranes, aromatic precursor molecules, such as Biphenyl-4-thiol (BPT), 1,1',4',1"-Terphenyl-4-thiol (TPT) and 2-Naphthalene-thiol (NPTH) are of most interest as can be seen from their use in experimental research publications such as Ref. [86]. More details on the structure of the mentioned molecules can be found in the Appendix A.1. A selection of structural formulas of aromatic precursor molecules is depicted in Fig. 3.1. There, each vertex is a carbon (C) atom with hydrogen (H) attached to it, with the latter not being drawn in the schematics. Molecules stick to a substrate, e.g. gold or silver with the help of a chemical group, in this case a sulfur or thiol (-SH) group. A history of CNM preparation from various SAMs will be discussed in Ch. 4. The property of aromaticity and the loss of it in the process of the conversion of a SAM to a CNM is discussed in Ch. 8.

Linear tree-like aromatic precursor molecules can be characterized by their number of carbon rings (hexagons) as their name implies, e.g. two carbon rings for BPT. Then there are also wider molecules such as NPTH and very tall and wide snowflake-like ones which are used less often in experiments.

The substrate plays a key role in the assembly process with the surface structure imprinting a lattice structure onto the monolayer [88]. For CNMs the most used substrate is gold with a hexagonal Au(111) surface structure with a lattice constant of
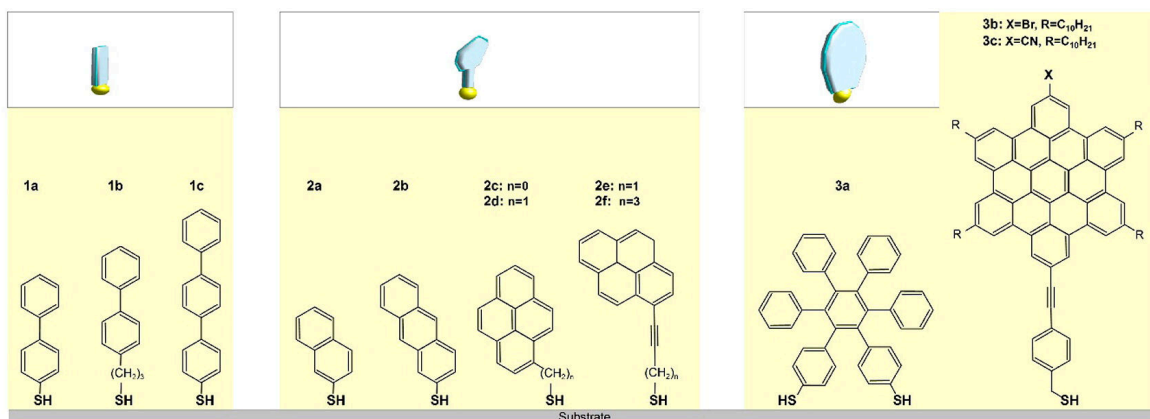
Figure 3.1.: Selection of popular aromatic precursor molecules, taken from Ref. [11].
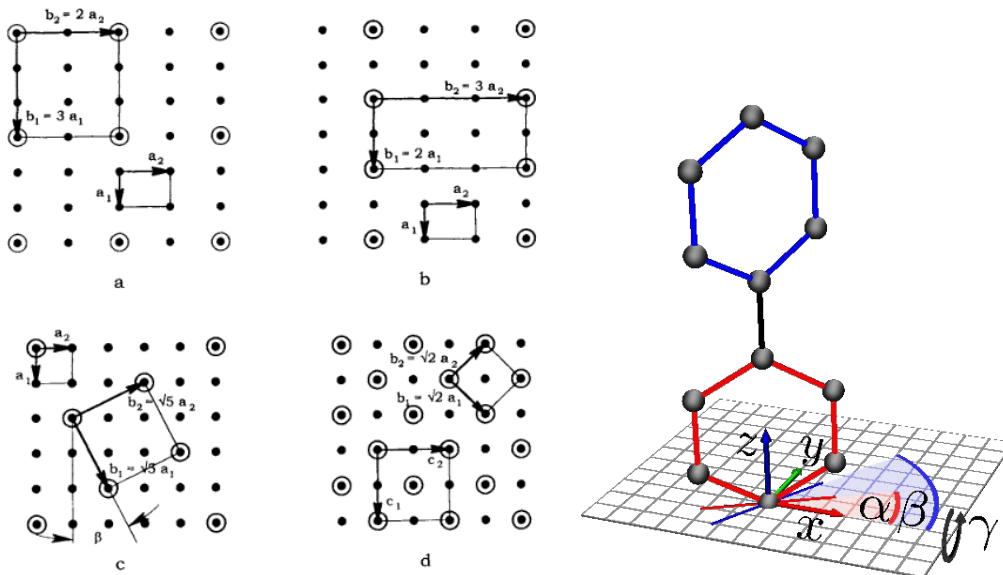
(a) Examples of the Wood notation, taken from Ref. [87].

(b) BPT molecule with skew and twist angles α, β and γ, taken from Ref. [13].

Figure 3.2.: Main characterization geometries of SAMs: Superstructure and molecule skew and twist angles.

2.88 Å [89]. The structure or superstructure of atoms or molecules on a surface can be described by various means, e.g. matrix notation and Wood notation [87], with the latter one being the preferred notation for this thesis and most experimental publications. Some examples of the Wood notation are shown in Fig. 3.2a. The black dots represent an exemplary underlying simple cubic lattice of edge lengths a_1 and a_2 with circles around the dots showing various superstructures, e.g. $(\sqrt{2} \times \sqrt{2})$R45 which is identical to c(2×2) both being depicted in the bottom right of Fig. 3.2a together with their pair of basis vectors $\mathbf{b}_1$ and $\mathbf{b}_2$ in the rotated or stretched coordinate system of the superstructure. Here, R45 is a counterclockwise rotation of 45° of the basis vectors $\mathbf{b}_1$ and $\mathbf{b}_2$ in relation to the simple cubic basis vectors $\mathbf{a}_1$ and $\mathbf{a}_2$ as depicted by the angle β in the bottom left of Fig. 3.2a. A precursor molecule placed at each lattice position might additionally be rotated or skewed about its local x-axis with angle γ as depicted in Fig. 3.2b. For linear molecules there are also twist angles for each ring rotating about the local z-axis. There are two angles α and β for the exemplary BPT molecule, each twisting one of the two rings.

Experimental characterization is possible by various means such as scanning tunneling microscopy for determination of the lattice structure or X-Ray photoelectron spectroscopy for analysis of present molecular orbitals. An overview of experimental studies for both SAMs and CNMs is given in Ch. 5.

4. History and use of carbon nanomembranes (CNMs)

Carbon nanomembranes are mechanically stable and freestanding nanometer-thin membranes [90, 11, 12] with wide-ranging applications such as water desalination through its excellent filtration capabilities [17], as transparent supports for transmission electron microscopy or for use in nanocapacitors [19].

The beginnings of carbon nanomembranes lie in studies of pattern generation with self-assembled monolayers [4, 21], with applications ranging from sensor design to electrochemistry and micromechanical engineering. Grunze, Eck et al. tested aromatic precursor molecules as materials for controlled modification of SAMs and found that the SAM assembled on a gold substrate is converted to amino groups under irradiation with low energy electrons [4, 21, 85]. In the process, the aromatic layer is dehydrogenated and cross-linked [4, 21]. Later on, a universal scheme has been formulated by Turchanin, Gölzhäuser et al. to convert aromatic molecular monolayers into functional carbon nanomembranes as presented in the aptly named publication [11].
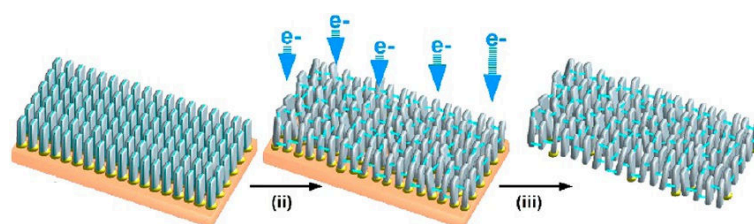
Figure 4.1.: Sketch of the experimental synthesis of a CNM, taken from Ref. [11].

The experimental fabrication process for carbon nanomembranes starts with a self-assembled monolayer of polyaromatic molecules on a gold substrate in high vacuum [11]. The monolayer is then irradiated by a low-energy electron beam accelerating electrons to around 50 eV to 100 eV, effectively rasterizing the SAM with an electron dose of 50 mC/cm^2. This rasterization causes bonds between the carbon atoms to break and thus allowing for new bonds to form, especially with neighboring molecules delivering the necessary glue for cross-linking. Almost all hydrogen inside the SAM is lost during this procedure, leaving only the now cross-linked membrane and the substrate-attaching thiol-group. The resulting CNM is transferred to a TEM grid as support with the help of a PMMA coating and the gold substrate gets etched away [11]. Finally the PMMA coating is dissolved and the membrane dried [11]. When annealing the membrane to over 1000°C, a structural change to pyrolytic graphite is triggered [10].

An example of a macroscopic CNM on a hexagonal TEM support can be seen in the helium-ion microscopy image in Fig. 4.2a. Recent publications [86] tend to soften the strict requirements on the properties of precursor molecules by demonstrating
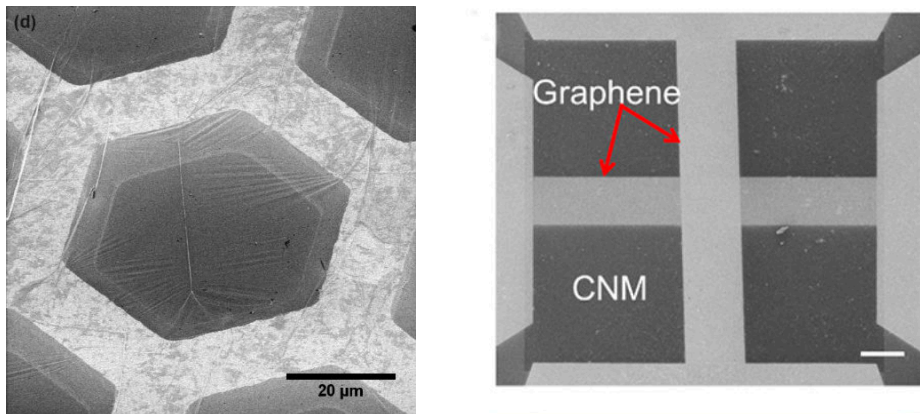
(a) Helium-ion microscopy (HIM) image of a CNM on a macroscopic lateral support structure, taken from Ref. [92].

(b) Helium-ion microscopy (HIM) image of a graphene-CNM nanocapacitor, taken from Ref. [19].

Figure 4.2.: Exemplary helium ion microscopy (HIM) images of CNMs.

porous and mechanically stable membranes being made from molecules attaching to the substrate by another group than thiols, so called aromatic carboxylate precursors. Also, completely non-aromatic, i.e. aliphatic molecules have been demonstrated to result in mechanically stable but brittle nanomembranes [16, 91]. Although almost all CNMs are observed to be mechanically stable, they have an unexpectedly low Young's modulus of the order of 10 GPa [14] when compared to other carbon based structures such as graphene (1 TPa [15]), carbon nanotubes ($\approx$ 1.2 TPa [93]) and diamond ($\approx$ 1.15 TPa [94]), with aliphatic membranes coming in at only 0.5 GPa [16]. The experimental means of mechanical characterization are explained in detail in Ch. 5.

A promising usecase of CNMs is water filtration. It is observed that these membranes are very effective at filtering contaminations from water, thus e.g. allowing for very energy efficient desalination when compared to traditional means, e.g. boiling salt water by burning fossil fuels, with a filtration property that is highly selective and sensitive to the permeating gas or liquid [17]. Carbon nanomembranes show potential of being used as dielectric components in environmentally friendly energy storing all-carbon nanocapacitors [19]. Finally, the mechanical stability allows the membranes to be used as supports for visible light microscopy or TEM images due to the membranes' transparency in these spectra [95].

From the experimental point of view, the number of analysis methods offer to study a wide spectrum from mechanical to electronic properties of the membrane. Most of them allow detailed characterization of the membrane with respect to bond types, elemental composition, hydrogen loss and mechanical properties. The latter category is comprised of many industry-standard methods from materials science like nanoindentation and bulge testing which have been proven to work for many materials. However, mechanical characterization of nanomaterials, especially nanometer-thin carbon nanomembranes, can be challenging. Methods for experimental studies will be discussed in the following chapter outlining potential pitfalls and shortcomings, one of the most prominent being the impossibility of determining the internal structure of CNMs.

5. Experimental characterization of SAMs and CNMs

This chapter tries to give an overview of some of the most used and important experimental methods for characterization of self-assembled monolayers and carbon nanomembranes that is by no means complete. Also, the possibility of reproducing these experiments using computer simulation is discussed where appropriate. Due to the lack of electronic properties, most classical molecular dynamics simulations are limited to mechanical properties, e.g. the Young's modulus or some limited vibrational spectra as well as thermal transport properties.

5.1. Infrared (IR) and infrared reflection absorption spectroscopy (IRRAS)
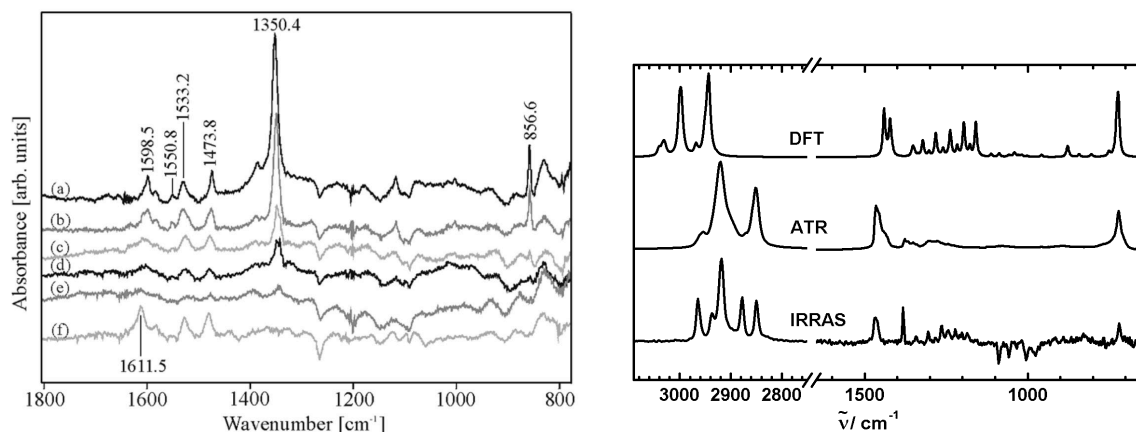
(a) IR spectra of a 4'-nitro-1,1'-biphenyl-4-thiol (NBPT) SAM (a) and after irradiation (b) to (e) with increasing electron dose, taken from Ref. [21].

(b) IRRAS spectrum of a self-assembled dodecanethiolate monolayer on gold, taken from Ref. [96].

Figure 5.1.: Typical IR and IRRAS spectra of SAMs before and after irradiation.

Infrared reflection absorption spectroscopy (IRAS, IRRAS) is a non-destructive optical technique to study thin films of only a few Angstroms adsorbed on reflective substrates such as gold [97], thus being ideally suited for SAM and CNM characterization. It can be used to get an insight on molecular composition, degree of order of the molecules and the relative angle between molecules and substrate [96] as depicted by the angle γ in 3.2b. The difference between common IR spectroscopy and IRRAS is that for IRRAS the measurement is done via reflection at a grazing angle demanding

highly sensitive sensors due to the small layer heights of SAMs and CNMs [96]. Standard IR spectroscopy exploits radiation absorption instead and measures the difference of IR signals of the substrate by itself and the substrate with a monolayer on top or uses substrates with a low interference and featureless background signal [98]. It also finds much wider application in analytical chemistry than IRRAS. Both methods rely on excitation of electromagnetic dipoles in the material that are closely related to molecular vibrational spectra thus showing characteristic peaks indicating the molecular composition of the material [99]. Fig. 5.1a shows IR spectra of 4'-nitro-1,1'-biphenyl-4-thiol (NBPT) for the pristine SAM (a) and irradiated membranes (b) to (e). For example, the aromatic ring stretching modes at 1533.2 cm^{-1} and 1473.8 cm^{-1} can be observed to decrease with increasing electron dosage [21]. A typical IRRAS spectrum for a dodecanethiolate monolayer on gold is depicted in Fig. 5.1b.

Computer simulation of vibrational spectra is possible by means of Fourier-transformed auto-correlation functions of dipole moments performing best for ab-initio methods [100]. Results of classical molecular dynamics simulations as required for macroscopic CNMs due to the number of atoms might be poor [101, 102].

5.2. Scanning electron (SEM) and helium ion (HIM) microscopy
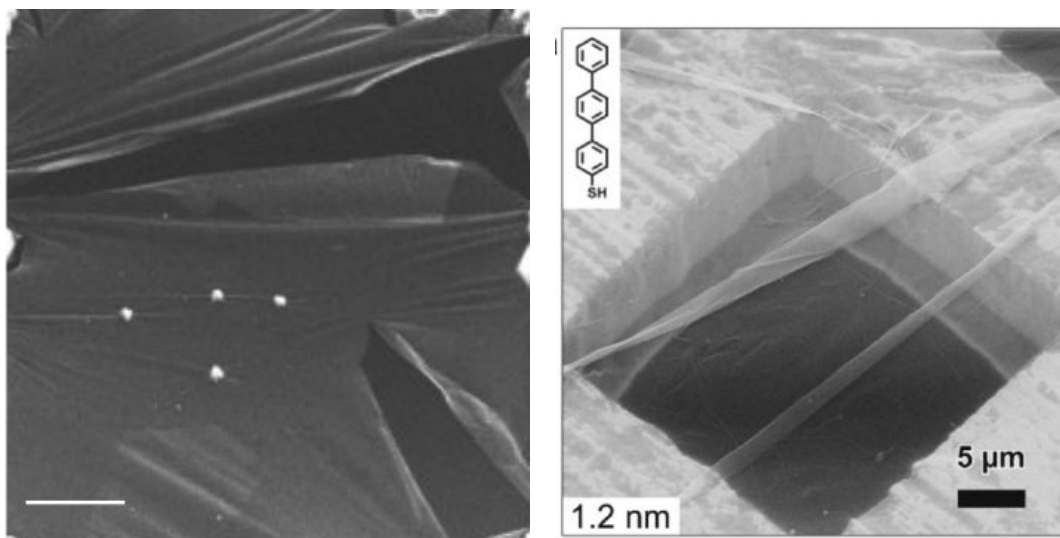
(a) Scanning electron micrographs (SEM) of a CNM, taken from Ref. [85].

(b) Helium ion micrograph (HIM) of a TPT-CNM on a gold TEM support, taken from Ref. [11].

Figure 5.2.: Comparison of SEM and HIM imaging methods.

Scanning electron microscopy (SEM) is an industry standard imaging method for sub-micrometer surface structures that have to be conductive and vacuum friendly [103]. Conductivity is often achieved by drying the sample and applying conductive coatings potentially obscuring subtle surface details [103]. The method is applicable to many materials with biological and insulating materials being the most problematic. The basic principle of SEM is rasterization of the specimen with an electron beam whose diameter is one inherent limiting factor of image resolution [104]. The most common modes of operation of a SEM are based on the intensity of secondary and backscattered electrons as well as X-ray signals being probed, with the probe current being another limiting factor [104]. An example of SEM being used to image a cross-linked membrane can be seen in Fig. 5.2a showing a ruptured membrane, demonstrating the features best resolvable by SEM, e.g wrinkles whereas details of the membrane are lacking.

The shortcomings of SEM are improved by helium ion microscopy (HIM) with advances in minimized damage to the specimen, higher contrast and resolution improvements to structures as small as 5 Å without the need of conductive surface coatings as well as increased depth of field [103]. Instead of electrons, a HIM uses accelerated helium ions focused on the specimen, producing secondary electrons and ions depending on the beams geometry as well as the specimen's topography and electronic properties [105]. Fig. 5.2b shows a helium ion micrograph of a free-standing TPT-CNM on a gold TEM support [11]. Not only the wrinkles but small surface structures of the membrane are resolved in this image.

5.3. Scanning tunneling microscopy (STM)
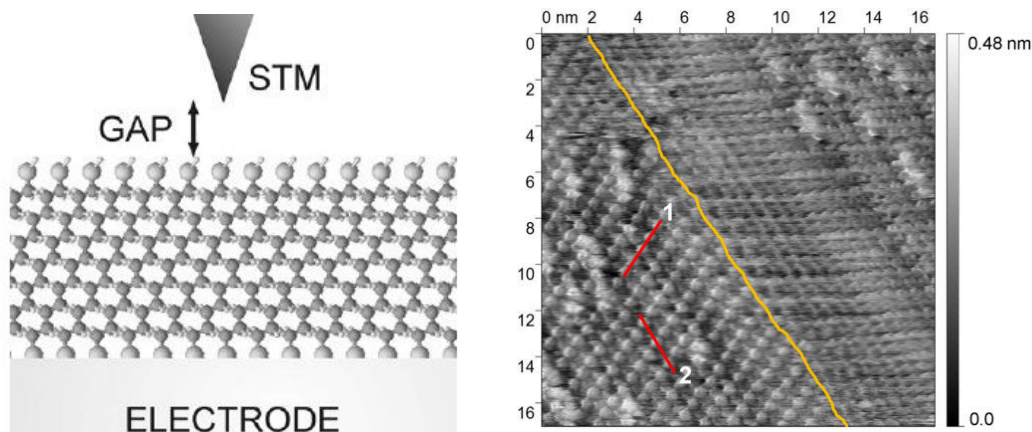
(a) Schematic representation of scanning tunneling microscopy (STM), taken from Ref. [106].

(b) Scanning tunneling microscopy (STM) image of a TPT-SAM, taken from Ref. [17].

Figure 5.3.: Schematic representation of STM and exemplary imaging result.

Scanning tunneling microscopy is a means of electron microscopy for imaging of surfaces at atomic scales based on the principle of quantum tunneling [107]. A bias voltage is applied between a conducting, e.g. metallic or semiconducting surface and a tip placed only a few Angstroms above the surface thus allowing electrons to tunnel the vacuum, effectively probing the density of states of a material [108]. Rasterizing the surface with the tip while recording the resulting tunneling current allows to produce topographical images of the surface with depth resolutions down to 0.01 nm and lateral resolutions of 0.1 nm [108]. STM is besides atomic force microscopy a viable but limited resource to image the surface of SAMs and CNMs, as shown in the STM image of a TPT-SAM in Fig. 5.3b. There, the regular structure of the molecule assembly is clearly visible.

STM is limited by the necessity of a very clean surface [107] which is problematic for CNMs due to residual PMMA coatings from the transfer process. When STM is used successfully, it gives insights into the height profile as encoded by the grayscale colors, possible defects and general structural properties, e.g. the lattice structure of the molecules in the SAM in Fig. 5.3b.

5.4. Atomic force microscopy (AFM)
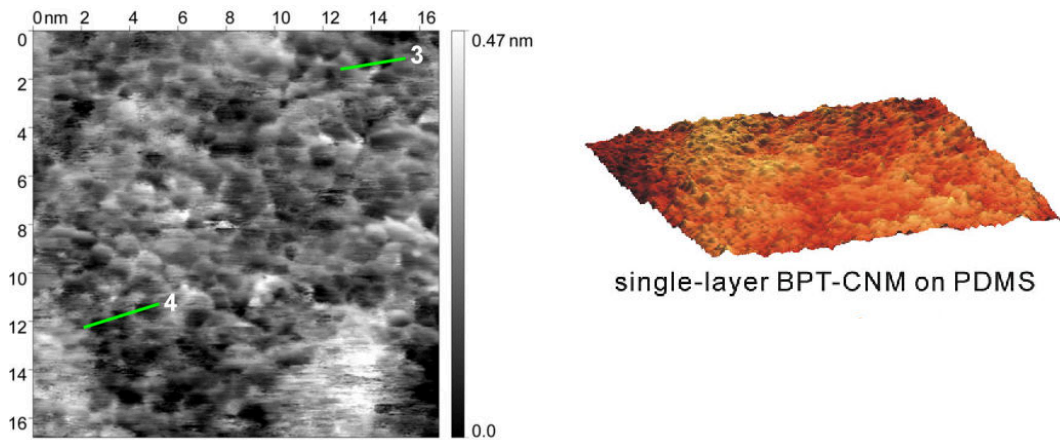
(a) Tapping mode atomic force microscopy (AFM) image of a TPT-CNM, taken from Ref. [17].

(b) Tapping mode AFM topography image of a single-layer BPT-CNM, taken from Ref. [109].

Figure 5.4.: Different visual representations of AFM images.

Similar to STM, atomic force microscopy (AFM) is a scanning probe microscopy method for surface profile imaging with a horizontal resolution of about 0.2 nm and vertical resolution of 0.01 nm [108]. The so called cantilever, a probe with a sharp, at the tip only a few atoms or even single atom wide probe rasterizes the surface by getting deflected through atomic interactions with the material, e.g. through Pauli exclusion or Coulomb repulsion [110]. Measurements of the bending of the tip are possible with the help of a laser beam getting reflected by the cantilever [110].

The main modes of atomic force microscopy are contact mode, tapping mode and non-contact mode. They differ in accuracy and potential in damaging the specimen, e.g. by imprinting the cantilever into the material in contact mode. Imaging of carbon nanomembranes is often done using tapping mode AFM which tries to limit surface damage. Fig. 5.4a shows a tapping mode AFM image of a TPT-CNM. As can be seen by the color coding from black to white, a maximum height of 0.47 nm is resolved with semi-circular areas at close to 0 nm being counted as pores. An exemplary pore distribution taken from Ref. [17] is given in Fig. 5.5. The authors of the paper from which the images are taken [17] explain the property of high permeability of CNMs with the mentioned AFM image and estimated pore size distribution which is sensible but comes with a caveat.

Taking the parameters of a TPT-SAM defined by an angle $\gamma = 20°$ (refer to Ch. 3 and Appendix A.1) and a regular TPT molecule height of at least 15 Å would suggest that ei-
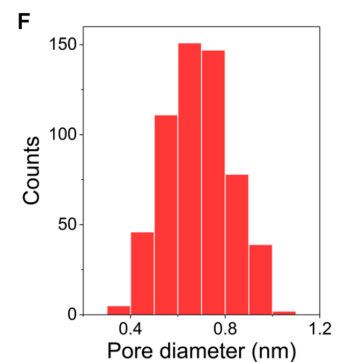
Figure 5.5.: Estimated pore diameter distribution, taken from Ref. [17].

ther many carbon atoms are lost during the irradiation process which contradicts XPS measurements or that the AFM is not able to resolve proper pores, i.e. cavities that reach from the top to the bottom and especially no slanted, organically shaped pores [17]. The 3D surface rendering of an atomic force micrograph in Fig. 5.4b, taken from Ref. [109] shows another popular goldish color coding of AFM images and allows for a better visual feel for the surface roughness and resolvability of pores. The latter cannot be easily concluded from this topographic perspective.

The formation and function of pores will be discussed in Ch. 5.13 with regard to permeability.

Atomic force microscopy images are not inherently possible by means of classical molecular dynamics where all positions and velocities of atoms or molecules are known exactly at a particular timestep, i.e. molecular dynamics has ideal imaging resolution. A quantum mechanical approach considering the cantilever as a classical object of only electrostatic forces has been suggested in Ref. [111], which would be impossible for the lateral extent of the CNMs discussed in this thesis. To simulate the limitations of the previously discussed AFM images, especially with regard to pore detection, which is most likely due to the cantilever not reaching the true bottom of the membrane, an approach for a qualitative and artistic method for generating AFM images based on exact atom positions is presented in Ch. 9.

5.5. Thermal desorption spectroscopy (TDS)
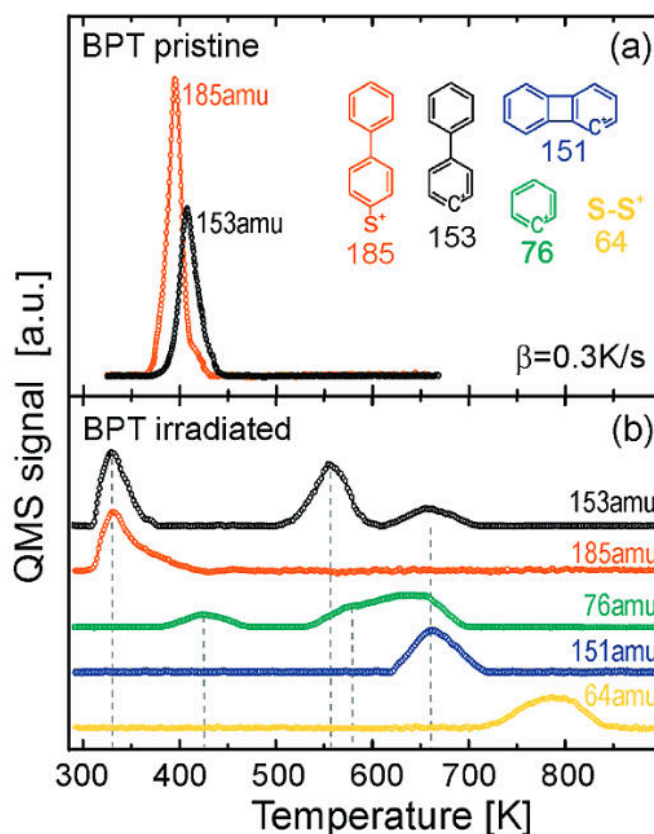
Figure 5.6.: Thermal desorption spectroscopy (TDS) of a pristine BPT-SAM (a) and after irradiation (b) for various characteristic masses, taken from Ref. [20].

Thermal desorption spectroscopy (TDS) is a temperature dependent method to study adsorption, desorption and the reaction of adsorbed atoms or molecules on surfaces [112]. The rate of desorption, i.e. the release of atoms or molecules from the surface is often measured using a quadrupole mass spectrometer, an example being shown in Fig. 5.6 for a pristine BPT-SAM and the irradiated SAM. The method allows to identify the molecular composition of the membrane. Each peak indicates the existence of a particular molecule. For example, the red peak at 185 amu in Fig. 5.6 (a) corresponds to the mass of the entire pristine BPT molecule and the black peak at 153 amu is the BPT molecule without the thiol group, indicating different desorption channels due to the slightly different temperature [20]. The spectrum for the irradiated membrane shows shifted peaks for the BPT and thiol-less BPT as well as new peaks, all of which is related to the cross-linking process while some of the initial SAM's BPT molecules might stay intact [20]. Overall, there is a drastic decrease of signal strength for the irradiated membrane [20].

As for computer simulations, e.g. simulated hydrogen thermal desorption spectra of metal-organic frameworks by means of Monte Carlo simulation have been shown to be in qualitative agreement with experimental results [113].

5.6. X-ray photoelectron spectroscopy (XPS)
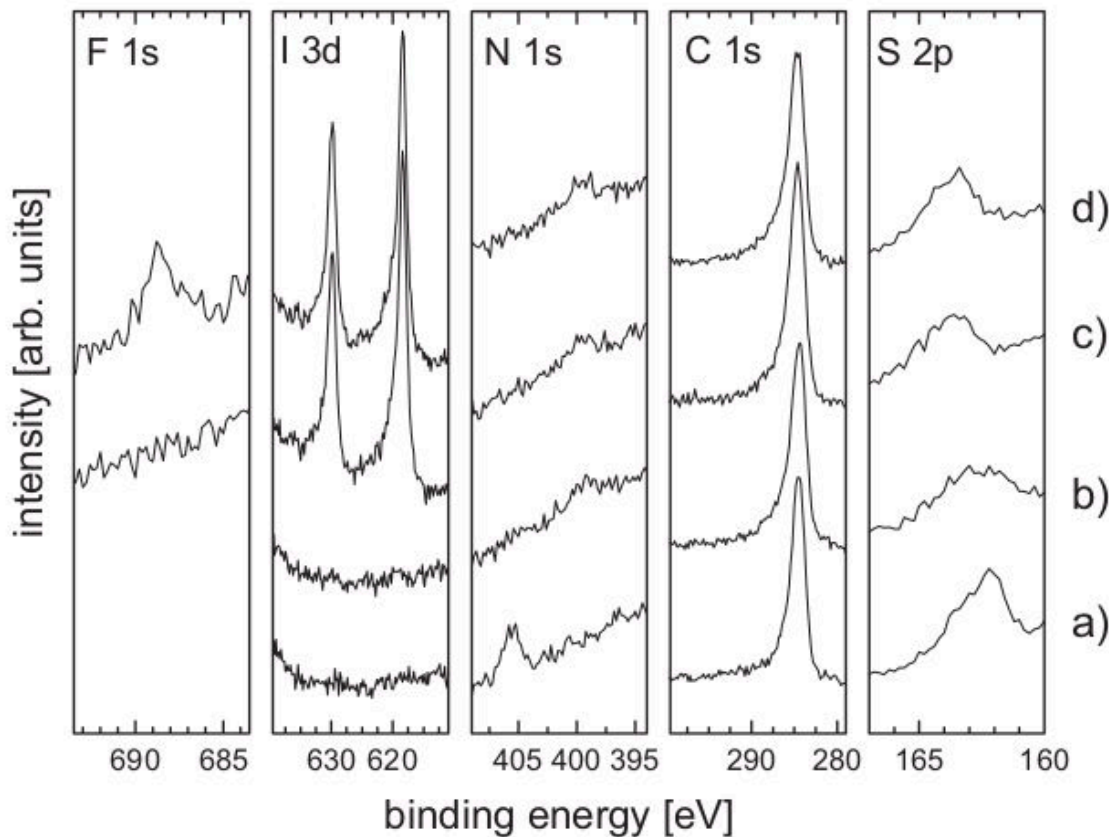
Figure 5.7.: XPS spectra of 4'-nitro-1,1'-biphenyl-4-thiol (NBPT) from pristine SAM a) to irradiated and chemically treated membranes after irradiation b) - d), taken from Ref. [85].

X-ray photoelectron spectroscopy (XPS) is another method for surface characterization based on the measurement of emitted electrons after irradiation of a material with X-rays able to reveal chemical state information except for elemental detection of hydrogen and helium [114]. It is based on the photoelectric effect where the sample is irradiated with soft X-rays of energies below 6 keV, completely transferring their energy to bounded electrons of the material which are analyzed with regard to their kinetic energy [114], i.e.

$$h\nu = \text{BE} + \text{KE} + \Phi\,, \tag{5.1}$$

where BE is the binding energy and KE the kinetic energy of the emitted electron. Φ is a spectrometer-specific work function describing the difference between the vacuum and Fermi level [114]. Knowledge about the X-ray photon energy $h\nu$ and the work function Φ as well as measurement of the kinetic energy KE of the emitted electrons then allows to determine the binding energy BE and the corresponding intensities [114]. An example can be seen in Fig. 5.7 for a molecule similar to BPT, 4'-nitro-1,1'-biphenyl-4-thiol (NBPT) on a gold Au(111) support. XPS allows to break down the chemical composition of the SAM and the resulting membrane. Spectra are often named after atom

and electron level the signal originates from, e.g. spectra for the existence and relative abundance of C 1s, S 2p and N 1s as components of the precursor molecule as well as F 1s and I 3d as part of the chemical treatment constituents [85]. The characteristic C 1s peaks change only little when the SAM is irradiated while there is a change for the thiol group indicating a breakup of S-Au bonds [85, 115] and the formation of S-S bonds. When the membrane is chemically treated with iodine (Fig. 5.7 c)) or trifluoroacetic acid (Fig. 5.7 d)), iodine and fluor atoms are embedded into the highly reactive surface of the membrane, leading to distinct peaks in the corresponding spectra [85]. The relatively small change in signal intensity for the C 1s peak was studied

Table 5.1.: Results from XPS measurements, taken from Ref. [11].

	SAM thickness	CNM thickness	C loss
BPT	10 Å	9 Å	5 %
TPT	13 Å	12 Å	4 %
NPTH	6 Å	6 Å	9 %

in detail for BPT, TPT and NPTH in Ref. [115] and is shown in Tab. 5.1. Since there is no experimentally observed change in lateral dimensions of the membrane, the decrease in C 1s peak height after irradiation of the SAM is related to a loss of carbon atoms in the process due to high excitation energies leading to dissociation of atoms and can thus also be related to the thickness of the membrane when also accounting for the Au 4f spectrum of the gold support [115]. The witnessed loss of carbon is less than 10 % for the largest studied molecule NPTH and less than half of that for smaller molecules such as BPT and TPT, thus leading to the conclusion that almost no carbon is lost during the process.

Experimental XPS results help in modeling the theoretical formation of carbon nanomembranes e.g. with respect to radiation intensity and whether or not to allow carbon atoms to be lost. These aspects will be discussed in detail in Ch. 6 about the theoretical simulation setup.

5.7. Near edge X-Ray absorption fine structure (NEXAFS)
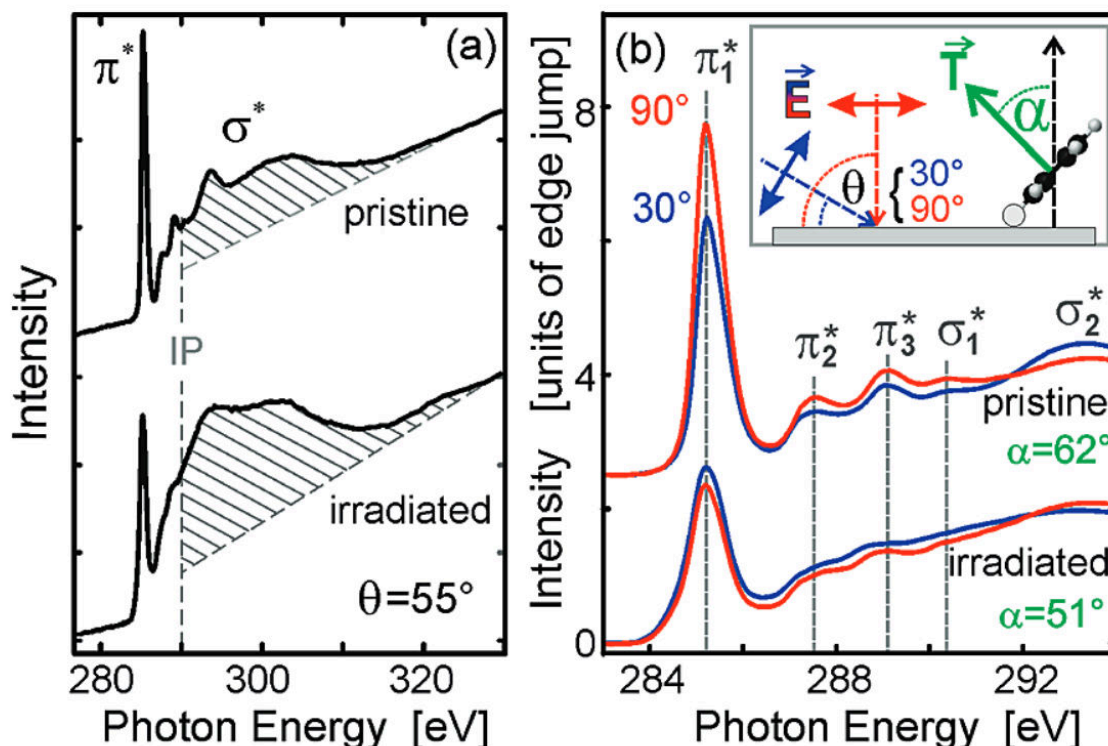
Figure 5.8.: Carbon C 1s edge NEXAFS of pristine and irradiated BPT-SAMs: (a) non-normalized spectra at an incident angle of 55° and (b) angular dependence of magnified π^*-region, taken from Ref. [20].

X-ray absorption fine structure spectroscopy (XAFS) allows to study the chemical state and local atomic structure of an atom species, sensitive to oxidation state, coordination chemistry, distances as well as surrounding atoms [116]. It relies on the angle-dependent absorption of X-rays at energies near the core-level binding energies of an atom [116], thus called near edge XAFS or NEXAFS.
For CNMs in particular, NEXAFS allows to study the effect of irradiation of the SAM and determination of orientational ordering by means of C 1s X-ray absorption [20]. For example, peaks between 285.2 eV and 289.1 eV in the spectra shown in Fig. 5.8 indicate excitations of C 1s electrons into unoccupied π^* orbitals, whereas peaks at 290.4 eV and 293.4 eV are indicative of σ^* resonances [20]. When comparing raw NEXAFS data for the pristine SAM and the resulting CNM, there is a massive decrease in signal intensity which can be attributed to a partial loss of aromaticity, i.e. very likely to the breakup of carbon hexagons [20]. Also there is an overall broadening of the peaks best observed in Fig. 5.8 (b) which also emphasizes the angle dependence of X-ray absorption for two angles as depicted in the inset of the experimental geometry [20].

NEXAFS data can be used to motivate the aspect of loss of aromaticity in molecular dynamics simulations in addition to IRRAS spectra as presented in Ch. 5.1.

5.8. High resolution electron energy loss spectroscopy (HREELS)
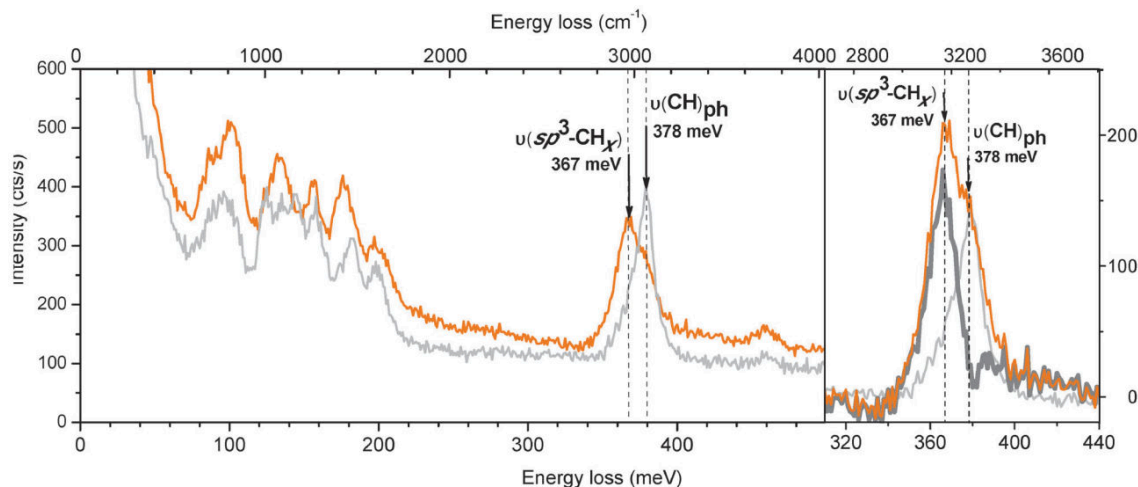
Figure 5.9.: Comparison of HREELS energy loss spectra of a pristine TPT-SAM (light gray curve), after irradiation (orange curve) and difference signal (dark gray curve) at 6 eV, taken from Ref. [117].

High resolution electron energy loss spectroscopy (HREELS) is a method for vibrational spectroscopy of surfaces and molecules adsorbed to a surface using a beam of accelerated electrons with energy in a range of 2-20 eV as a probe in the process of which the electrons lose up to 500 meV of their energy through elastic or inelastic scattering from a surface or adsorbed molecules [118]. This characterization of most common vibrational modes as well as their overtones is limited by how well the electron beam is focused and by the energy delta or width of the accelerated electrons of around 5 meV [118].

The energy loss spectrum of a pristine TPT-SAM on gold taken at an electron energy of 6 eV as depicted by the light gray curve in Fig. 5.9 shows characteristic peaks at various energies that can be associated with a broad selection of vibrational modes [117]. Those at 182 meV and 378 meV can for example be attributed to $\delta\,(\mathrm{CH})_{\mathrm{ph}}\,/\nu\,(\mathrm{CC})_{\mathrm{ph}}$ deformation or stretching modes and $\nu\,(\mathrm{CH})_{\mathrm{ph}}$ stretching modes, respectively [117]. After irradiation, the signal is overall decreased and peaks are broadened (orange curve). The main difference however lies in the peak at 367 meV, while the signal at 378 meV decreased, a zoomed-in difference signal is shown in the right of Fig. 5.9 (dark gray curve). The new peak can be associated to a $\nu\,(\mathrm{sp}^3\text{-}\mathrm{CH}_x)$ stretching mode of sp³-hybridized CH_x groups, i.e. indicating cross-linking further supported by the decrease in signal intensity between 124 meV and 144 meV whose peaks are indicative of phenyl rings [117].

Similar to IRRAS and NEXAFS, HREELS can be an indicator for an undergoing modification of a SAM through irradiation towards a CNM, especially with regard to a loss of aromaticity, supporting molecular dynamics simulations setup parameters.

5.9. Bulge testing
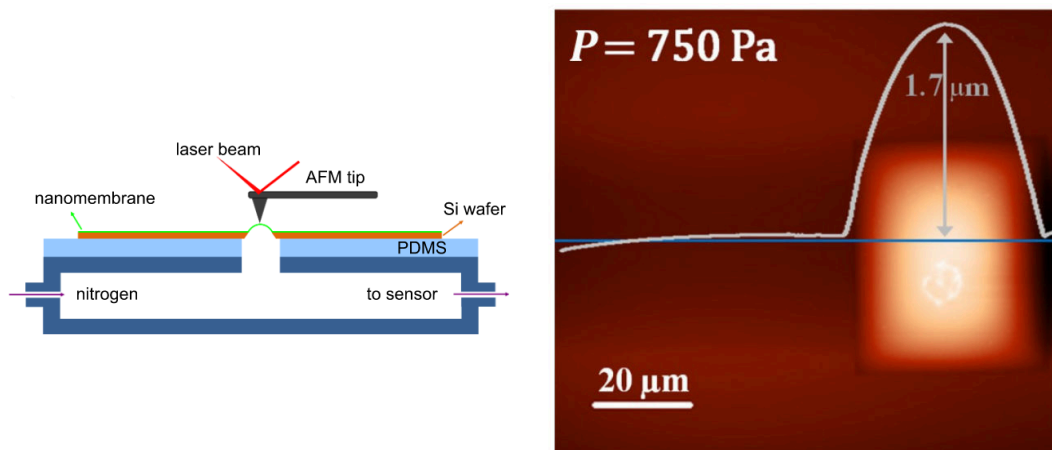
(a) Schematic experimental bulge testing setup using a pressurizable cell and an AFM tip, taken from Ref. [14].

(b) AFM image of a pressurized BPT-CNM, taken from Ref. [14].

Figure 5.10.: Bulge testing schema and AFM deflection result for a BPT-CNM.

A key deciding factor for use of CNMs as filters or sensors lies in the mechanical properties of the membrane which can be investigated by various means, an overview of which is given in Ref. [119].

Since clamping the membrane for the typical stress-strain analysis is unfeasible, other widely used methods to characterize mechanical properties of freestanding membranes must be employed, one of which is bulge or blister testing [14]. A schematic representation of the experimental setup is shown in Fig. 5.10a. The membrane is adhered to a chamber with an orifice getting pressurized from below [14]. The membrane gets deflected by application of nitrogen gas pressure and deflection height is measured using laser interferometry of a deflected atomic force microscopy cantilever in either tapping or contact mode or optical microscopy with resolutions in the range of nano- to micrometers [14]. An exemplary AFM image of a pressurized BPT-CNM can be seen in Fig. 5.10 indicating a maximum deflection height of 1.7 μm over a rectangular orifice [14].

Deflection height is recorded for various applied pressures measured indirectly through flow measurement and data can be fitted by the following analytical formula supported by FEM calculations [120]:

$$p = c_1 \frac{\sigma_0 t}{a^2} h + c_2 \frac{Et}{a^4(1-v)} h^3 , \qquad (5.2)$$

ultimately delivering the Young's modulus E as a measure of elasticity of the membrane [14]. The Young's modulus will be discussed in Ch. 6.2 on its own as it is a main topic of this thesis enabling the comparison of modeled and real membranes.

Bulge testing can be performed with a single layer CNM and yields a Young's modulus in the range of $9-19$ GPa for BPT, TPT and NPTH membranes, respectively [119]. Although bulge testing is a well-known characterization method in materials science, it should be noted that for membranes as thin as CNMs and relatively huge deflections

in the μm-range, the membrane might be destroyed in the process of pressurization, leading to e.g. almost unnoticeable pressure loss when the membrane ruptures, unintentionally reducing the Young's modulus.

Classical molecular dynamics simulations of bulge testing have been performed for graphene enabled through heavy use of symmetries reducing the computational cost and an analytical expression for the relation between applied pressure and deflection [121], both of which is not possible for CNMs.

5.10. Nanoindentation
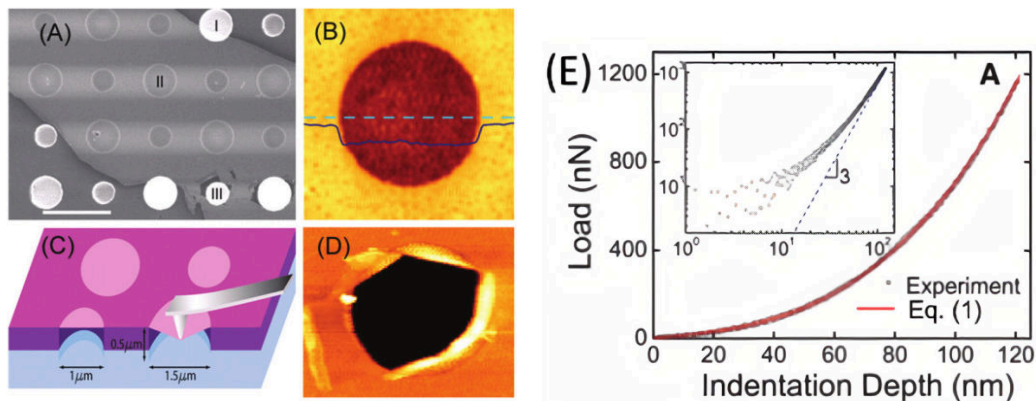
(a) Exemplary nanoindentation schematic (C), STM image of the experimental setup of circular freestanding graphene membranes (A) and AFM images of graphene nanoindentation (B, D), taken from Ref. [15].

(b) Loading/unloading curve with regard to indentation depth, taken from Ref. [15].

Figure 5.11.: Schematic representation of graphene nanoindentation and measured loading/unloading curves.

Nanoindentation, or more specifically AFM-based nanoindentation can be used to measure the hardness of thin films and nanolayers [119], e.g. multi-layer graphene [15] or multi-layer CNMs [119] by pushing an AFM cantilever into the material and measuring the resulting force on the cantilever. An exemplary setup of AFM-based nanoindentation of a graphene membrane is shown in Fig. 5.11a and the measured force-profile while loading and unloading the cantilever is presented in Fig. 5.11b. Similar to bulge testing, this data has to be fitted using a model formula that must include both the membrane geometry, e.g. clamped circular or beam-shaped, potentially leading to non-linear terms for thick membranes under deflection as well as the indenters geometry, all of which being of the form $F = \alpha \cdot \delta + \beta \cdot \delta^3$, again motivated by FEM calculations [119]. The Young's modulus is contained in α and β depending on the system's geometry. Often, the effective 2D-Young's modulus $E^{2D} = E \cdot t$ with t the sometimes artificially chosen thickness of the membrane is calculated. For graphene, the resulting Young's modulus is close to the expected value of 1000 GPa [119] with the thickness t chosen as either the graphite interlayer spacing of around 0.334 nm or carbon-carbon bond length 0.142 nm [38].

For CNMs, four membrane layers are needed for proper measurement, leading to a total Young's modulus of 46 ± 10 GPa [119], i.e. $E \approx 12.5 \pm 2.5$ GPa for a single CNM in good agreement with bulge testing results. As depicted by subfigure (D) in Fig. 5.11a, the membrane can be destroyed in the process of indentation, potentially leading to inelastic softening and thus underreporting the Young's modulus [121].

Classical molecular dynamics simulations of CNM nanoindentation are presented in Ch. 7.

5.11. Electronic transport measurements

Apart from mechanical properties, the description of molecular composition and limited insights to internal structure, there are also aspects related to e.g. electronic transport and capacitance, promising the use of CNMs in nanoelectronics.

Measurements of electronic transport and tribological properties of pristine and ir-

(a) Bias voltage-current histograms across different types of junctions measured with CP-AFM for a NBPT-SAM (left) and the resulting CNM (right), taken from Ref. [122].

(b) Bias voltage-current density across different types of junctions measured by the EGaIn method, taken from Ref. [122]
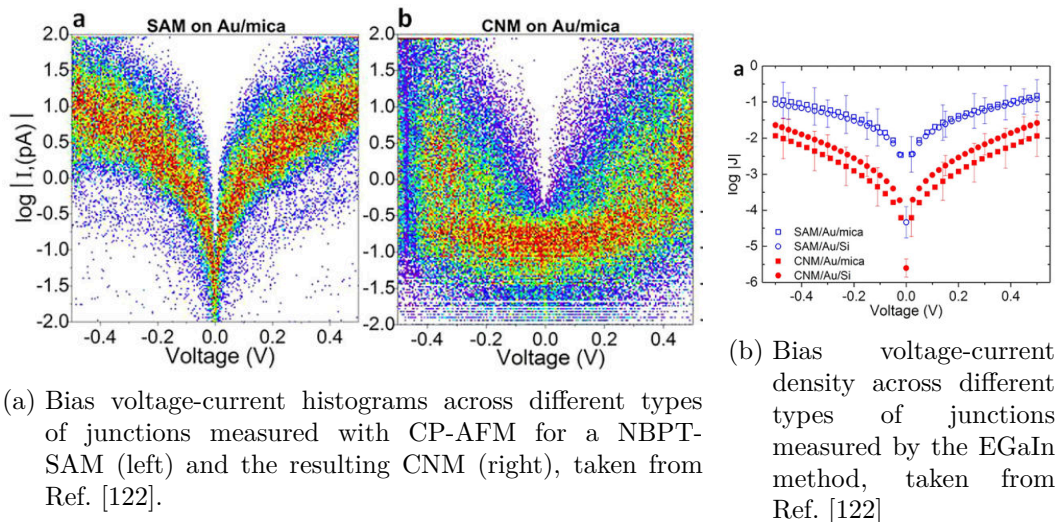
Figure 5.12.: Comparison of CP-AFM and EGaIn measurements of electronic transport through a NBPT-SAM and CNM.

radiated NBPT-SAMs have been performed using conductive probe atomic force microscopy (CP-AFM) and a eutectic Ga-In (EGaIn) top electrode in Ref. [122] to give both qualitative and quantitative insights depending on the method employed.
CP-AFM measurements were performed by first recording frictional images by forward and backward scanning determining lateral force signals in contact mode AFM to estimate the contact area for current density calculations [122]. For measurement of the latter, a bias voltage is applied between the AFM tip and the substrate supporting the SAM or CNM, respectively. The accumulated results of many measurements due to high variance between samples is shown in Fig. 5.12a. For more quantitative measurements, an eutectic Ga-In top electrode was placed on top of the SAM or CNM which forms a molecular junction with the membrane and the support material [122], the results of which are shown in Fig. 5.12b for various junctions.

It was found using both methods that there is a decrease in conductance after irradiation of the SAM related to modifications of molecular structure and electronic coupling of molecules to the substrate [122]. Conductance measurements have been shown to be dependent on the support material used, surface roughness of the membrane as well as the inherent effective contact area of the methods employed [122].

Although electronic properties are not at all feasible with classical molecular dynamics simulations, conductivity measurements show dependence on internal and surface structure of a CNM of which experimental results are limited.

5.12. Capacitance measurements in nanocapacitors
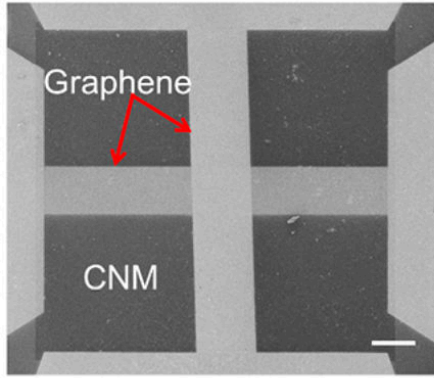
(a) HIM image of a capacitor made of a six-layer CNM as dielectric and trilayer graphene electrodes, taken from Ref. [19].
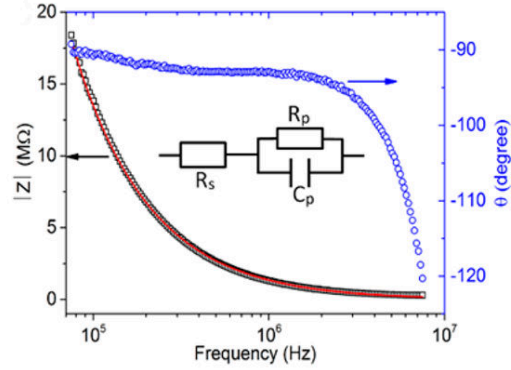
(b) Impedance spectra of a graphene/6-TPT/graphene capacitor, taken from Ref. [19].

Figure 5.13.: Finished nanocapacitor after lithography and stacking in a) and exemplary impedance spectra in b).

The overall decrease in conductivity as discussed in the previous chapter leads to the potential use of CNMs as a dielectric component in capacitors. Up to 1200 μm^2 large all-carbon capacitors (ACCs) have been fabricated from graphene and multi-layer stacks of CNMs with a dielectric constant of 3.5, dielectric strength of 3.2 MV/cm and a capacitance density of around 0.3 $\mu F/cm^2$ as presented in Ref. [19].

Fig. 5.13a shows a HIM image of a finished nanocapacitor that can use either trilayer or pyrolyzed graphitic carbon (PGC) as the top and bottom carbon-based electrode and the CNM being used as a dielectric. Assuming a series resistance from the top and bottom graphene ribbons to the impedance spectrometer R_S, and a capacitor-resistor model for the nanocapacitor consisting of C_P and R_P, the total impedance can be expressed by

$$Z(\omega) = R_S + \left(R_P^{-1} + (i\omega C_P)^{-1} \right)^{-1} , \qquad (5.3)$$

and allows to find the capacitance of an ACC [19]. For the impedance spectra depicted in Fig. 5.13b this results in a capacitance of 85 fF for the trilayer graphene variant, with PGC ACCs coming in at 0.29 pF [19]. From these results, the dielectric constant of the CNM can be derived from the formula for a capacitor with dielectric $C = \varepsilon_0 \varepsilon_r (A/d)$.

5.13. Liquid/gas permeation
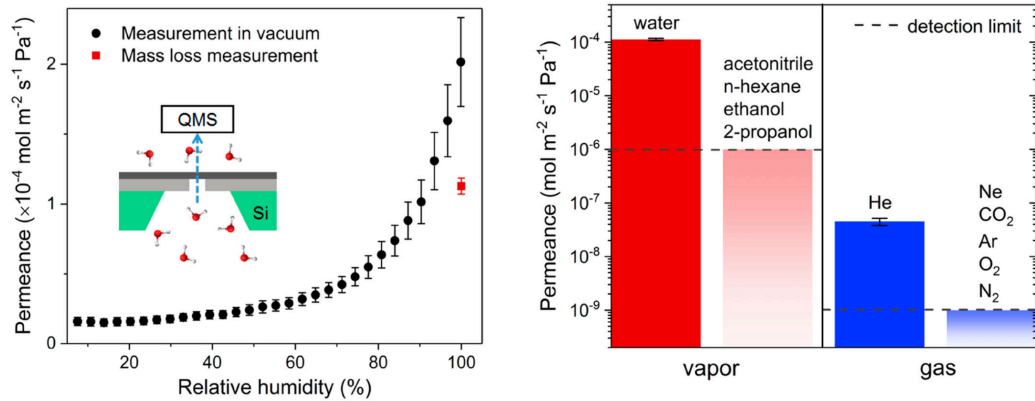
(a) Water permeance of a TPT-CNM, taken from Ref. [17].

(b) Permeances for a variety of gases, taken from Ref. [17].

Figure 5.14.: Water permeance of a TPT-CNM measured in vacuum or by mass-loss in a) and permeances for a variety of gases in b).

One of the most promising features of CNMs for commercial use lies in their property of water filtration overcoming the limitations of conventional filtration membranes with regard to the trade-off between permeance and selectivity [17]. Sub-nanometer channels or pores, as potentially revealed by atomic force microscopy discussed in Ch. 5.4 and estimated to be less than 0.7 nm wide, unite high water selectivity and high water permeance as measured by the mass-loss method of around $1.1 \cdot 10^{-1} \mathrm{mol} \cdot \mathrm{m}^{-2} \cdot \mathrm{s}^{-1} \mathrm{Pa}^{-1}$, significantly higher than existing membrane filtration methods [17]. The measured permeance would correspond to around 66 water molecules $\cdot \mathrm{s}^{-1} \cdot \mathrm{Pa}^{-1}$ per pore [17]. This would furthermore lead to the estimate of around one pore per nm^2. Thus, with the estimated pore size of at least 0.5 nm in diameter, the membrane is indeed overwhelmingly porous. For that, the initial material of the SAM has to be displaced for holes to form which is possible due to the SAM structure not being the closest packing [123]. Existence of residual stress σ_0 in the membrane is believed to be another key indicator for hole formation [84].

Helium (He) on the other hand has an almost 2500 times lower flux than water vapor. Gases like neon (Ne), oxygen (O_2), argon (Ar) and carbondioxide (CO_2) permeances being below the detection limit [17] as depicted in Fig. 5.14b indicate that CNMs are indeed molecular sieves. However, when taking into account that the kinetic diameter of helium of 0.26 nm is actually smaller than the kinetic diameter of water with 0.265 nm while helium has a permeability 2500 times worse than water, there must be another mechanism. All other tested and non-permeating gases have a kinetic diameter above 0.275 nm indicating that the estimated pore size might be too big [17].
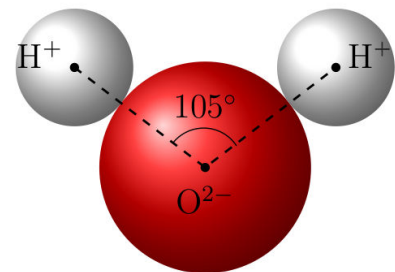
Figure 5.15.: Electric dipole moment of a H_2O molecule.

The first explanation lies in the molecular density of water which is 10^4 times higher than of helium, thus there is a higher probability to reach the membrane [17]. Another explanation can be found by comparison with other highly permeable structures such as aquaporines in biological systems, graphene with holes or graphene with embedded carbon nanotubes [17]. All of these show a transport mechanism called single-file mode, which can be broken down into three steps: adsorption on the surface and diffusion to the channel, transport across the channel and dissociation from the channel and surface [17]. The transport across the channel is initiated by one water molecule entering the channel and pulling in other molecules through electric dipole moments as depicted in Fig. 5.15 for water.

This transport mode is supported by measurements with the mass-loss method as depicted in the inset graphic in Fig. 5.14a, the measurement result of which is shown as the red datapoint in the same figure. For this measurement, a cup was filled with a pre-defined volume of water and placed in a low-humidity environment [17]. Difference in water flux between a sealed cup, a cup with a tiny hole in the top and a cup with a CNM on top is measured. For the latter case, no difference was observed for an upright and an inverted cup, thus underlining the possibility of single-file mode transport [17]. Additionally, permeances have been verified by measurements in vacuum, where one side of a CNM is exposed to water vapor under controlled relative humidity and flow being detected by a mass spectrometer on the other side [17] as depicted by the black data points in Fig. 5.14a.

A molecular dynamics simulation of water permeation through a CNM is presented in Ch. 10 using the explicit solvent model TIP3P.

6. Molecular dynamics modeling of CNMs and mechanical properties

Parts of this chapter are an extension of the previous work done on carbon nanomembranes by Florian Gayk as presented in his Master's thesis [3] from 2018. It has been expanded by new methods to calculate the Young's modulus with a dynamical stress-strain and a barostated approach as well as simulated nanoindentation as opposed to the LAMMPS-internal ELASTIC script that has been adopted to work with carbon nanomembranes. Young's moduli have been calculated for the structures generated for the Master's thesis to extend the existing database of simulated membranes. This chapter reproduces this work as published in Ref. [1] either closely following or verbatim.

6.1. Modeling the electron-induced cross-linking of SAMs
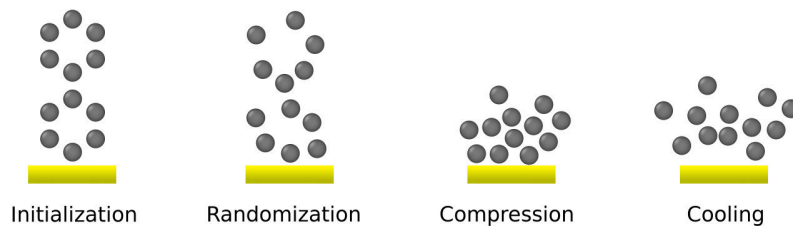
Figure 6.1.: Sketch of the theoretical synthesis model of a CNM starting from a BPT precursor.

Modeling of a membrane is achieved through the following steps inspired by the experimental procedure as depicted in Fig. 6.1 and explained in detail in Ch. 4. The simulations include only carbon atoms, which is justified by the fact that the final CNM consists of pure carbon only. All other atoms such as the surface terminating thiols are neglected right from the beginning:

1. Formation of a self-assembled monolayer (SAM) from a selection of various precursor molecules on a gold substrate is initiated by placing carbon atoms above a gold surface at positions they would have in the respective precursor molecules (Initialization). Then, specific starting conditions are imposed by tilting or randomly moving some or all molecules and by either removing some of the atoms or whole molecules to e.g. mimic defects in the experimental process (Randomization), see also Tab. 5.1. Also, the computationally expensive array of gold

atoms representing the substrate is replaced by a repulsive Lennard-Jones wall potential

$$V(r) = 4\varepsilon \left[\left(\frac{\sigma}{r} \right)^{12} - \left(\frac{\sigma}{r} \right)^{6} \right], \tag{6.1}$$

with its minimum $r_{\mathrm{min}} = \sqrt[6]{2} \cdot \sigma$ at the bottom of the simulation box z_{lo} and parameters for the C-Au interaction $\varepsilon_{\mathrm{C\text{-}Au}} \approx 0.29256$ kcal/mol ≈ 0.012695 eV and $\sigma_{\mathrm{C\text{-}Au}} \approx 2.99$ Å taken from Ref. [124]. It should be mentioned however that this also leaves the precursor molecules with no structure of the substrate (except for the structural parameters of gold taken for the initial placement of precursor molecules), which might have some influence, e.g. the experimentally observed residual stress σ_0 assumed to play a role in hole formation [84], on the formation process during the next fabrication step.

2. Experimentally, after low-energy electron irradiation of the SAM, cross-linking of the molecules induces the formation of the CNM. Theoretically, the electron irradiation is modeled by a vertical force gradient being applied to the atoms that is linear and decreasing with height (Compression). It is assumed that secondary electrons actually cause most of the bond-breaking and cross-linking [125]. The effect of secondary electrons is e.g. modeled by lateral forces on specific molecules.

3. The now highly excited model system is then allowed to relax towards it equilibrium structure according to a thermostat dynamics (Nosé-Hoover or Langevin) with a desired decrease in temperature (Cooling).

Taking into account the XPS measurements presented in Table 5.1 taken from Ref. [11], one has a qualitative measure for the modeled membranes. The thickness of the membrane should remain close to the thickness of the original SAM, since there is only little loss of carbon during irradiation [11].

The outcomes of the simulation procedure will be presented in Ch. 6.5 divided into three categories depending on the model scenarios: 1) randomization and compression, i.e. after randomization of atom coordinates a vertical force is applied, 2) randomization, compression and lateral force that acts on some selected molecules and 3) randomly removed molecules.

6.2. Measure of elasticity: The Young's modulus

With the structures generated, the Young's modulus is chosen as the observable of choice as it allows comparison with experimental results due to the lack of electronic properties within classical molecular dynamics. These calculations are realised in four ways:

1. An adaption of LAMMPS' own ELASTIC code as available in the example repository [126] to the specific needs of modeled CNMs which derives the Young's modulus from the curvature of the potential Energy U. For this, the implementation of the EDIP by Marks is used.

2. A dynamical approach that stretches the membrane (stress vs. strain), thereby allowing for deformation and defect formation. The modulus is derived from the linear region of the stress-strain curve. Due to the lack of the virial per atom in the implementation of the EDIP, the AIREBO potential is used for this type of simulation as it includes the necessary virial term and performs overall well. The technical details of the stress-strain method are explained in Ch. 6.3.

3. A barostated approach where the membrane is pressurized in all but one direction and then deforms under the pressure. The resulting stress-strain response can be analyzed analogously to the dynamical stretch approach. The process is outlined in Ch. 6.8 as an outlook to different methods of calculating the Young's modulus.

4. Simulated nanoindentation with a spherical indenter explained in detail in Ch. 7.

The Young's modulus E in the ground state, i.e. at temperature $T = 0$ K, can be evaluated from the curvature of U at the ground state configuration (the kinetic energy is zero) [93]:

$$E_V = \frac{1}{V_0} \left(\frac{\partial^2 U}{\partial \alpha^2} \right)_{\alpha=1} , \qquad (6.2)$$

where α is the factor by which all positions are scaled along the direction of the dimensionless unit vector $\vec{e}_\alpha$, i.e.

$$\vec{x}_i \to \vec{x}_i + (\alpha - 1)\, \vec{e}_\alpha \cdot \vec{x}_i\, \vec{e}_\alpha . \qquad (6.3)$$

V_0 denotes the cuboid volume of the sample in equilibrium.

Another approach is to derive the Young's modulus from the relationship between stress σ and strain ε in the linear part of a stress-strain-curve as employed by materials science for macroscopic materials, i.e. by determining

$$E = \frac{\Delta\sigma}{\Delta\varepsilon} , \qquad (6.4)$$

which can be done in classical molecular dynamics by moving clamped parts of the material similar to experiments for material characterization. This is not directly transferable to CNMs from the experimental point of view as they cannot be investigated this way due to their restricting size. Alternatively, the Young's modulus can be theoretically determined by using one of the other linear elasticity methods, i.e. the barostat method or nanoindentation.

An alternative experimental way to characterize such thin membranes is by performing a bulge test [14] where the deflection of a membrane under pressure is measured by the tip of an atomic force microscope as previously described in detail in Ch. 5.9. Bulge testing has been modeled as a molecular dynamics simulation for graphene in Ref. [121]. This method however is not applicable to carbon nanomembranes since there is no well defined profile of curvature of the membrane while for graphene there is a formula for expressing maximum height of the graphene sheet with regard to the applied pressure difference [121]. Also, one might have to resort to bigger molecules for the gas pressurizing the membrane (for graphene hydrogen is used) when this model is transferred to CNMs as the holes possibly allow for gas molecules to pass through the membrane, making it hard to keep track of applied pressure when there is a vacuum on the other side.

6.3. Modeling of the stress-strain method

(a) Schematic representation of clamp regions (black) and enlarged simulation box (gray).

(b) Result of straining in the direction as depicted by the schematic drawing with color-coding for the corresponding stress-tensor component.
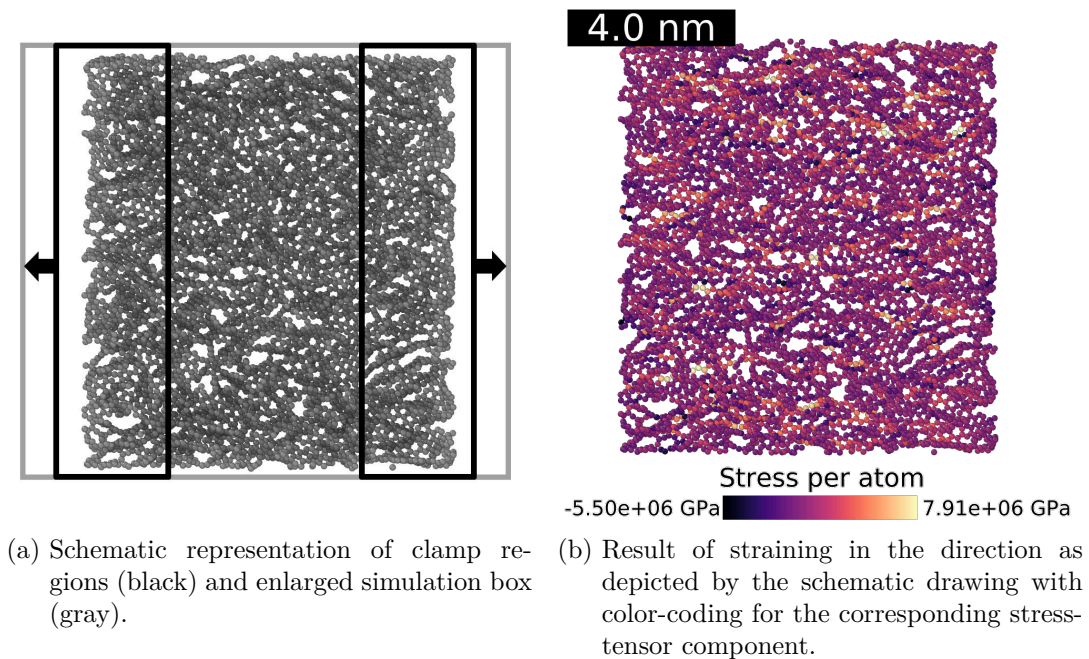
Figure 6.2.: Stress-strain simulation setup and exemplary result with qualitative color coding.

The stress-strain variant of Young's modulus determination is inspired by the same type of macroscopic experiments in materials science, where the material under test is clamped on two opposing sides and strained by a factor ε given a specific strain-rate. The stress response σ depends on material properties such as the Young's modulus E for the linear region of straining. For that region, the stresses in the material are given by a law similar to Hooke's law, i.e. $\sigma = E \cdot \varepsilon$ where ε is the strain $\frac{L-L_0}{L_0}$ with L the current length and L_0 the initial length. This way, the Young's modulus can be determined by fitting the data with a linear function.

In order to simulate stress-strain responses in molecular dynamics, clamping of the material has to be modeled. The method presented in Ref. [127] has been adapted for this procedure by making use of selection box regions (*region* command in LAMMPS) of the size of the clamp as depicted by the black outline in Fig. 6.2a. As these regions have to move to strain the material, the simulation box with fixed boundary conditions (gray lines in Fig. 6.2a) is enlarged in the direction of strain to leave room for the clamps. Atoms in the clamp region are excluded from the calculation of stresses inside the material and considered rigid (*fix setforce 0 0 0*). Exclusion of the clamps' atoms is done by putting the clamp atoms and all other atoms each in their own group. The initial simulation box side length of the strain direction is saved for the calculation of strain at each timestep. Finally, clamps are moved outwards (depicted by the black arrows in Fig. 6.2a) using the *change_box* command with a predefined strain-rate equal and fixed for every deformation step.

The rate has to be chosen such that the dynamics stay physical, i.e. atoms should not move further apart from each other than what is covered by the effective potential, i.e.

pulling them over a certain energy barrier, while avoiding unnecessarily long simulations times.

For atoms to change their position, the *fix remap* command is necessary when changing the clamp box position. Moving of the clamps is done inside a deformation loop until the desired number of straining steps is reached. Logging the current strain and corresponding stress tensor component allows to record the necessary stress-strain data, which can then be fitted e.g. using gnuplot [128].

To shorten the simulation runtimes, straining is always limited to about 1 % size increase which should be plenty for the linear region to deliver meaningful data as thoroughly tested with longer simulation runs. For the simulations in this chapter, the AIREBO potential was used with Lennard-Jones and torsion terms enabled and a cutoff of 3 Å.

An exemplary result of straining in x-direction (along the arrows depicted in the schematic Fig. 6.2a) of a TPT membrane with a total of 7200 atoms, i.e. 400 TPT precursor molecules and lateral size of around 87.3 Å in x- and 98.5 Å in y-direction is shown in Fig. 6.3. Here, the initial stress σ is not zero due to residual stresses in the material, which however does not affect the calculation of the Young's modulus as defined by the derivative of the linear region. The linear fit of said region results in a Young's modulus of around 87 GPa for this particular membrane generated with vertical momentum transfer only, not adjusted for the volume as described in the next chapter. The ELASTIC method would suggest 352 GPa and 131 GPa by the barostat method that will be introduced in Ch. 6.8.
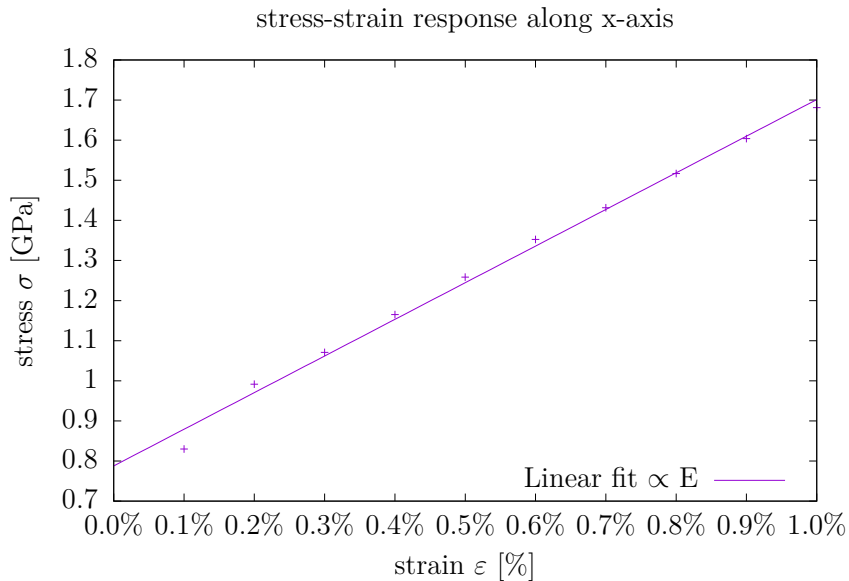
Figure 6.3.: Fit of the linear region of stress-strain data for a TPT-CNM.

It is also possible to output the stress data on a per-atom basis for visualization purposes, i.e. color-coding the stress distribution and intensity as shown in Fig. 6.2b for the previously discussed membrane. This representation of the data allows for qualitative statements to be made. For example, the regions of higher stress as depicted by the brightest colors seem to be of linear chain-like nature along the strain direction thus indicating that sp_1 bonding together with the cross-linking could play an

important role in what gives the membrane its strength but drastically lower Young's modulus than that of graphene.

The implementation of the stress-strain method in LAMMPS relies on the *compute stress/atom* command, i.e. the stress per atom which in turn is calculated from the virial per atom [129]. As the virial per atom is not implemented in the version of the EDIP used for this thesis, AIREBO is used for all simulations that need this LAMMPS *compute* style.

6.4. Volume ambiguity

Due to the irregular internal structure of a CNM it is difficult to define the proper volume of the membrane. Thus one has to find ways to approximate the volume, which introduces inherent uncertainty into the results, since the variation of thickness can be of the same order as the thickness itself depending on how pronounced the surface roughness and voids in the membrane are. There are several options to calculate the volume. The simplest and crudest is to take the size of the simulation box, which does not account for voids at all. Another more involved method is to create a surface volume of the CNM that tries to minimize superficial empty volumes thus creating a shrinkwrap-like representation of the membrane's volume. Due to the approximate nature of the surfacing algorithm, the resulting volume is over- and underestimated as can be seen in Fig. 6.4a which is the source of the relatively huge error mentioned earlier.

The shrinkwrapped volume is constructed using the software Ovito [130] and its "Construct surface mesh" modifier. The differences between the two methods can be best observed when comparing the gray shrinkwrap volume to the black outlines of the cuboid simulation box in Fig. 6.4b. To adjust the calculated Young's moduli with respect to the volume of the system, post-processing has to be performed to scale them appropriately.
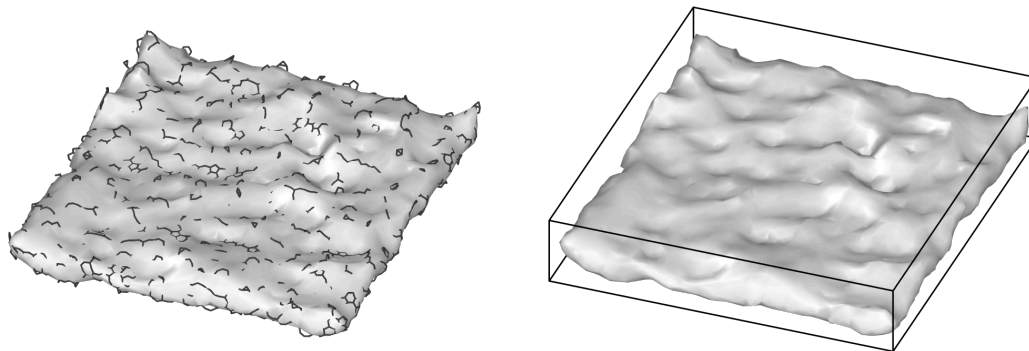
(a) Surface volume reconstruction for $r = 4$ Å with C-C bonds shown to underline over- and underestimation of the shrinkwrapped volume.

(b) Typical approximate shrinkwrapped volume representation without atoms or bonds compared to the simulation box.

Figure 6.4.: Comparison of uncertainty introduced by surface volume reconstruction error and difference between surface and simulation box volume.

6.5. Vertical momentum dynamics

(a) Top view to emphasize porosity.   (b) Perspective overview of the whole membrane.
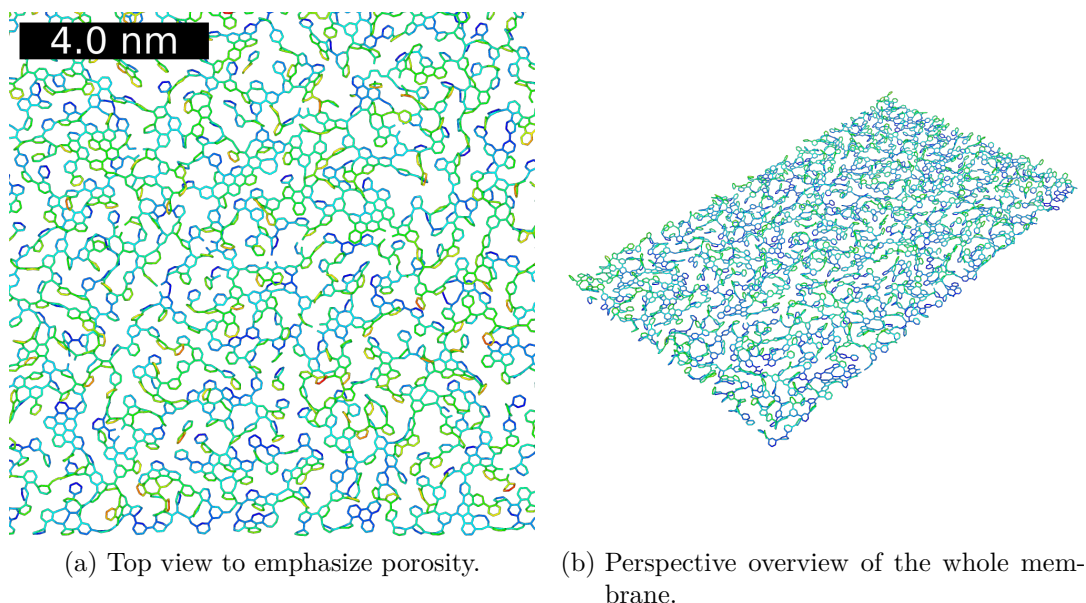
Figure 6.5.: A typical result of vertical momentum dynamics applied to a BPT-SAM, $T = 700$ K, $k = 60$ $\frac{\text{eV}}{\text{Å}}$.

This approach tries to be realistic in that a vertical momentum is applied to the molecules of the self-assembled monolayer in direction of the gold substrate to simulate the momentum transfer of electrons to the atoms. Since most of the electrons' energy should be absorbed at the top of molecules, a linear profile for the applied force is used utilizing the LAMMPS *fix addforce* command, i.e. $F = -k \cdot (z - z_{\text{lo}})$, where z_{lo} is the z-coordinate of the gold surface. During the time evolution of this procedure, atoms will be compressed towards and reflected away from the substrate. Time evolution is stopped when the height of the membrane approaches the initial monolayer height as experimentally observed membrane heights are also close to the self-assembled monolayer [11]. Finally, the system is cooled using thermostat dynamics. Multiple proportionality factors k are tested for the force profile ranging from 30 $\frac{\text{eV}}{\text{Å}}$ to 200 $\frac{\text{eV}}{\text{Å}}$ (z and z_{lo} being dimensionless), which is equivalent to a velocity range of 2.41 $\frac{\text{Å}}{\text{ps}}$ to 16.07 $\frac{\text{Å}}{\text{ps}}$. Additionally, an isotropic randomization corresponding to a temperature of $300 \ldots 1100$ K is applied to introduce some areas where bond formation might be preferred.

Visualizations of membranes created through this process can be seen in Fig. 6.5 to Fig. 6.7. The resulting carbon networks show pronounced irregular areas and contain remnants of broken aromatic rings that serve as linkers in the network as well as large flakes of graphene-like substructures.
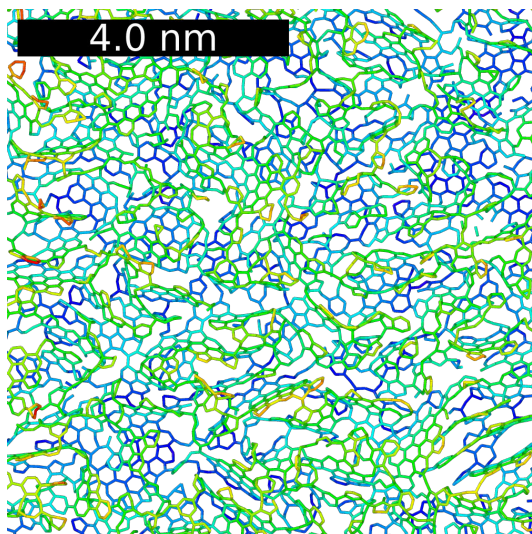
(a) Top view to emphasize porosity.
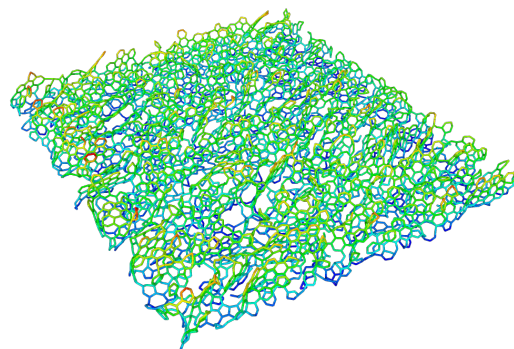
(b) Perspective overview of the whole membrane.

Figure 6.6.: A typical result of vertical momentum dynamics applied to a TPT-SAM, $T = 700$ K, $k = 30 \frac{\text{eV}}{\text{Å}}$.
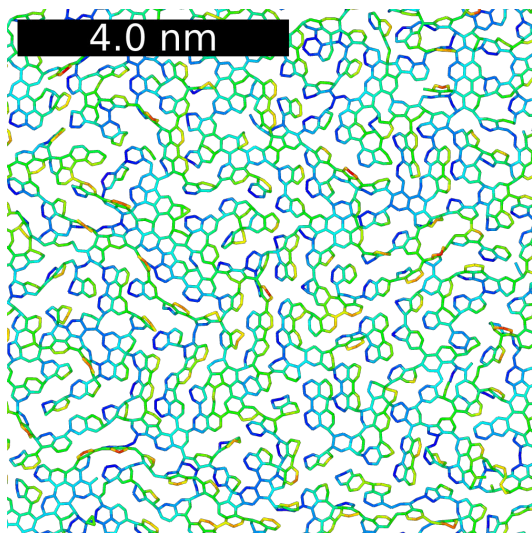
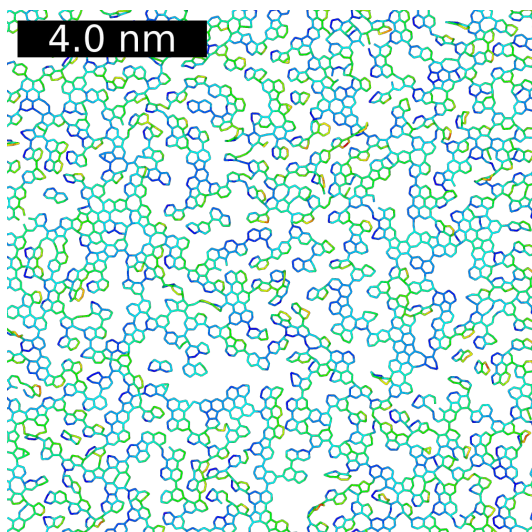(a) Top view to emphasize porosity.
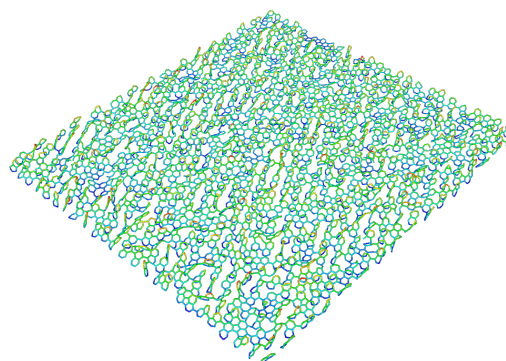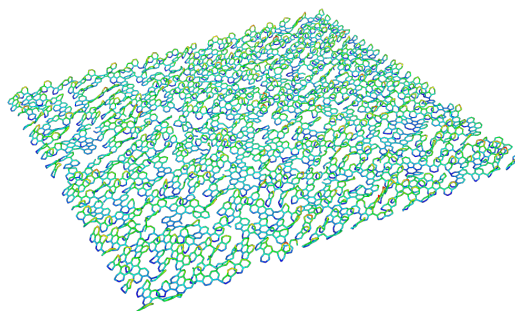
(b) Perspective overview of the whole membrane.

Figure 6.7.: A typical result of vertical momentum dynamics applied to a NPTH-SAM, $T = 700$ K, $k = 30 \frac{\text{eV}}{\text{Å}}$.

The generated CNMs, which are mechanically stable, are characterized by rather large Young's moduli as presented in Tab. 6.1. In particular, NPTH precursors form rather flat and rigid membranes with moduli close to that of graphene. All Young's moduli presented in the following chapters that are calculated with the stress-strain method have been fitted using gnuplot, but graphs will not be shown for the sake of clarity. Young's moduli obtained using the stress-strain method are systematically smaller than those calculated with the ELASTIC method by a factor of 3 to 4, see Tab. 6.2. The Young's modulus of the BPT membrane is even more than ten times smaller, which could be related to dynamic stretching of the low cross-linked BPT membrane in comparison with TPT and NPTH.

Table 6.1.: Method 1 (EDIP and curvature): Young's moduli in x- and y-direction (adjusted to volume of simulation box | surface volume).

	$E_{x,1}$/GPa	$E_{y,1}$/GPa
TPT (T=700 K, $k = 30\ \frac{eV}{\text{Å}}$)	436 | 847	334 | 649
TPT (T=700 K, $k = 200\ \frac{eV}{\text{Å}}$)	215 | 448	220 | 457
TPT (T=300 K, $k = 60\ \frac{eV}{\text{Å}}$)	325 | 987	316 | 960
TPT (T=1100 K, $k = 60\ \frac{eV}{\text{Å}}$)	351 | 866	339 | 838
BPT (T=700 K, $k = 60\ \frac{eV}{\text{Å}}$)	202 | 736	191 | 695
NPTH (T=700 K, $k = 60\ \frac{eV}{\text{Å}}$)	536 | 1367	500 | 1277

Table 6.2.: Method 2 (AIREBO and stress): Young's moduli in x- and y-direction (adjusted to volume of simulation box | surface volume).

	$E_{x,2}$/GPa	$E_{y,2}$/GPa
TPT (T=700 K, $k = 30\ \frac{eV}{\text{Å}}$)	135 | 262	77 | 150
TPT (T=700 K, $k = 200\ \frac{eV}{\text{Å}}$)	45 | 92	40 | 83
TPT (T=300 K, $k = 60\ \frac{eV}{\text{Å}}$)	122 | 371	97 | 295
TPT (T=1100 K, $k = 60\ \frac{eV}{\text{Å}}$)	123 | 303	100 | 247
BPT (T=700 K, $k = 60\ \frac{eV}{\text{Å}}$)	16 | 58	19 | 69
NPTH (T=700 K, $k = 60\ \frac{eV}{\text{Å}}$)	99 | 252	45 | 115

6.6. Additional lateral momenta

(a) Top view to emphasize porosity.

(b) Perspective overview of the whole membrane.
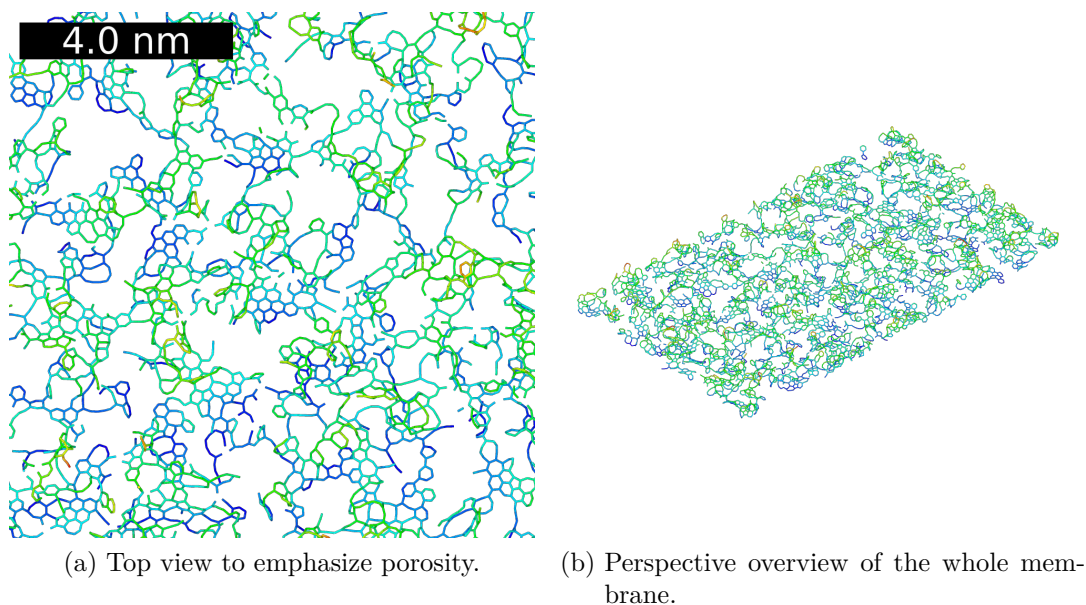
Figure 6.8.: A typical result of vertical and lateral momentum dynamics applied to a BPT-SAM after 4900 timesteps, $T = 300$ K, $v = 35 \frac{\text{Å}}{\text{ps}}$, $k = 60 \frac{\text{eV}}{\text{Å}}$.

In order to mimic the influence of secondary electrons and their interaction with neighboring molecules and atoms, additional lateral momenta of various magnitude as shown in Tabs. 6.3 and 6.4 are incorporated. An isotropic but randomly chosen lateral force is applied to all atoms using the same LAMMPS *fix addforce* command as before. Tabs. 6.3 and 6.4 show averages over 10 realizations of such membranes depending on the theoretical synthesis procedure. By applying lateral momenta there is a higher chance for holes to form due to displacement in the x- and y-directions. This also affects membrane thickness and surface roughness. This method relies highly on the randomly chosen lateral force by which molecules are laterally displaced. Realistically, forces would not be isotropic throughout the membrane. Thus, the Young's modulus is averaged over ten different configurations each. Large holes start to emerge for the BPT based and NPTH based CNMs in Figs. 6.8 and 6.10, respectively.

For the TPT based membrane depicted in Fig. 6.9, holes are not as pronounced, but there is increased surface roughness compared to the previous results.

(a) Top view to emphasize porosity.

(b) Perspective overview of the whole membrane.
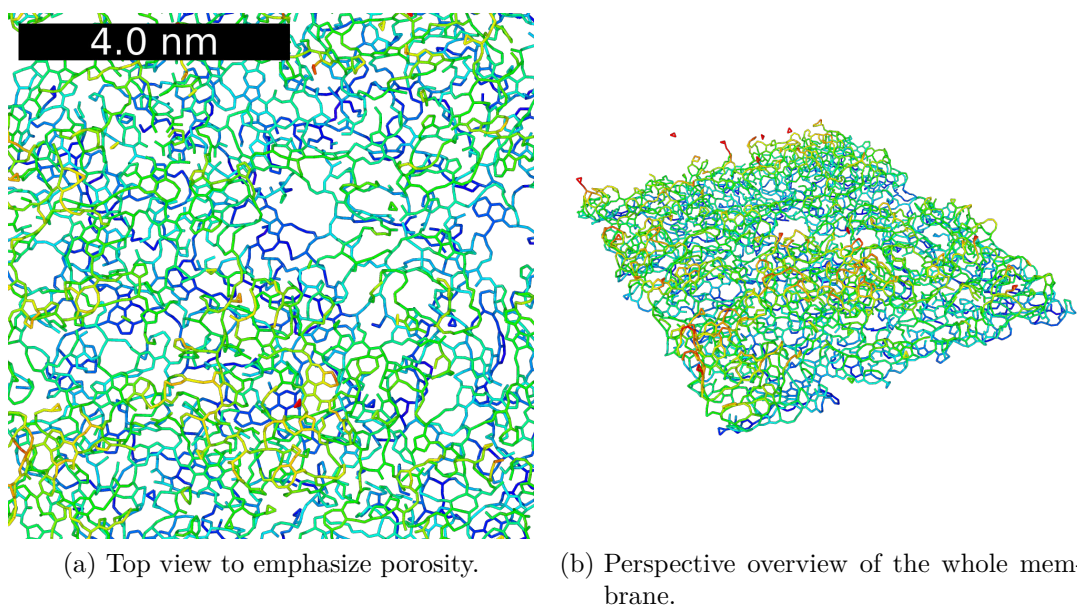
Figure 6.9.: A typical result of vertical and lateral momentum dynamics applied to a TPT-SAM after 5700 timesteps, $T = 700$ K, $v = 35$ $\frac{\text{Å}}{\text{ps}}$, $k = 60$ $\frac{\text{eV}}{\text{Å}}$.

(a) Top view to emphasize porosity.

(b) Perspective overview of the whole membrane.
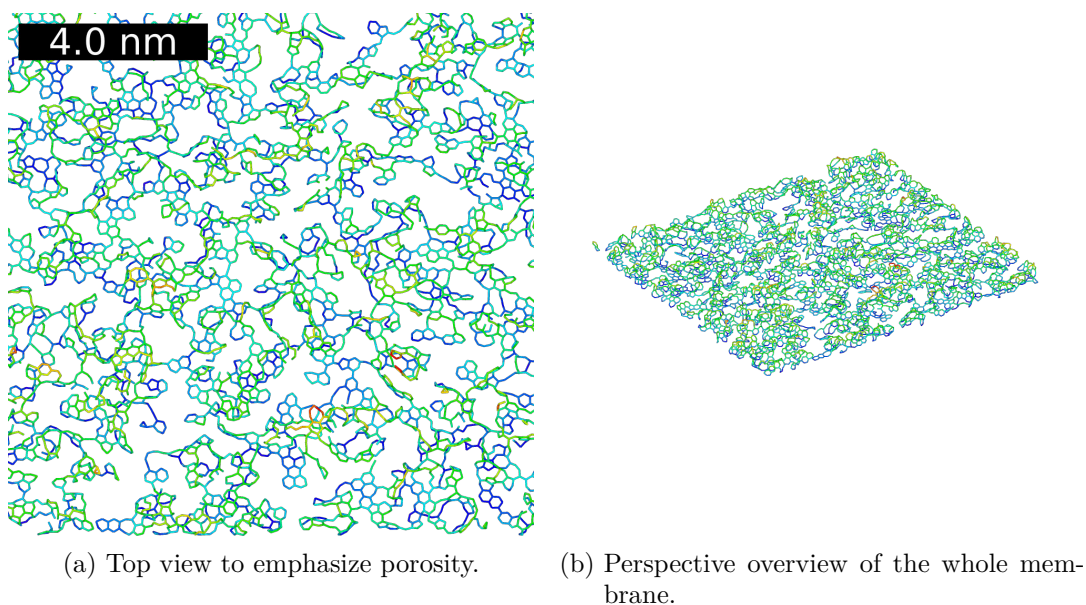
Figure 6.10.: A typical result of vertical and lateral momentum dynamics applied to a NPTH-SAM after 2500 timesteps, $T = 300$ K, $v = 35$ $\frac{\text{Å}}{\text{ps}}$, $k = 60$ $\frac{\text{eV}}{\text{Å}}$.

The qualitative results are also reflected in the quantitative results for the Young's modulus. With increasing magnitude of the lateral force there is a decrease in the Young's modulus for all precursor molecules. Only for the highest $v = 35\ \frac{\text{Å}}{\text{ps}}$, the TPT based nanomembrane's Young's modulus increases, which could be explained by the height of the precursor molecule. While BPT and NPTH are basically two carbon rings tall, TPT is about 50 % taller. This gives rise to the possibility of bonds to form on top of the membrane allowing increased surface roughness and more dense linking thereby increasing the Young's modulus.

Table 6.3.: Method 1 (EDIP and curvature): Young's moduli in x-direction (adjusted to volume of simulation box | surface volume).

$v / \frac{\text{Å}}{\text{ps}}$	TPT: $E_{x,1}$/GPa	BPT: $E_{x,1}$/GPa	NPTH: $E_{x,1}$/GPa
5	338(55) | 925(18)	246(14) | 782(12)	588(41) | 2002(47)
15	299(20) | 858(24)	195(25) | 888(15)	546(32) | 1865(38)
25	224(46) | 769(20)	166(16) | 818(24)	497(25) | 1579(49)
35	268(46) | 738(32)	139(12) | 732(12)	410(34) | 1393(40)

Table 6.4.: Method 2 (AIREBO and stress): Young's moduli in x-direction (adjusted to volume of simulation box | surface volume).

$v / \frac{\text{Å}}{\text{ps}}$	TPT: $E_{x,2}$/GPa	BPT: $E_{x,2}$/GPa	NPTH: $E_{x,2}$/GPa
5	120(23) | 328(63)	25(4) | 79(13)	201(32) | 684(109)
15	98(12) | 281(34)	23(5) | 105(23)	144(28) | 492(96)
25	62(14) | 213(48)	19(4) | 94(20)	114(34) | 362(108)
35	68(11) | 187(30)	16(3) | 84(16)	95(23) | 323(78)

6.7. Missing molecules

(a) Top view to emphasize porosity.

(b) Perspective overview of the whole membrane.
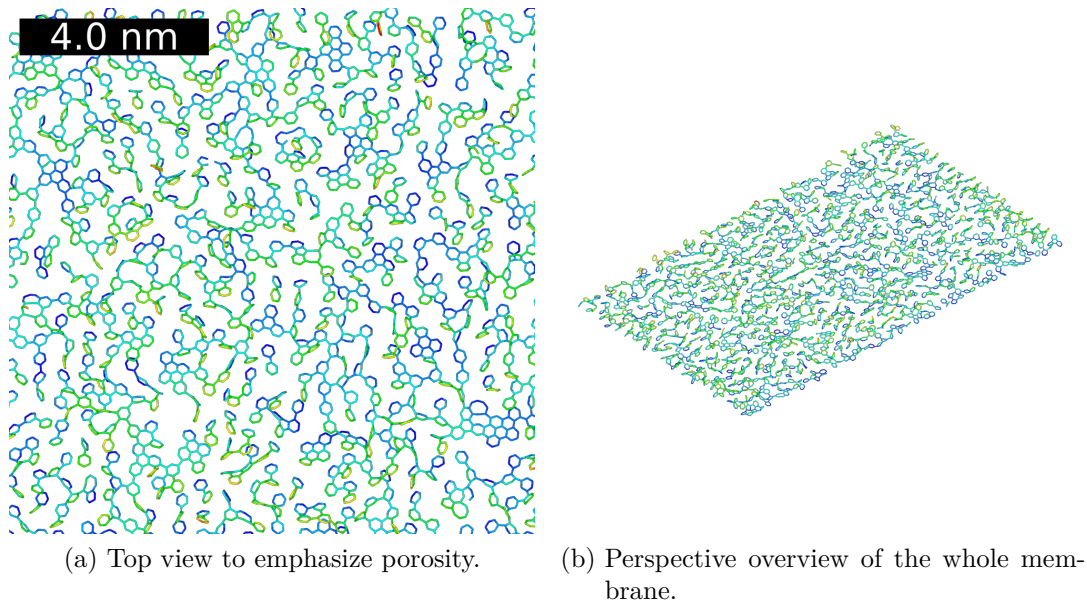
Figure 6.11.: A typical result of vertical dynamics with 10 % missing molecules applied to a BPT-SAM after 4900 timesteps, $T = 300$ K, $k = 60 \frac{eV}{Å}$.

By randomly removing molecules from the self-assembled monolayer, the formation of holes in the resulting membrane can be enhanced. It is experimentally verified that about 5 to 9 % of carbon atoms get lost during synthesis [11]. The molecular dynamics procedure models a correlated/collective disappearance of atoms in form of a whole molecule where percentages of removal range from 5 to 20 %. Areas where molecules are missing are preferred locations of holes as applied vertical momentum can only cover the gaps to a limited degree. This also gives rise to the possibility of further lowering the Young's modulus. The resulting CNMs show a less dense structure than before. Holes have the tendency to be smaller but more frequent due to the more isotropic distribution of missing molecules, which can be seen in Figs. 6.11 to 6.13.
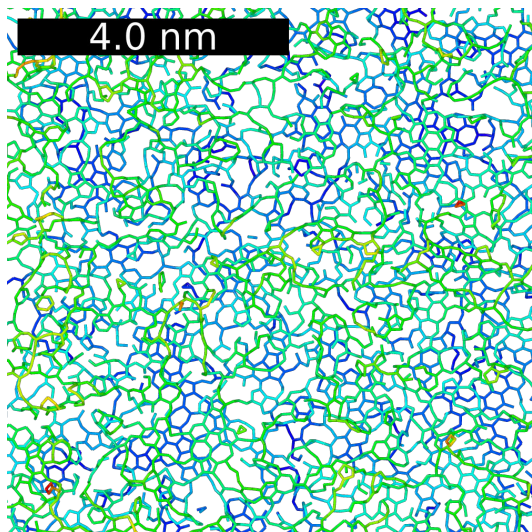
(a) Top view to emphasize porosity.
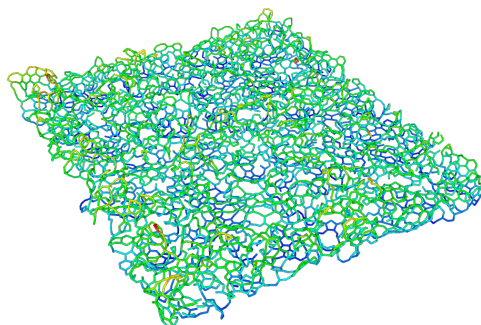
(b) Perspective overview of the whole membrane.

Figure 6.12.: A typical result of vertical momentum dynamics with 5 % missing molecules applied to a TPT-SAM after 7200 timesteps, $T = 300$ K, $k = 60 \, \frac{\text{eV}}{\text{Å}}$.

(a) Top view to emphasize porosity.

(b) Perspective overview of the whole membrane.

Figure 6.13.: A typical result of vertical momentum dynamics with 20 % missing molecules applied to a NPTH-SAM after 2500 timesteps, $T = 300$ K, $k = 60 \, \frac{\text{eV}}{\text{Å}}$.

When it comes to quantitative results, the differences in Young's moduli are not as pronounced as the visual differences. The moduli vary by 10 to 20 % at most. Even if there is significant carbon loss when irradiating the SAM, the newly created bonds are too isotropic to allow for weaker areas. Thus any local weak spot is corrected by molecules arranging flatter than before. This is best observed for the NPTH based carbon nanomembrane shown in Fig. 6.13, where large areas of intact hexagonal carbon rings strengthening the overall membrane can be seen.

Table 6.5.: Method 1: Young's moduli in x-direction for different deletion percentages (adjusted to volume of simulation box | surface volume).

p / %	TPT: $E_{x,1}$/GPa	BPT: $E_{x,1}$/GPa	NPTH: $E_{x,1}$/GPa
5	368 | 1011	220 | 704	620 | 2313
10	255 | 976	177 | 787	579 | 1689
20	329 | 1000	193 | 824	558 | 2437

Table 6.6.: Method 2: Young's moduli in x-direction for different deletion percentages (adjusted to volume of simulation box | surface volume).

p / %	TPT: $E_{x,2}$/GPa	BPT: $E_{x,2}$/GPa	NPTH: $E_{x,2}$/GPa
5	131 | 360	21 | 67	135 | 503
10	86 | 329	16 | 71	50 | 146
20	105 | 319	16 | 68	40 | 175

6.8. Barostated dynamics

Another linear elasticity approach to determine the Young's modulus by molecular dynamics means is the simultaneous application of simulation box deformation and barostating as suggested in Refs. [131, 132]. The Young's modulus can then be derived analogously to the stress-strain method discussed in Ch. 6.3. The difference to the latter method lies in how the membrane is deformed. For the simulation in this chapter, the AIREBO potential was used with Lennard-Jones and torsion terms enabled and a cutoff of 3 Å.

Instead of clamping opposing sides to strain along the e.g. x-axis of the membrane,

(a) TPT-CNM before barostat straining.   (b) TPT-CNM after 10% strain.
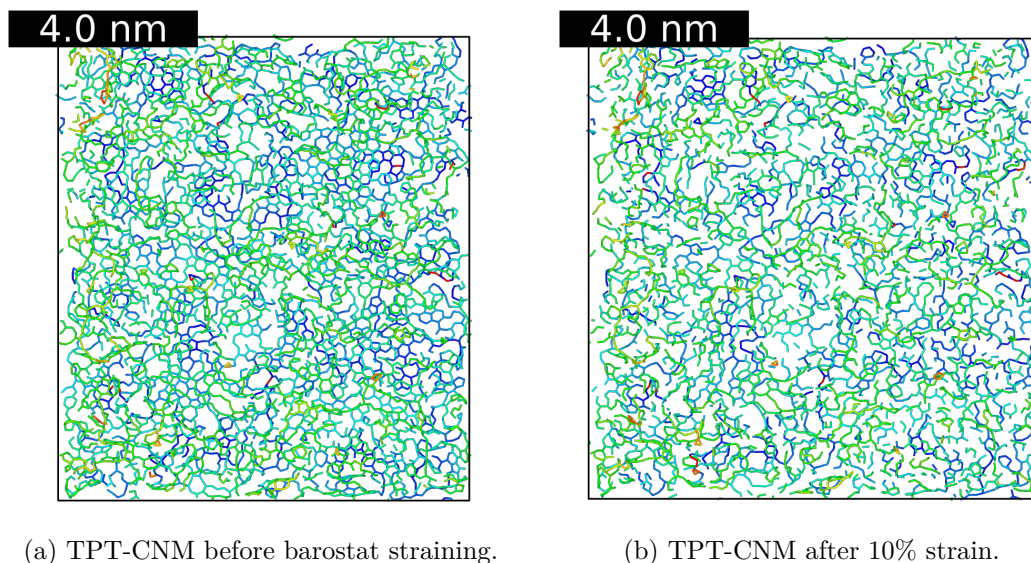
Figure 6.14.: Visualization of the structural changes inside a TPT-CNM during barostated straining. Strain direction is along the horizontal axis.

the simulation box length in that direction is enlarged at a specified strain rate without remapping of the atoms, i.e. the simulation box is enlarged in the chosen direction with no influence on the atom positions. The system is initialized with a thermo- and barostat which are of Nosé-Hoover type using the *fix npt* command [49], that keeps the pressure in all directions but the strained one (i.e. y- and z-direction in the example given) at a constant 1 bar. Temperature is held low at 100 K to avoid thermal fluctuations.

If the strained side length L changes by ΔL, there is a corresponding change in volume $\Delta V = V \cdot (1 + \Delta L/L)$ that would lead to a decrease in pressure since the number of particles N and temperature T are kept constant. This change in pressure is compensated by the barostat in the unstrained directions, through scaling the atom positions, essentially pushing atoms to fill the newly created volume, which is also changed in y- and z-direction. An exemplary bond visualization of a TPT-CNM of 7200 atoms and size 87.6 Å x 98.6 Å x 11.6 Å is given in Fig. 6.14a for the unstrained initial membrane and after 10 % strain in Fig. 6.14b. It should be noted that a strain of 10 % is unnecessarily huge and unrealistic, but serves the purpose of better visualization. Fig. 6.15 shows one of the sides along which the box is deformed (i.e. normal to the face as outlined by the black line) in its initial size (top) and after 10 % strain (bot-
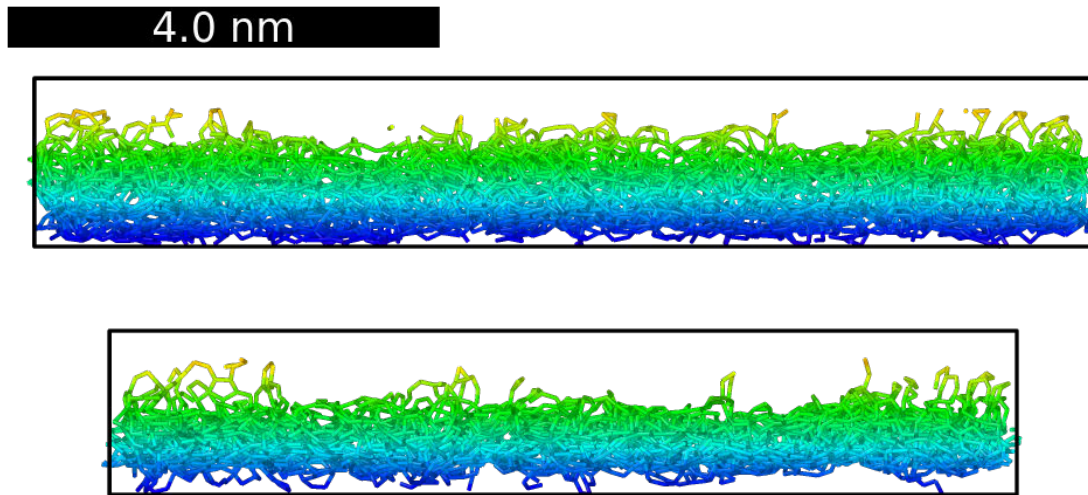
Figure 6.15.: Side view normal to the strained simulation box face. Top: Initial TPT-CNM dimensions, bottom: TPT-CNM dimensions after 10 % strain.

tom). Both images have been taken from the same point of view. Thus it becomes clear that the barostat changed the membrane thickness by squeezing it in z-direction (vertical axis) and that the lateral dimension in y-direction (along the horizontal axis) decreased in an effort to keep pressure constant.

Straining and barostating is repeated until the desired strain ϵ is reached. The resulting deformation of the membrane causes stresses σ similar to the stress-strain method, the evaluation of which is equivalent by fitting the linear part with a function proportional to the Young's modulus E. One criterion of the simulation's quality is that the stress components in unstrained directions should be close to unaffected when the barostat adjusts the pressure and side lengths. However, as shown in Fig. 6.16 this is not the case for small strain percentages, but holds in the limit of huge strain. The membrane of which the stress-strain data has been obtained from, has been strained to more than double its initial size to emphasize that the membrane appears to be mechanically stable even above a size increase of 30 % with a steep decrease in stress σ afterwards. This decrease however is related to the mechanical destruction of the membrane that should take the stress down to zero, but long-range forces as included in the AIREBO potential make it appear intact when it would realistically be not. The strain-rate is again chosen such that the simulation stays within physical regions, but larger than the rate of the stress-strain approach. This is to keep the barostat from pushing the system back into its initial configuration when the strain-rate is too small.

Focusing on the relevant part of the stress-strain curve, i.e. low single digit strain percentages, one can identify the linear region and determine the slope to derive the Young's modulus as shown in Fig. 6.17.

The resulting Young's modulus is $E = 121$ GPa, whereas the ELASTIC method would suggest 352 GPa and 131 GPa by the linear elasticity stress-strain method. All values are given with respect to the simulation box volume. The similarity of both linear elasticity methods is thus also reproduced in the obtained Young's modulus.
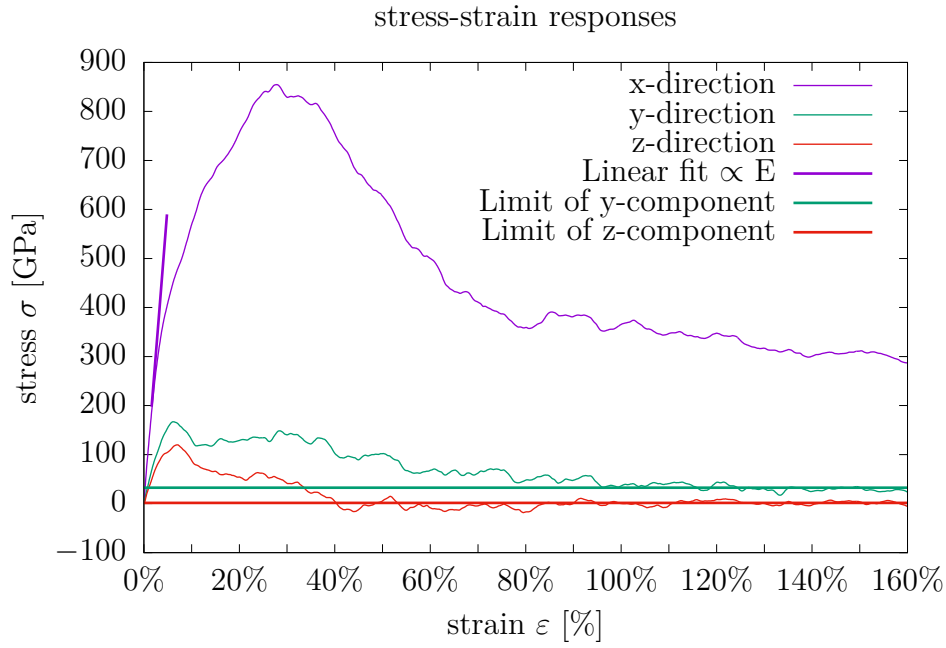
Figure 6.16.: Stress responses σ_x, σ_y and σ_z for an exaggerated strain-range along the x-axis of a TPT-CNM.
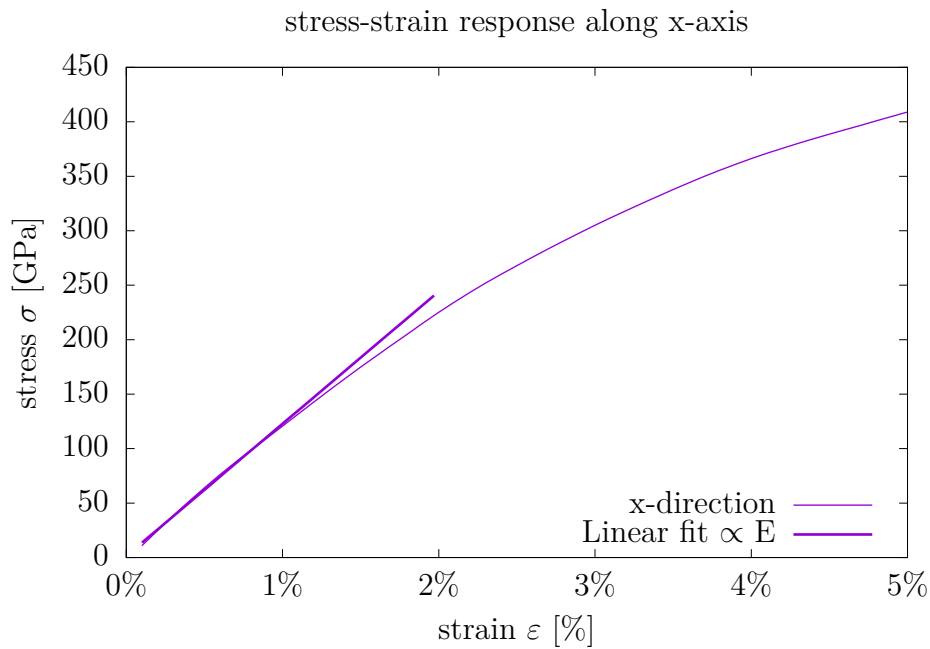
Figure 6.17.: Fit of the linear region of the stress σ_x due to strain along the x-axis of a TPT-CNM.

6.9. Membranes from aliphatic SAMs
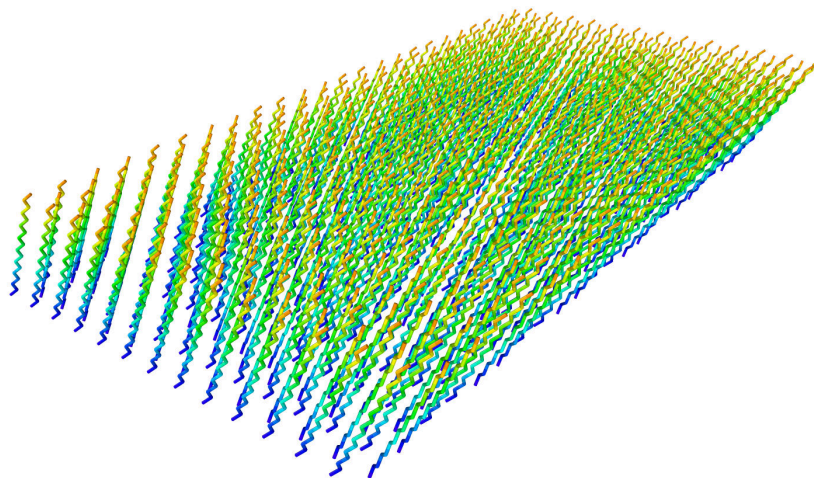
Figure 6.18.: ODT-SAM arranged in the structure described by Love et al. [133].

More recently it has been demonstrated that mechanically stable CNMs cannot only be produced from aromatic precursor molecules, but aliphatic precursors such as 1-Octadecanethiol (ODT) on gold Au(111) [16]. They differ from aromatic molecules in that there are no carbon rings, but only linear alkene chains of hydrocarbons. A minimum chain length of at least 12 carbon atoms was identified to be necessary for CNM formation, most likely due to a lower limit for the density needed for cross-linking [91].

In the case of ODT, the chain is 18 carbon atoms tall with an alternating zig-zag structure. The structural parameters as schematically shown in Fig. 6.19 of decanethiolates on gold Au(111) with lattice constant $a = 2.88$ Å are taken from Ref. [133]. The substrate-attaching sulfur atoms are depicted as gray circles that are arranged in a $\left(\sqrt{3}\,\text{x}\,\sqrt{3}\right)$R30° structure. Alkene chains alternate in orientation (twist angle β as shown in Fig. 6.21 alternating between 0° and 90° to each other) as depicted by the black triangles defined by a c(4 x 2) superlattice structure (long dashed lines). Alternatively, an equivalent description of the structure is possible with a $2\sqrt{3}\,\text{x}\,3$ unit cell (short dashed lines).

Figure 6.19.: Arrangement of decanethiolates on Au(111) lattice, taken from Ref. [133].

Molecules are tilted by an angle $\alpha = 20°$ as shown in Fig. 6.21. The same CNM preparation schemes as previously described can be applied to an ODT-SAM.
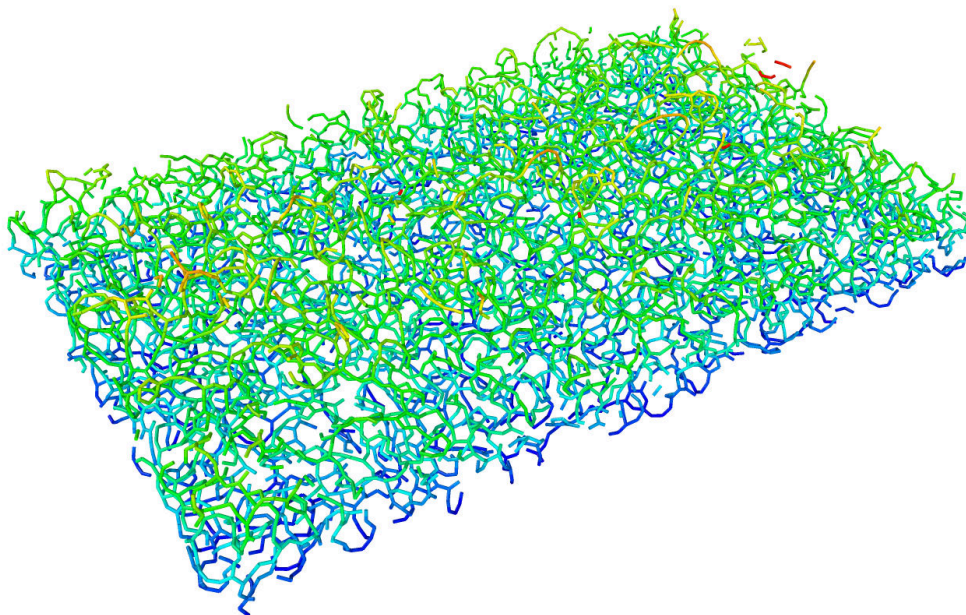
Figure 6.20.: A typical result of vertical momentum dynamics applied to an ODT-SAM, $T = 300$ K, $k = 30$ $\frac{\text{eV}}{\text{Å}}$.

In this example, the SAM as depicted in Fig. 6.18 has the dimensions 72.56 Å x 117.82 Å x 18.66 Å and consists of a total of 11232 atoms or 624 molecules arranged in the structure described by Love et al. for general decanethiols [133]. An example for vertical momentum dynamics (primary and secondary electron momentum transfer) with parameters $T = 300$ K and $k = 30$ $\frac{\text{eV}}{\text{Å}}$ is shown in Fig. 6.20.
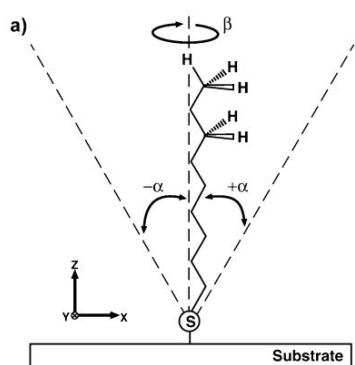
Figure 6.21.: Schematic view of alkenethiolate geometry, taken from Ref. [133].

For the simulation in this chapter, the AIREBO potential was used with Lennard-Jones and torsion terms enabled and a cutoff of 3 Å.

Although no aromatic carbon rings were present in the SAM, cross-linking and successive energy minimization induced the formation of hexagons, which is also observed in graphitization simulations starting with no structure [134]. Overall, the membrane is much more cross-linked but not necessarily denser than its BPT, TPT and NPTH equivalents, also resulting in porosity different from the mentioned membranes that could still allow liquid or gas permeation through more networked internal structures. These aspects are also observed in experiments [16].

The simulated ODT-SAM is mechanically stable, with a Young's modulus of around 352 GPa obtained by the ELASTIC method, 87 GPa by the stress-strain method

and 67 GPa by barostated linear elasticity dynamics. All values are given with respect to the simulation box volume.

The experimental value for an ODT-CNM, $E = 0.592$ GPa [16], is already significantly smaller than the Young's moduli of porous BPT-, TPT- or NPTH-CNMs, which is explained by a "spiderweb-like" structure and high carbon loss [16], the latter of which is not observed in the simulation. Adding to that, it has been shown that membranes from aliphatic SAMs are very brittle, which makes them unfavorable for the intended usecases, e.g. as supports or filtration membranes [91].

7. Molecular dynamics modeling of nanoindentation

This chapter will discuss a molecular dynamics simulation approach to nanoindentation as discussed in Ch. 5.11. It gives another perspective on how to determine the Young's modulus that can very well be related to the experimental procedure which is not the case for the previously discussed theoretical approaches. The model system consists of a BPT-CNM and a spherical repulsive force indenter as depicted schematically in Fig. 7.1a.

7.1. Simulation setup

(a) Schematic representation of the nanoindentation simulation setup, where a repulsive sphere is moved towards the membrane.

(b) Top view with schematic representation of the clamp regions (black lines).
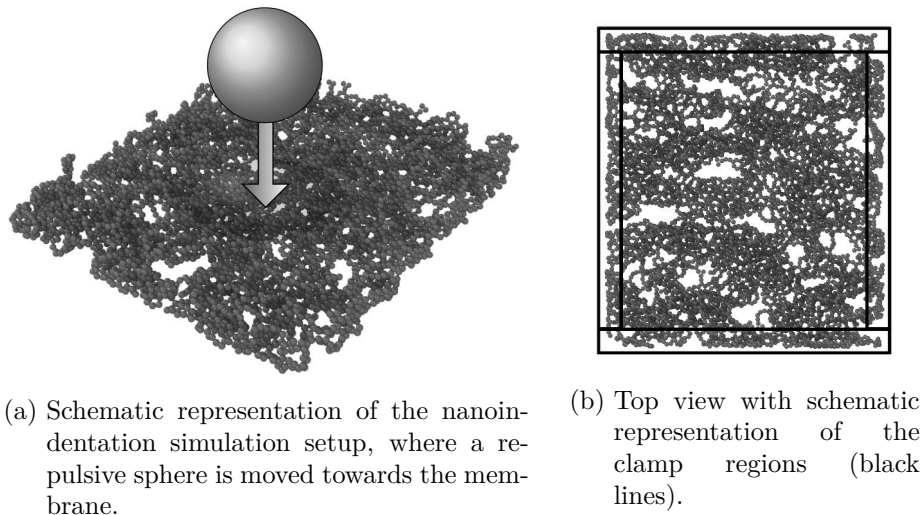
Figure 7.1.: Visualization of the molecular dynamics nanoindentation process with schematic of clamped regions (black lines).

To prepare the membrane for indentation, it has to be held in position. This is achieved by lateral clamping in x- and y-direction of the membrane similar to the clamping employed for stress-strain simulations as presented in Ch. 6.3, i.e. regions (*region* command in LAMMPS) with a width of around 5 Å are positioned at the maximum lateral extent of the membrane encompassing a group of atoms (*group* command in LAMMPS) to be used as clamps (see Fig. 7.1b). These atoms are excluded from the dynamics by setting their forces to zero with the LAMMPS *fix setforce 0 0 0* command. The simulation box is set to be shrinkwrapped to allow the membrane to deform under indentation.

With the membrane clamped in place, a spherical indenter (*fix indent* command in

LAMMPS) with radius R is placed above the membrane. It exerts a repulsive force $F(r) = -K(r - R)^2$ with a force constant K on each atom fulfilling $F(r) = 0$ for $r > R$ [135]. The sphere is brought closer to the membrane at a stepwise pace. After each step, the energy of the system in the indented configuration is minimized. When the desired indentation depth is reached, the indenter is removed, again in a stepwise pace allowing the membrane to relax at each minimization.

During this process, the resulting force in the membrane is logged with regard to the indentation depth. This is different from the experiment, where the force on the indenter is measured, thus resulting in a flipped sign of the force as well as potential errors from internal stresses of the membrane.

7.2. Qualitative insights

The spherical indenter is not visualized in the following Figs. 7.2 to 7.4 to focus on changes inside the material during the process.

The top views as shown in Fig. 7.2 emphasize the lateral extent of the indenter which can be seen from the portion of blue colored bonds increasing, i.e. atoms are pushed to positions with lower z-coordinate going from Fig. 7.2a to 7.2c. Also, a slight increase in the size of holes through stretching within the indentation area can be observed, which aligns with the possibility of destruction of the membrane during nanoindentation as observed in experiments [121]. The same holds for perspective views as shown in Fig. 7.3. The lateral view serves as an impression of how deep the indenter is pushed
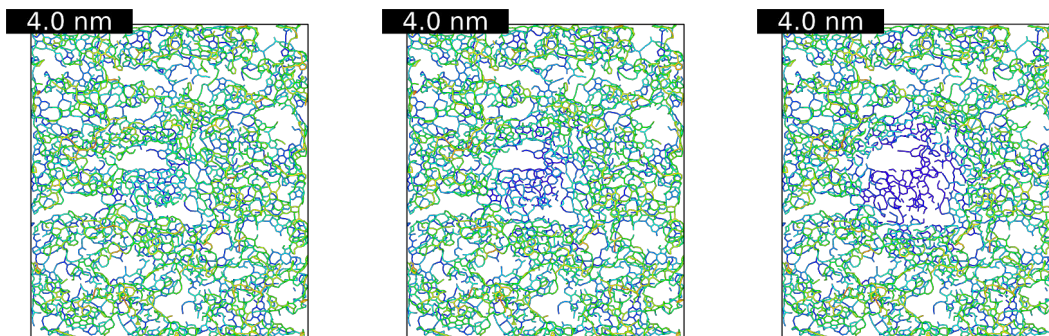
(a) Top view at the beginning.   (b) Top view at half the final indentation depth.   (c) Top view at final indentation depth.

Figure 7.2.: Top views of the indentation process at various timesteps. Color-coding represents height of the membrane.

into the membrane with increasing depth from Fig. 7.4a to 7.4c. In the end position of the indenter as shown in Fig. 7.4c, a defect formation starts to show on the lefthand side of the membrane bulge.

7.3. Determination of the Young's modulus

An exemplary loading and unloading result of molecular dynamics nanoindentation for a BPT-CNM is shown in Fig. 7.5. The sign of the force data has not been flipped, thus
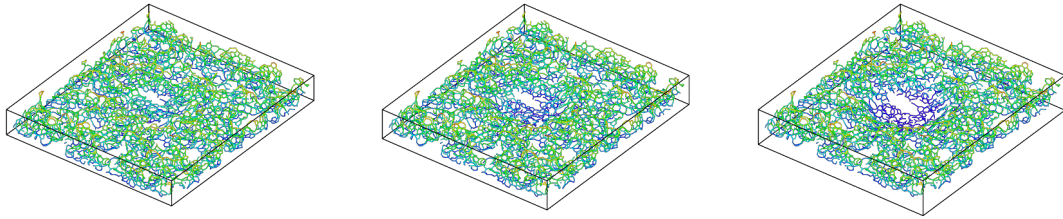
(a) Perspective view at the beginning.

(b) Perspective view at half the final indentation depth.

(c) Perspective view at final indentation depth.

Figure 7.3.: Perspective views of the indentation process at various timesteps. Color-coding represents height of the membrane.
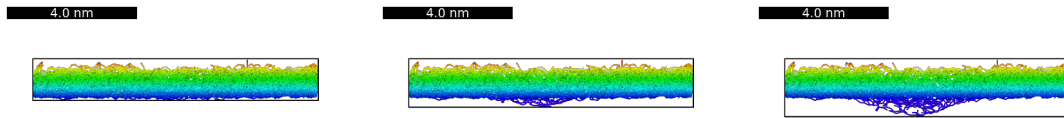
(a) Lateral view at the beginning.

(b) Lateral view at half the final indentation depth.

(c) Lateral view at final indentation depth.

Figure 7.4.: Lateral views of the indentation process at various timesteps. Color-coding represents height of the membrane.

the actual force exerted by the membrane is shown. For this simulation, the radius of the indenter was chosen as $R = 30$ Å with a force constant $K = 40 \frac{eV}{Å^3}$. Lateral dimensions of the membrane are 87.5 Å x 98.9 Å with a height of 12.8 Å. Figs. 7.2 to 7.4 visualize the indentation from various points of view. The resulting force during the indentation process shown in Fig. 7.5 starts at $d = 0$ Å with a non-zero force in z-direction $F_z \approx 13.5 \frac{eV}{Å}$ due to mechanical stress in the membrane that comes from the lateral clamping as depicted by the orange curve.

Force is calculated using the force per atom quantity *compute property/atom fz* which is summed and reduced over all atoms using *fix reduce sum*, ultimately turning the calculated force into an extensive quantity, i.e. it has to be divided by the total number of atoms $N = 7200$ for the calculation of the Young's modulus. Data presented in the graphs is unscaled.

The force curve stays constant up until approximately $d = 3$ Å, which is due to the placement of the indenter sphere above the membrane to avoid unphysical behavior if placed to close to the membrane at the first timestep. After that, the force decreases (existing stress is compensated for by the indentation). The indenter reaches its maximum indentation depth at $d = 5.4$ Å from its initial position, resulting in a bulge of ≈ 4.4 Å of the bottom of the membrane at the deepest point due to stretching and thinning.

The indenter is then removed by reversing the previous procedure as shown in the bot-

tom half of Fig. 7.5, where the forces inside the membrane oscillate around a residual net force of around $F_z \approx -5 \frac{\text{eV}}{\text{Å}}$. This behavior comes from the atoms finding a new energy minimum at each step with the indenter still influencing them, thus jumping into a new position and relocating the stress. The indentation bulge remains even if the indenter is removed completely, explaining the non-vanishing force that has an opposite sign to the previously observed residual force. The behavior can be summarized as a type of stress hysteresis induced by the nanoindentation resulting in irreversible changes and damage of the material.

To compare the force-indentation depth curves with experiments, the sign has to

Resulting forces in z-direction in the membrane under loading/unloading
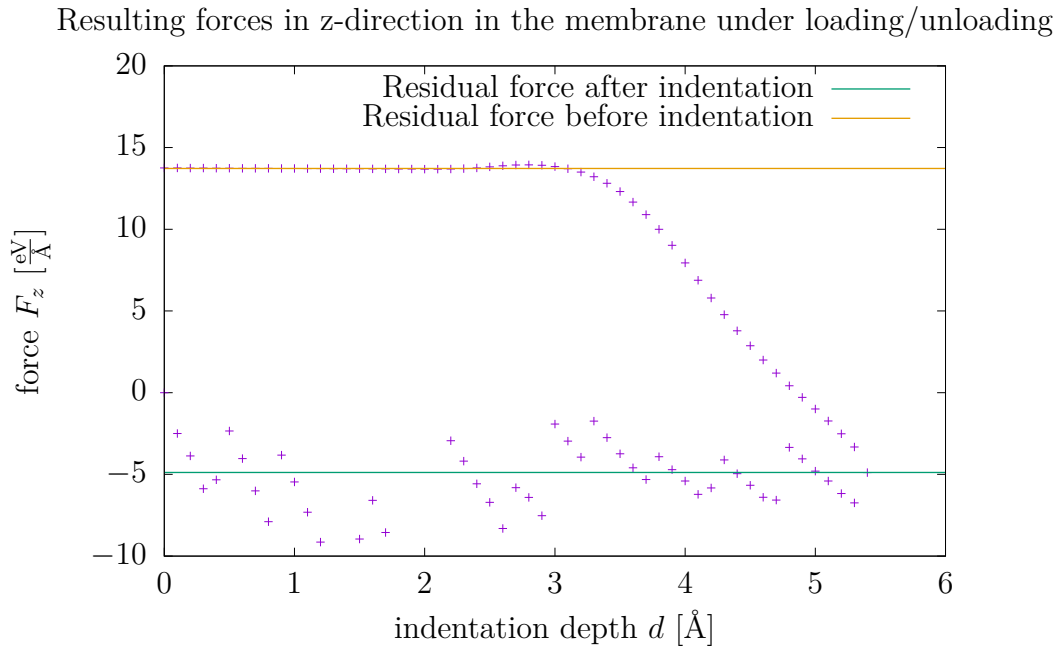
Figure 7.5.: Resulting forces in z-direction during molecular dynamics nanoindentation loading (starting top left) and unloading (starting bottom right).

be flipped to give the force on the indenter. Also, residual stress effects have to be neglected as they would not be part of the experimental measurement. The return path of experimental nanoindentation is different as well with much less pronounced thermal effects curve hysteresis as the indenter feels a net force of all surrounding atoms, thus being not as sensitive to interatomic restructuring.

Therefore, to discuss the derivation of the Young's modulus from the indentation data, only the linear-cubic part as depicted in Fig. 7.6 that is identical with the experimental process will be discussed. This part of the curve can be fitted with a function that is linear and cubic in the indentation depth d as discussed in the experimental overview in Ch. 5.11. Further care has to be taken since the indentation does not start at 0 Å as it would in the experiment but at around 3.0 Å thus shifting the curve and influencing the linear term of the fit function.

There are various models motivating different forms of fit functions depending on the geometry considered as discussed in the experimental overview. All models assume a membrane of macroscopic lateral dimensions and often use finite-element methods to derive a force-function containing the Young's modulus. Thus, continuum material properties are considered instead of those at the molecular level, which is the case for
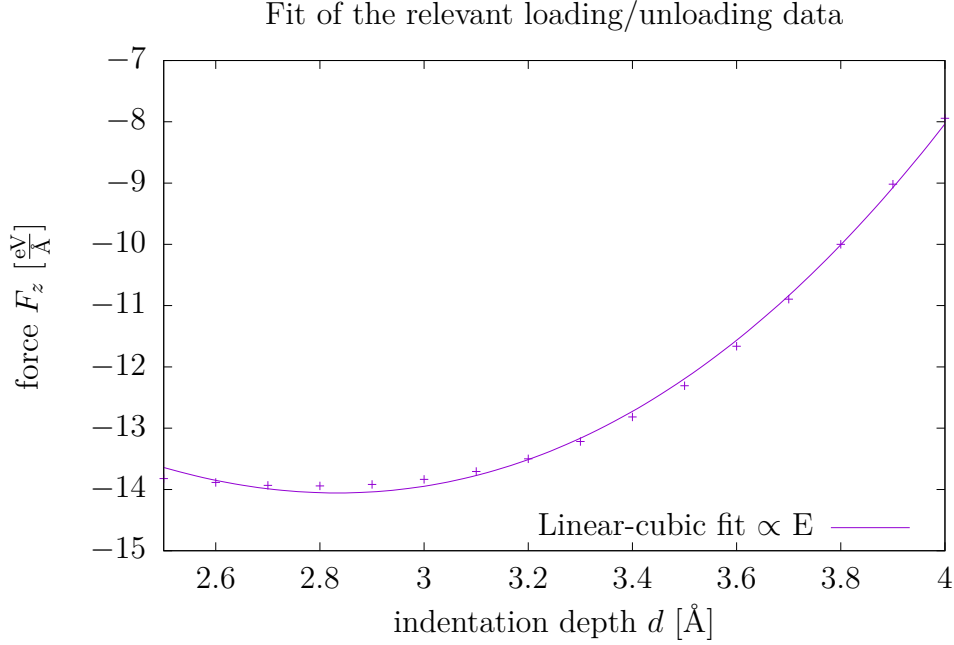
Figure 7.6.: Zoomed-in simulated nanoindentation force data with flipped sign to represent loading of the indenter.

the simulated CNMs that only make up a tiny fraction of a real membrane (≈ 100 Å vs. several μm up to cm in lateral size). It is therefore not obvious as to which model formula to choose. All models concerned with non-linearity, i.e. macroscopic indentation depths are excluded from the beginning. Then there are models that incorporate the indenter geometry and those that do not. The spectrum ranges from a doubly clamped beam shaped membrane with a point load to a thick circular membrane with non-negligible bending stiffness [119], i.e.

$$F = \left(\frac{30.78 w t^2}{l^3} E_1^{2D} + \frac{12.32}{l} \right) \delta + \frac{8 w E_1^{2D}}{3l^3} \tag{7.1}$$

for a beam shaped membrane where w, l and t are the width, length and thickness of the beam [119] and

$$F = \left(\frac{4\pi t^2}{3(1-\nu^2)R} E_2^{2D} + \pi R \sigma_0^{2D} \right) \left(\frac{d}{R} \right) + E_2^{2D} q^3 R \left(\frac{d}{R} \right)^3 \tag{7.2}$$

for a circular membrane of thickness t with pretension σ_{2D}, and q is expressed by $1/(1.05 - 0.15\nu - 0.17\nu^2)$ [119] with the Poisson's ratio $\nu = 0.35$ for CNMs [136]. Since the simulated membranes dimensions are tiny compared to the continuum model, both models might be applicable to some extent when ignoring bending stiffness. Thus the "true" Young's modulus determined by molecular dynamics nanoindentation lies somewhere inbetween those two limits. With the fit parameter $\beta = 0.45 \frac{eV}{Å^2}$ for the cubic term, the relation

$$216.00 \text{ GPa} = \alpha \frac{3l^3}{8w} = E_1^{2D} > E_2^{2D} = \alpha \frac{R^2}{q^3} = 23.77 \text{ GPa} \tag{7.3}$$

can be found to bound the nanoindentation Young's modulus after conversion of units. This puts the results somewhere below the barostated approach (see Ch. 6.8) with a value of 121 GPa and the ELASTIC result of 352 GPa. Compared to the experimental result of $E^{\text{2D}} = 12.5$ GPa for a single layer CNM [119], the presented theoretical range overestimates the Young's modulus by up to ten times. The lower bound, which is coincidentally calculated identical to the Young's modulus of graphene [119], is close to the experimental result, off by around a factor of two.

This might be indicative of finite-size effects. The lateral extent of the membrane is too small to actually identify continuum properties and the indenter geometry makes up a huge portion of the membrane's dimensions. Also, the size of clamp regions might play a role in finite-size effects.

8. Ring statistics and aromaticity

An experimental observation backed by NEXAFS, HREELS and IRRAS measurements is the loss of aromaticity in the process of irradiation of aromatic precursor SAMs. Aromaticity is a chemistry term describing cyclic planar structures, so called cycloalkenes with delocalized electrons in π^*-resonance that stabilize the ring [137]. Loss of aromaticity is believed to be a key indicator of molecular cross-linking [117]. Carbon rings of the aromatic precursor molecules get broken apart in the irradiation process which gives way to new bond structures to form and deliver the necessary glue to form mechanically stable membranes. However, mechanically stable membranes can also be created from aliphatic precursors, albeit with a much smaller Young's modulus [16], indicating that high initial aromaticity might play a role in mechanical stability and that internal structure is correlated with the initial configuration.
All of the mentioned experimental methods are able to determine a qualitative difference between SAM and CNM aromaticity indirectly, e.g. through an overall decrease in signal strength of the observed quantity.
In this chapter, an approximate method for quantitative and qualitative measurement of aromaticity in a molecular dynamics environment will be presented. The term "aromaticity" will be used synonymously with "number of intact carbon rings" for this purpose and is thus a weaker formulation than the chemical definition.

8.1. Simulation setup

Since atom positions are exactly known in molecular dynamics simulations, the idea is to find and count hexagons in both SAM and CNM. This is easy for linear precursor molecules as e.g. BPT and TPT are known to consist of two and three carbon hexagons, respectively. NPTH on the other hand has overlapping hexagons thus introducing ambiguity in the definition of which bonds belong to which hexagon, while at most three hexagons might share one common vertex and two sites. This type of structure also appears in the final CNM e.g. as graphene flakes that originate from broken up and rearranged rings of a molecule. Thus, although overlapping, all hexagons are counted separately such that relative aromaticity never exceeds 100 %.
Finding hexagons in 3D space is not trivial. From a pure geometric standpoint only a brute-force algorithm would be possible as planar hexagons could be oriented arbitrarily in space. When allowing for even slight deviations from a planar structure, a geometric search becomes virtually impossible.
Some molecular dynamics visualization packages such as VMD [138] make use of a sophisticated data structure called graph to store atom positions with respect to the atom type and bond length. A graph is a network of nodes and edges. In this case, each node describes an atom's properties, e.g. position and charge.

Edges connect nodes if neighboring atoms are within the typical bond length of the atom type, e.g. 1.42 Å for C-C bonds, plus some tolerance. With that data structure in place, a graph search algorithm such as depth first search (DFS) can be used to very efficiently find every possible path of a specified length n (the number of sites of the ring) where the starting point is the same as the end point, a so called cycle. Thus, rings are found regardless of their spatial orientation or deviations from a plane. An alternative approach lies in the utilization of correlation functions $g(r)$ that essentially count neighbors [132].

8.2. Results

VMD [138] is used for the ring statistics employing a Tcl script to select rings with $n = 6$, i.e. hexagons, *atomselect $i "ringsize 6 from all"*, count and highlight them visually. Fig. 8.2 shows the initial TPT-SAM with a relative aromaticity of 100 % and all rings depicted as bold black lines. Vertical bonds connecting the rings are an artefact of the visualization and not counted as a contribution to the hexagons. Various snapshots of the irradiation process are presented in Fig. 8.4. From these images, the qualitative observation of a decrease in aromaticity as measured by the destruction of hexagons is obvious from the decrease in bold black lines and the appearance of light gray lines indicating non-aromatic areas.

Besides that, a quantitative evaluation is possible, when comparing the fraction of atoms that are part of a hexagon to the total number of atoms (assuming 100 % aromaticity in the beginning), which is shown in the graph in Fig. 8.1. Additionally to the decrease during irradiation ($0 \leq t \leq 1$ ps), a slight increase of 10 % can be observed to the end ($t > 3$ ps) of cooling which starts at 1 ps. The final configuration at around 40 % of the initial aromaticity is shown in Fig. 8.3.

Thus, there is an overall decrease of aromaticity of around 60 % for the exemplary TPT-CNM which is in qualitative agreement with experimental results.
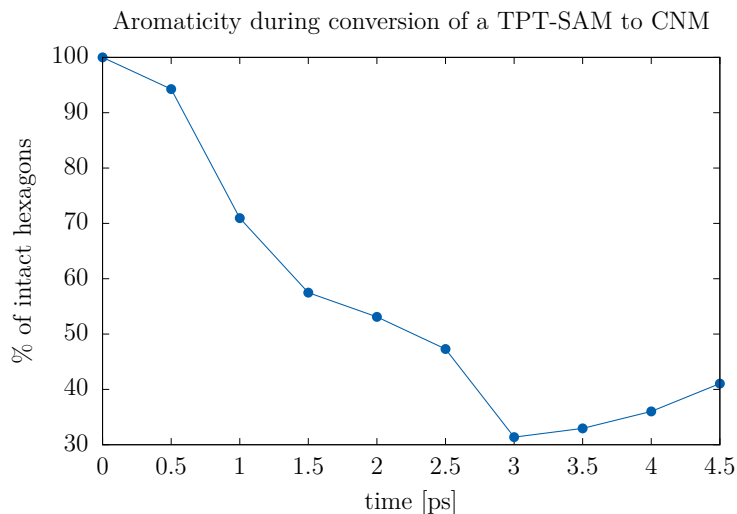
Figure 8.1.: Aromaticity during one simulation of the conversion of a TPT-SAM to a CNM.
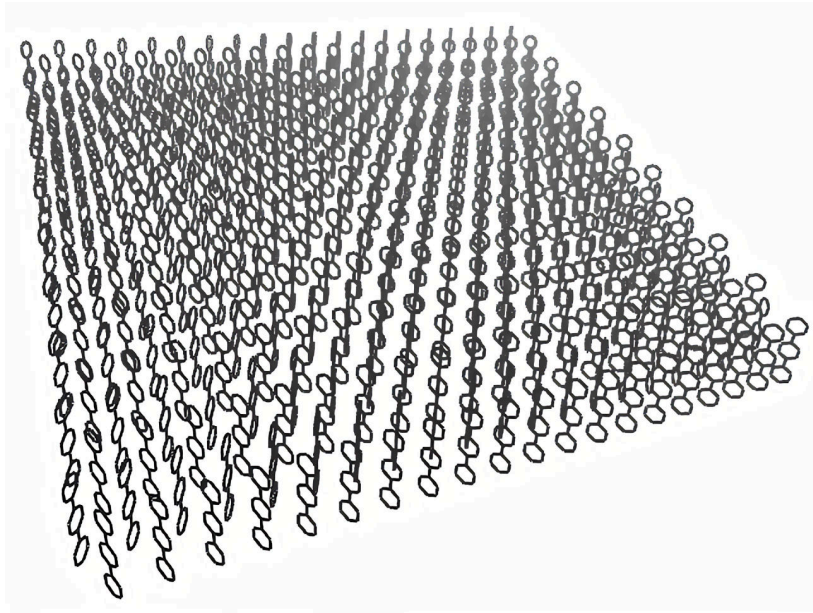
Figure 8.2.: Initial TPT-SAM ring visualization (bold black lines).
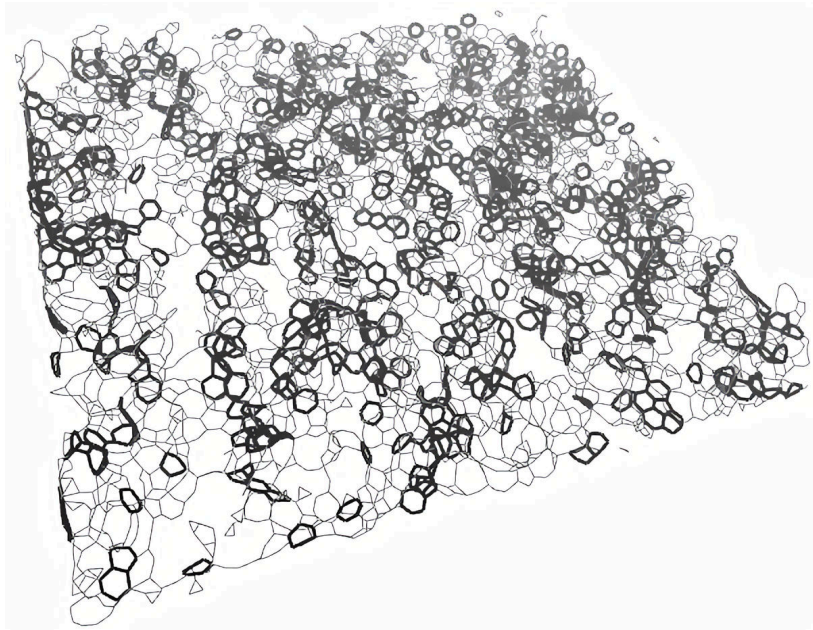
Figure 8.3.: Final TPT-CNM ring visualization (bold black lines).
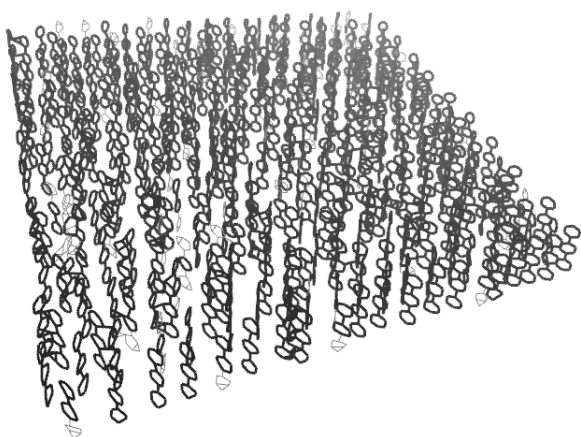
(a) During irradiation at timestep 300
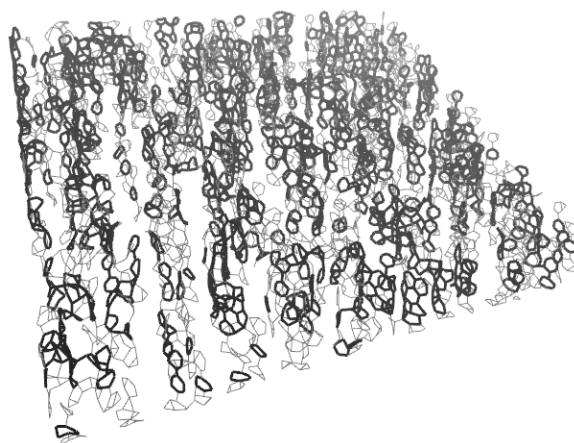
(b) During irradiation at timestep 900
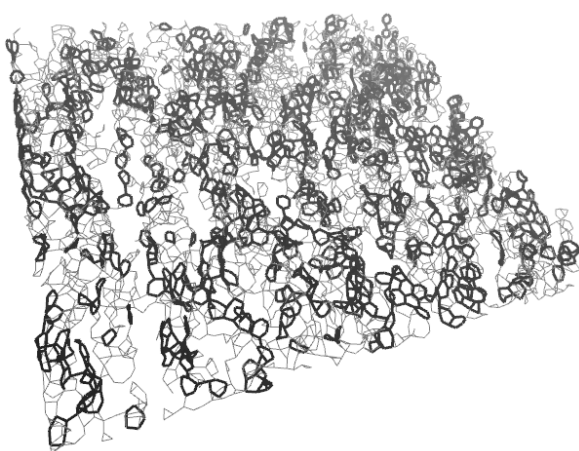
(c) During irradiation at timestep 1500
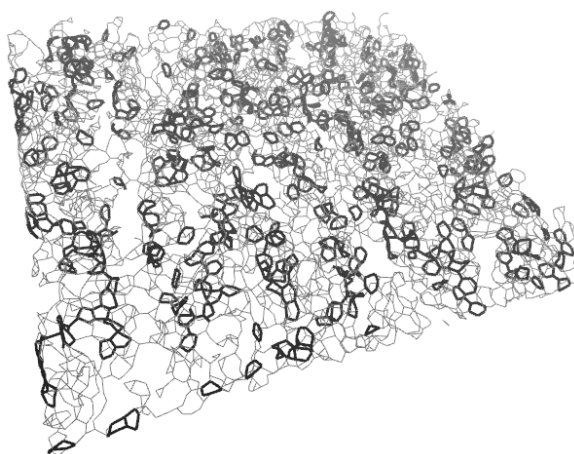
(d) During cooling at timestep 10000
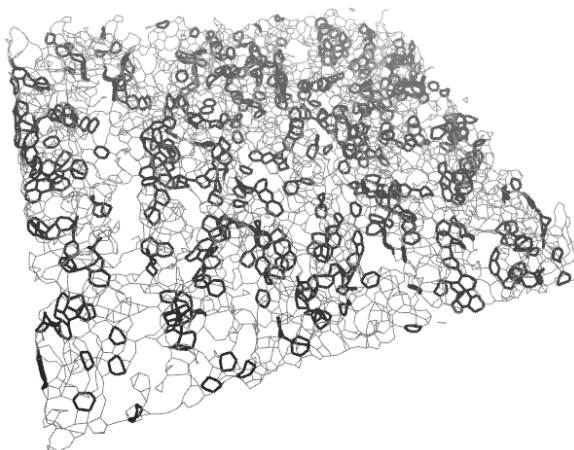
(e) During cooling at timestep 20000
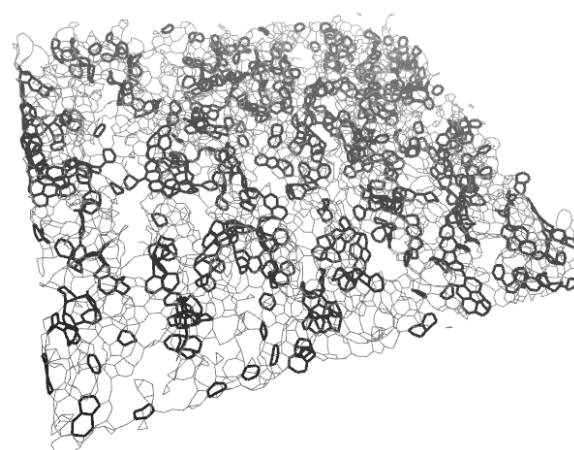
(f) During cooling at timestep 30000

Figure 8.4.: Visualization of intact carbon rings (bold black lines) at various timesteps of the transformation from TPT-SAM to CNM.

9. Simulated atomic force microscopy (AFM) images

In this chapter a more artistic than empirical approach to atomic force microscopy (AFM) images boiled down to the experimental method's inherent limited resolution will be discussed.

9.1. Simulation setup

For that purpose there will be made no difference between tapping and contact mode AFM imaging. The resolution is assumed to be limited by the size and pyramid shape of the cantilever tip only and thus its ability to clearly depict individual atoms that are positioned highly irregularly including hills and valleys as well as voids bigger and deeper than the tip itself. While one can make clear statements about STM and AFM images of the self-assembled monolayer, it is only possible to talk about the overall roughness and porosity of the surface of the resulting membrane as almost no regularities are left after irradiation. The latter aspects are closely related to the highly selective permeation property of CNMs [17].

Since there is no quantitative method to generate AFM images from atom coordinates apart from the quantum mechanical approach presented in Ref. [111], which is incompatible with systems as large as the considered CNMs, the method proposed in the following tries to create a stylized and reproducible way to create images that are visually similar to AFM images using the open-source computer graphics package Blender from the Blender Foundation [139]. One key aspect for similarity is the color scheme. Perception of depth is highly influenced by the pseudocolor chosen for the encoding of depth, e.g. from black to gold or grayscale.

Atom positions in plain xyz-format can be readily imported into Blender by enabling the addon "Atomic Blender" inside the user preferences. This addon attaches a chosen geometry mesh, e.g. an icosphere, to each atom position. The radius of the sphere can be tweaked to influence the empty space between atoms. If one would just assign a simple single-color shader to all spheres, the image would be a perfect representation of the the atoms as e.g. depicted by spheres or the van der Waals radius. Just by post-processing means, e.g. Gaussian blurring or pixelization, this result cannot be adequately modified such that the image gets close to an experimental AFM image. Thus a cloth, i.e. a subdivided plane with a cloth modifier, is placed above the atoms and pulled towards the membrane by gravity. Atoms are fixed in position and held rigid. The cloth can thus fall into the crevices but since it has limited stretch, it is limited in how deep it penetrates in depth (z-direction) thus simulating the limited resolution of the cantilever tip. A shader encoding the height with a color gradient similar to the experiment is added.

Screenshots of the Blender scene used for the cloth rigidbody simulation are shown in Fig. 9.1 for the initial configuration and Fig 9.2 for the end result ready for rendering.
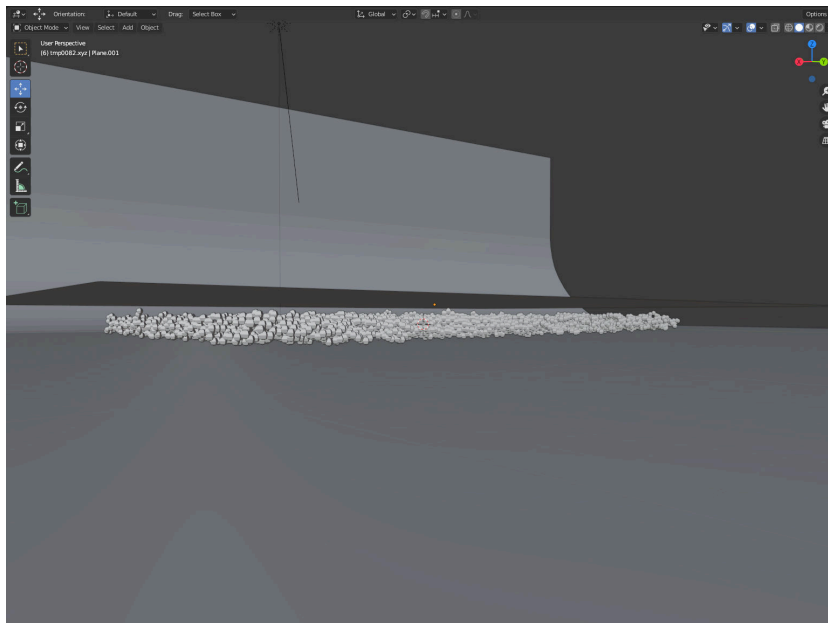
Figure 9.1.: Screenshot of the Blender scene for an AFM image of a TPT-CNM. Atoms are represented as icospheres (light gray). The plane acting as a cloth (dark gray) is placed above the membrane in the beginning of the simulation.
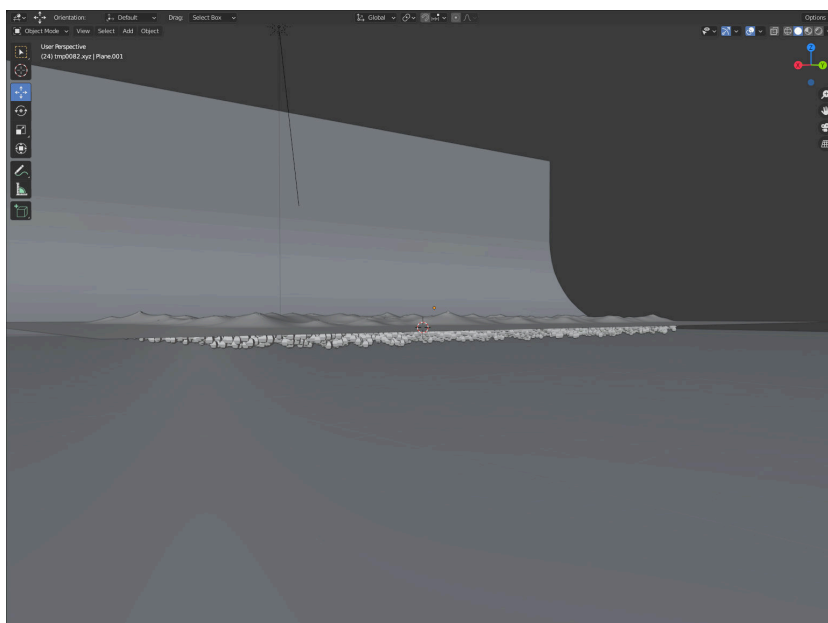
Figure 9.2.: Screenshot of the Blender scene for an AFM image of a TPT-CNM. Atoms are represented as icospheres (light gray). The plane lays on top of the membrane showing limited resolution hills and valleys at the end of the simulation.

9.2. Qualitative insights

Fig. 9.3 shows the initial configuration of a BPT-SAM, where its (2×2) hexagonal structure can be identified. The image for the resulting CNM is shown in Fig. 9.4. Parameters used for this membrane are identical to the membrane shown in Fig. 6.5 with $T = 700$ K, $k = 60 \frac{eV}{\mathring{A}}$.

The resulting CNM shows signs of a rougher surface with denser and less dense areas and a total loss of the initial regularity. As for porosity, large enough completely black areas, i.e. holes in the membrane, are scarce. Overall, a drastic structural change can be observed similar to experimental AFM results.
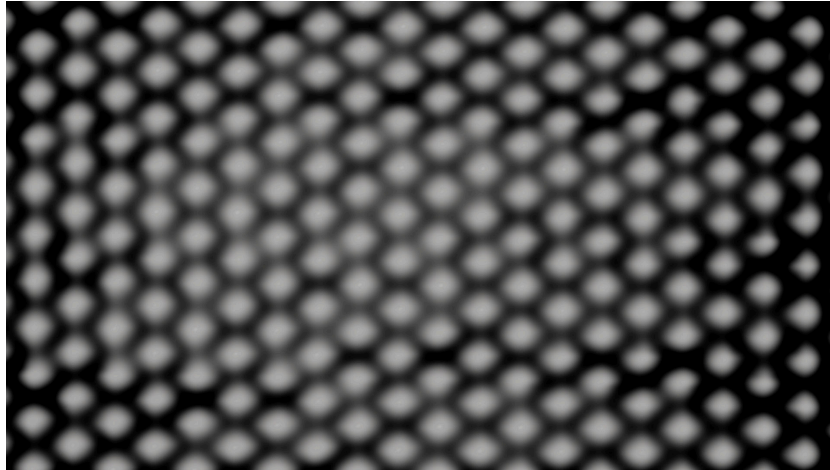
Figure 9.3.: Render of a simulated AFM image of a BPT-SAM. Grayscale encoding from black to gray for the height profile from lowest to highest z-coordinate.
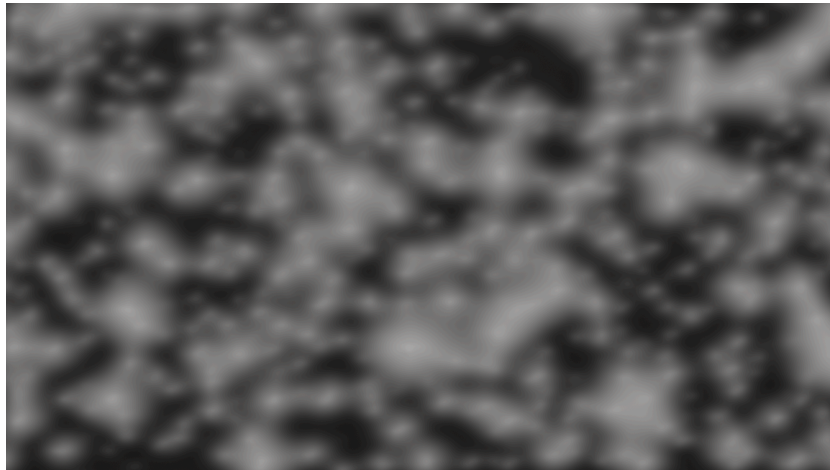
Figure 9.4.: Render of a simulated AFM image of a BPT-CNM. Grayscale encoding from black to gray for the height profile from lowest to highest z-coordinate.

For comparison, Fig. 9.5 and 9.6 show the initial SAM made from TPT precursors and the resulting membrane, respectively. The parameters for this membrane are $T = 700$ K, $v = 35 \frac{\text{Å}}{\text{ps}}$ and $k = 30 \frac{\text{eV}}{\text{Å}}$ as shown in Fig. 6.9. Again, the initial SAMs $(\sqrt{3} \times \sqrt{3})$ structure is clearly reproduced in the simulated AFM image of the SAM also depicting the different orientations of molecules in the $(2\sqrt{3} \times \sqrt{3})$ unit cell. The TPT-CNM has larger holes and overall less dense structure than the BPT-CNM, which can be seen by the much denser hill areas. Also, the areas depicted as black have much higher probability to be true holes due to their much more pronounced size and shape.

Figure 9.5.: Render of a simulated AFM image of a TPT-SAM. Grayscale encoding from black to gray for the height profile from lowest to highest z-coordinate.
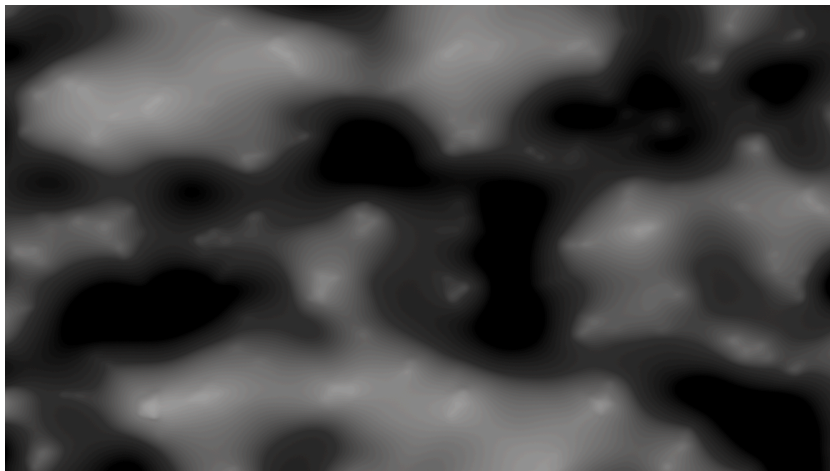
Figure 9.6.: Render of a simulated AFM image of a TPT-CNM. Grayscale encoding from black to gray for the height profile from lowest to highest z-coordinate.

10. Water permeation analysis

As discussed in the experimental overview in Ch. 4, liquid and gas permeation properties of CNMs are of key commercial interest with potential in replacing conventional filtration means. Studies [17] have shown that there is high molecular selectivity as well as high permeance for water which is motivated by the existence of pores in the membrane as potentially revealed by AFM. It is assumed that the process behind molecular sieving is supported by single-file water permeation modes. This chapter will present a molecular dynamics simulation approach using an explicit solvent model to visualize the transport mechanism.

10.1. Prerequisite setup to initialize CNM and water geometry

Setting up a carbon nanomembrane for a molecular dynamics permeation simulation is a multi-step process that starts with the generation of a block of water molecules of the same lateral size as the simulation box volume encompassing the CNM. The process will be discussed for a TPT-CNM of 7200 atoms and dimensions 87.6 Å x 98.6 Å x 11.6 Å.

(a) Initial 25 x 30 x 6 water block.　　(b) TPT-CNM placed above the initial water block.
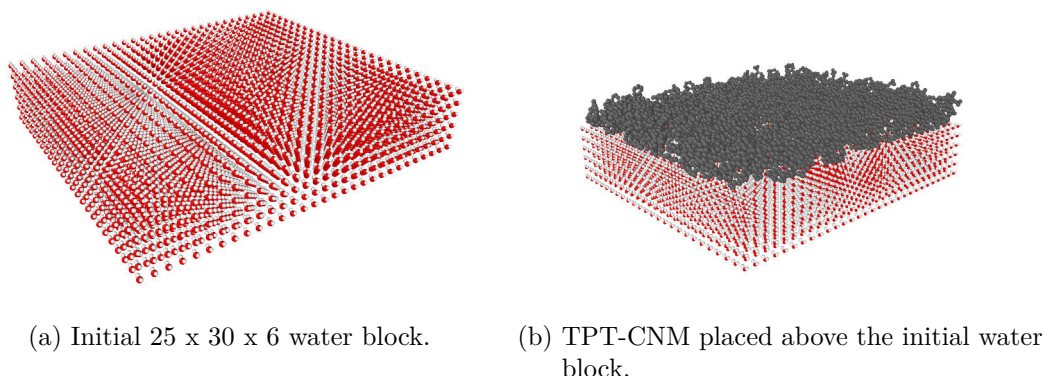
Figure 10.1.: Prerequisite preparation of the combined CNM (gray spheres) and water (H$_2$O molecules depicted by white (H) and red (O) spheres) system.

Generation and placement of the explicit solvent: Water molecules are placed along a subdivided cubic grid, where a water molecule is assigned to each vertex as shown in Fig. 10.1a. The block of water is generated with the help of moltemplate [140] by specifying the number of subdivisions of the grid as 25 x 30 x 6, i.e. placing 4500 water molecules containing a total of 13500 atoms inside the block with a spacing

of around 3.5 Å between neighboring molecules. Initial configuration of the water molecules is not as relevant as there are additional steps to treat the water block before the actual permeation simulation, thus there is no physical meaning behind the chosen spacing.

Merging solvent and membrane geometries: The next step is to place the CNM above the water block, again only loosely placing it such that all water molecules are below the membrane as depicted in Fig. 10.1b. The combined system of water molecules and the TPT-CNM would now be ready for permeation simulation. However, in order to speed up the simulation, water molecules should not have to diffuse to the membrane at first before being able to enter pores, but rather be as close to the membrane as possible, because it would take too long for a water molecule to find a pore by diffusion only.

Packing optimization: To bring the water molecules closer to the membrane, the packing optimizer PACKMOL [141] is used. Optimization parameters are chosen such that both the distance between neighboring water molecules is minimized as well as the empty space between water and CNM. Carbon atoms are fixed in position during the procedure, the result of which is shown in Fig. 10.2.
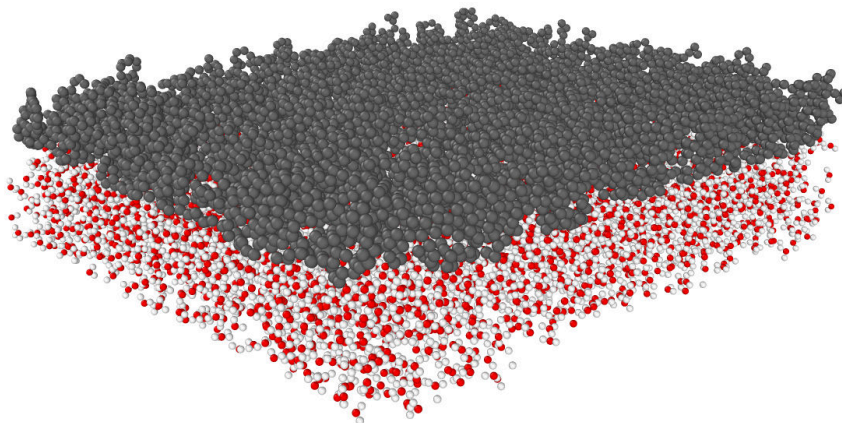
Figure 10.2.: Optimized packing of the water molecules (H_2O molecules depicted by white (H) and red (O) spheres) below the membrane (gray spheres).

This marks the final configuration ready for permeation studies.

10.2. Molecular dynamics setup of permeation analysis

For the permeation study presented in this thesis, an explicit model as defined by long-ranging Lennard-Jones type Coulombic interactions described by ϵ and σ as shown in Ch. 2.9 between constituents of the system, i.e. carbon (C), hydrogen (H) and oxygen (O) is employed. This mandates parameters for bond force field, angles force field, and pairwise interaction coefficients (*bond_coeff*, *angle_coeff* and *pair_coeff* in LAMMPS) to describe all atomic interactions between the CNM and the water. The following parameters are used as suggested in Refs. [142, 143] and by the TIP3P model [77]:

- $\epsilon = 0.1553$ eV and $\sigma = 3.166$ Å for O-O interaction.

- $\epsilon = 0.114$ eV and $\sigma = 3.28$ Å for C-O interaction.

- $\epsilon = 0.0$ eV and $\sigma = 3.28$ Å for C-H interaction.

- $\epsilon = 0.068443$ eV and $\sigma = 3.407$ Å for C-C interaction.

- Pair coefficients for H-H and O-H are set to zero and H_2O molecules are considered rigid.

Bond and angle force field parameters are chosen to be of the *harmonic* type. All carbon atoms are considered immobile, thus there is no stretching or bulging of the membrane that might improve or hinder the transport mechanism. The system is allowed to find a local minimum in configuration space consisting of membrane and water using a Langevin thermostat such that water molecules have some random initial velocity. The water reservoir is then pressurized by application of a force in upwards z-direction towards the membrane. This is done with the *fix addforce z* command in LAMMPS, restricted to the group of water molecules only. Force will be applied during the whole simulation and with a magnitude of around 7 pN to speed up the permeation process. This allows for qualitative inspection of where single-file mode permeation occurs. An exemplary snapshot of the simulation is shown in Fig. 10.3. There, a few areas of permeation can be identified visually indicated by H_2O-molecules as depicted by white and red spheres going through the membrane and looking like a fountain coming out the membrane. These molecules will re-enter the reservoir through periodic boundary conditions.

10.3. Qualitative results from simulated water permeation

From the visualization in Fig. 10.3 it is not entirely clear where the transport of water molecules occurs and which path the molecules take through the membrane. This can be improved by identifying the pores or holes that take part in the process. However, it is virtually impossible to find pores and channels, that may bend arbitrarily inside the membrane, thereby connecting two pores that need not necessarily be at the same lateral position on both sides of the CNM.
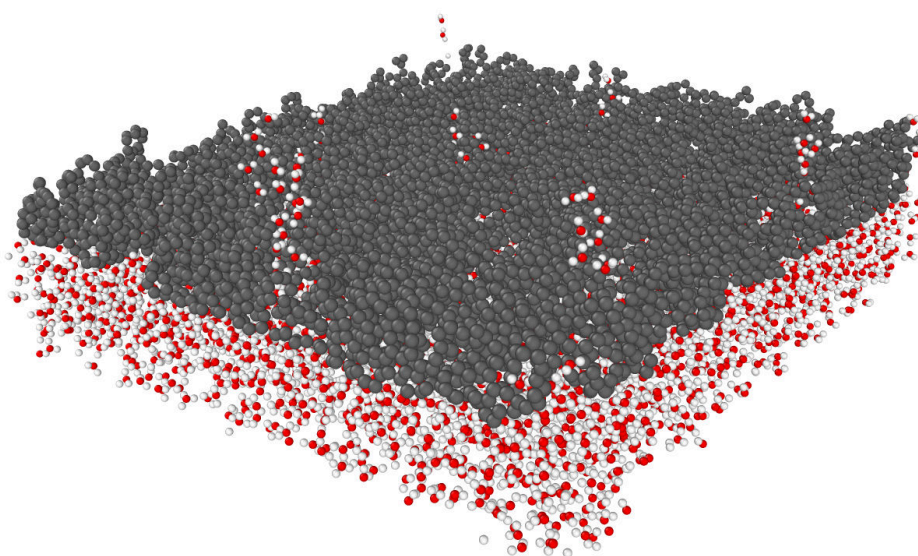
Figure 10.3.: Perspective view of single-file mode water (H_2O molecules depicted by white (H) and red (O) spheres) permeation through the pores of a CNM (gray spheres).

Transport channels that go straight through the membrane can readily be found by projection of atom coordinates to $z = 0$ and rasterization of the resulting 2D data to find holes in the membrane through brute-force searching [144]. Holes and their corresponding radius are depicted as spheres and overlayed on top of the permeation images to help in interpreting the transport behavior. An example can be seen in the top view of the membrane in Fig. 10.5 where holes are represented as blue spheres and water molecules have been colored black for better contrast. Together with the perspective view of a different timestep in Fig. 10.6 this allows for a qualitative determination of which pores contribute most to the flow. A cross-sectional side view of a pore taking part in the single-file mode permeation is shown in Fig. 10.4.

Surprisingly, there seem to be areas that appear to have large holes, e.g. in the middle and top middle of the membrane when viewed from the top in Fig. 10.5, where at no
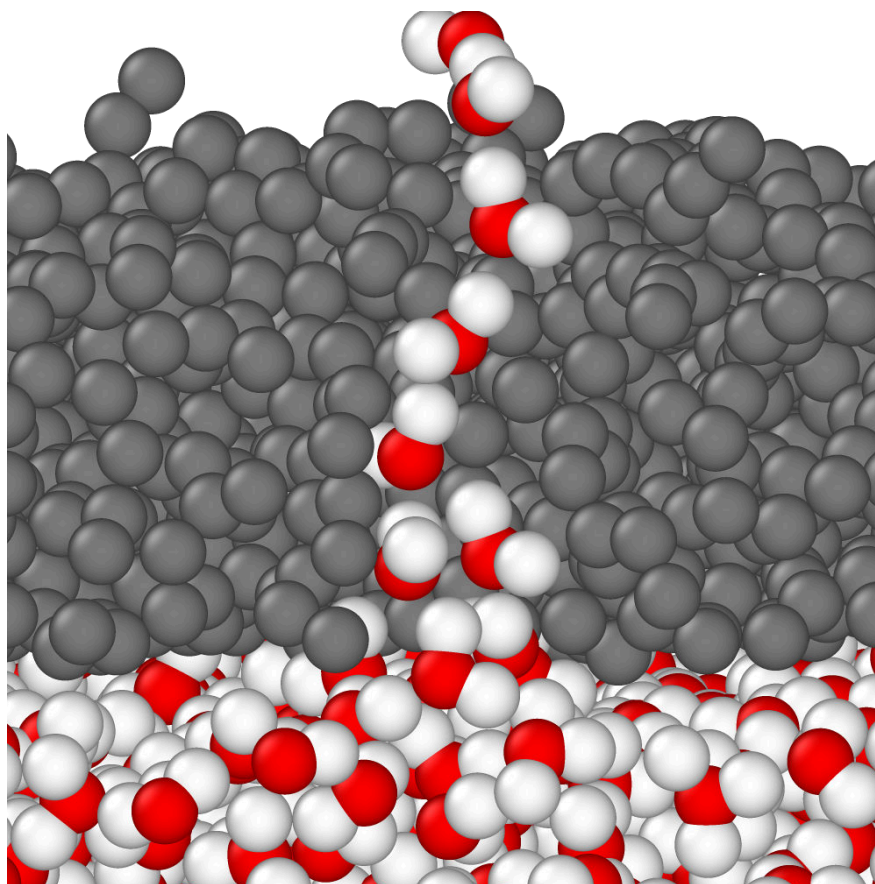
Figure 10.4.: Cross-sectional side view of a pore inside a CNM (gray spheres) showing single-file mode water (H_2O molecules depicted by white (H) and red (O) spheres) permeation.

timestep of the $2712 \cdot 10^{-15}$ s ≈ 2.7 ps long simulation a water molecule flows through this area, although hole size and topography from the top may suggest otherwise. Zooming in on these areas and tilting the view as shown in Fig. 10.7a and 10.7b indicates that flow of water molecules is not possible in this area as surrounding carbon atoms in the center of the membrane hinder the possibility of straight single-file mode flow. Tilting of the water molecules would diminish the single-file effect.
Overall, the porosity of the exemplary membrane seems much less pronounced than the real membranes with one hole up to 0.5 nm in diameter per nm^2 [17].
Nonetheless, the simulated membrane shows that water permeation is indeed possible and that the single-file mode is the key driving factor of the flow. The presented method allows for qualitative insights on the water permeation of porous carbon nanomembranes.

Pore identification might be improved to find arbitrarily formed channels inside a membrane. Since the permeation is sped up drastically by high pressure, direct comparison with quantitative experimental results, e.g. the number of water molecules permeating the membrane in a given time interval, is difficult, but possible when counting the water molecules in the simulation which would be a non-trivial improvement to the simulation setup.
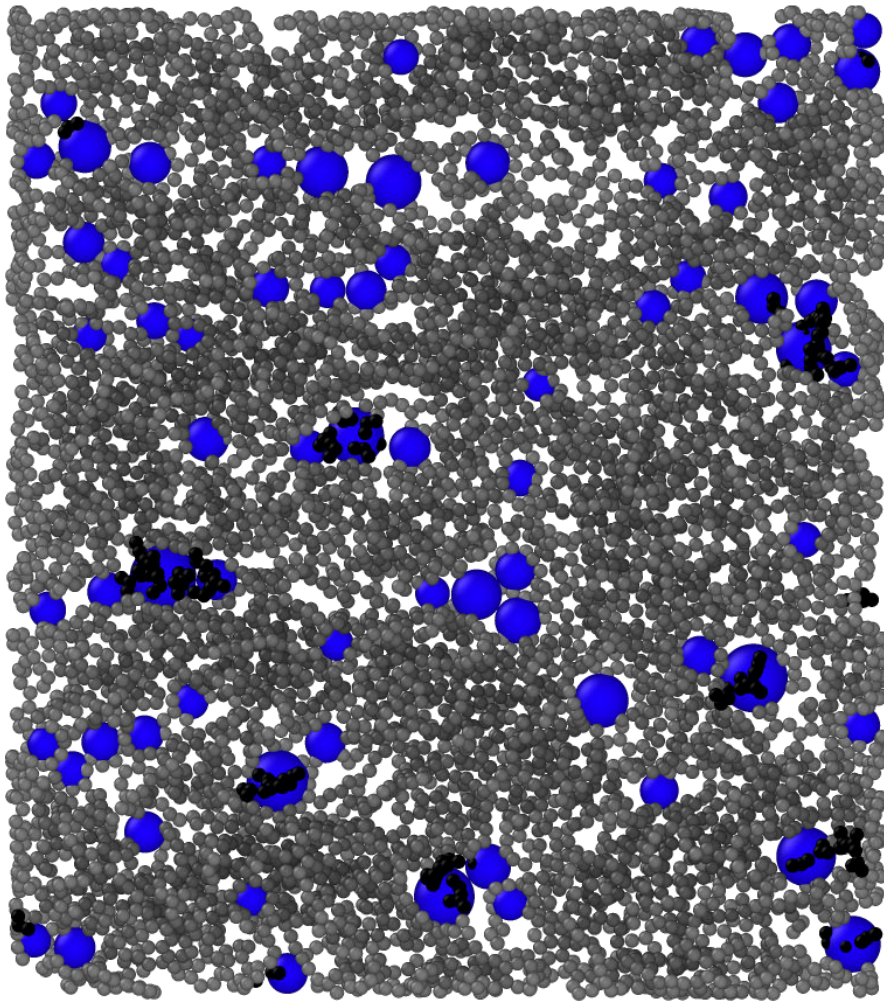
Figure 10.5.: Top view of single-file mode water (black spheres) permeation and approximation of holes visualized by blue spheres.
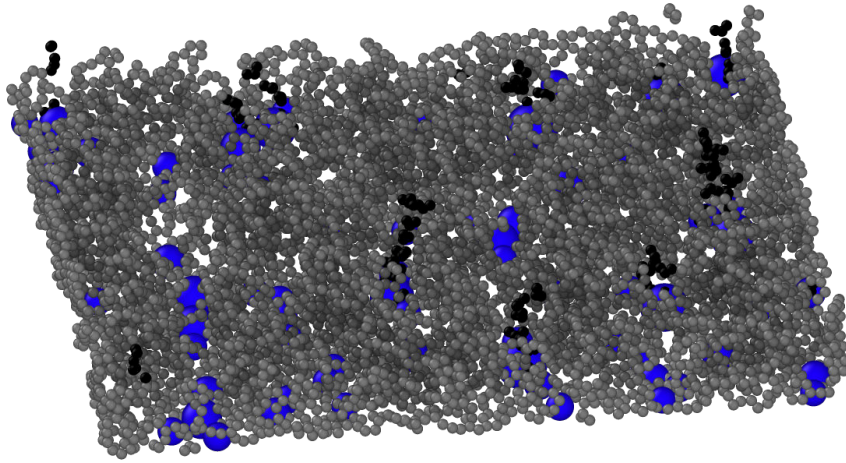
Figure 10.6.: Perspective view of single-file mode water (black spheres) permeation and approximation of holes visualized by blue spheres.
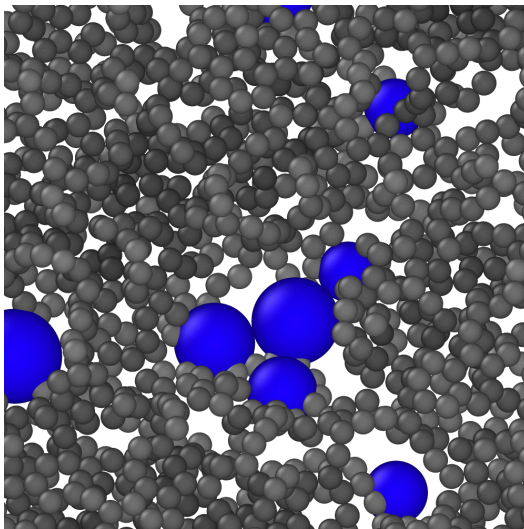
(a) Excluded region in the middle of the top view of the membrane.
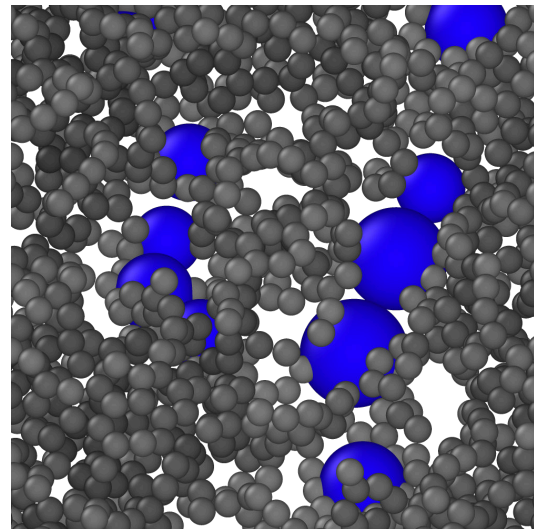
(b) Excluded region in the top of the top view of the membrane.

Figure 10.7.: Zoomed-in regions of porous areas not contributing to permeation.

11. Conclusions and outlook

The main goals were to create computer simulations of the process of CNM production and the characterization of resulting membranes by various means.

The model scenarios abstracting the experimental process considering the limitations of classical molecular dynamics have been shown to be in qualitative agreement with experiments. Some processes are closer to the experiment than others, e.g. the most violent approaches applying both vertical and lateral momentum transfer are able to produce better results with respect to the visual impression of the membrane with regards to its porosity.

Membranes have shown to be mechanically stable for both those created from traditional aromatic precursor SAMs and the recently demonstrated aliphatic SAMs.

This is a crucial step in understanding the internal structure of the membrane and possible molecular and atomic (sub-)processes involved.

Results fall short when it comes to reproducing the experimental value of the Young's modulus, which can be determined by various means, e.g. bulge testing or nanoindentation, to be at least an order of magnitude smaller than most molecular dynamics results. The dynamic linear elasticity methods performed overall better than the determination through the curvature of the potential energy with moduli much closer, but still too large by about a factor of 10...20, to the experimental values. The same holds for simulated nanoindentation results. The latter is especially limited by existing models to interpret the force-deflection data since only continuum approximations exist.

Overall, this is where the layers of abstraction play a big role. There are no hydrogen atoms and electrons present in the model system. Thus, breaking carbon-hydrogen bonds and momentum transfer by hydrogen atoms is neglected. Missing electrons limit the model to primary electron bombardment by simulated momentum transfer only, while some experimentalists assume secondary electrons to be the main cause of breaking and formation of bonds [125]. To simulate the effects of this assumption, an improvement to the model scenarios could be a sequential bond formation process, where bonds between carbon atoms are only allowed to form locally, while the dynamics of all other atoms is halted. All abstractions have to be made in order to be able to simulate a large enough and reasonably sized area of a membrane, keeping atom count such that simulations are first of all possible and completed in a reasonable timeframe. Other more accurate simulations, e.g. done by density functional theory (DFT) are limited to a few hundreds of atoms at most while introducing unwanted periodicity [44].

On the other hand, the molecular dynamics permeation studies carried out give a good qualitative impression of single-file modes of water molecules permeating the membrane. This characteristic is supported by hole distributions and artistic atomic force microscopy images. Compared to experimental results, the density and size of holes is not in agreement with the outstanding permeation properties of real membranes with one hole of up to 0.5 nm diameter per nm^2 [17]. To improve the permeation simulations to produce quantitative results, water molecules permeating the membrane

could be counted. However, due to the exaggerated pressure, the result would not be comparable to experiments.

High loss of aromaticity has also been shown to play a significant role in the experimental formation of CNMs in which broken bonds act as a glue in the cross-linking process [117]. Although formulated weaker than its original definition in chemistry, simulated aromaticity measurements by means of ring statistics are in qualitative agreement with the experiment.

For the topic of nanoindentation, further research has to be put in the models relating the Young's modulus to the force-indentation data which are often motivated by continuum properties in FEM simulations. The systems discussed in this thesis are nowhere close to the dimensions needed for continuum properties, which leaves all existing models as a crude approximation for molecular dynamics simulations.

Simulation of larger systems at the cost of computational expense would be an improvement for most simulations. However, this does not solve the problem of limited timescales reachable in molecular dynamics simulations and the necessity of exaggerating real-world scenarios to fit them in the available simulation times while maintaining physical meaningfulness.

Further large-scale statistics have to be made to draw conclusions with regard to finite-size effects. A Bachelor's thesis on the topics of membrane size and clamp size effects in stress-strain simulations as well as a different approach to hole detection was written by Mihlan on the basis of the methods developed for this thesis [145].

A different approach to membrane formation was developed by Marks and Vukovic within a framework of cooperation and discussed in private communications. It is based on randomly placed carbon atoms in a volume with exclusion cylinders forcing holes to form around.

Thus, the theoretical investigation of carbon nanomembranes is an ongoing research topic with improvements, new approaches and ideas to explore, e.g. by means of ion scattering experiments and simulations as performed by Wilhelm [146].

Statement of authorship

Hereby I assure, that the thesis at hand is written by myself and that I have not used any resources other than those that have been mentioned and appropriately marked, appearing in the bibliography for either direct or indirect citations, to the best of my belief. This thesis or any part of it, neither in this nor a similar form, has ever been submitted for another degree or diploma at any university or other institute of tertiary education. I am aware of the currently applicable examination regulations of the faculty of physics at the University of Bielefeld and confirm that no third parties have received either direct or indirect monetary benefits for work related to the submitted dissertation.
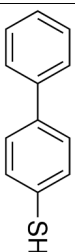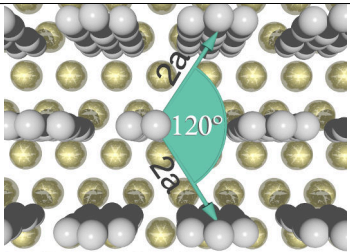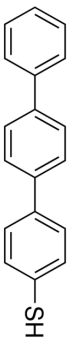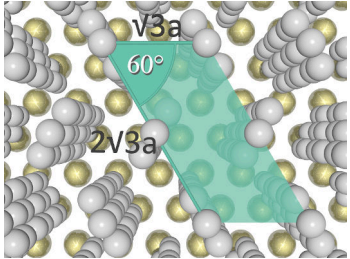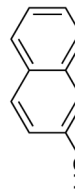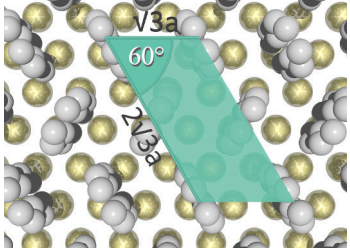
_____   _____
Place, Date   Signature

A. Appendix

A.1. Investigated aromatic precursor SAMs

Most of the simulations done for this thesis are based on self-assembled monolayers of the three experimentally favored precursor molecules. The following Tab. A.1 gives an overview over names, structural formulas, SAM structures and a visualization of the unit cell taken from Ref. [3] without rotation about γ being taken into account for simplicity.

Table A.1.: Structures of various self-assembled monolayers, taken from Ref. [3].

Name	Structural formula	SAM structure	Visualization
Biphenyl-4-thiol (BPT) 1,1'-Biphenyl-4-thiol 4-Biphenylthiol 4-Mercaptobiphenyl 4-Phenylbenzenethiol	[147]	(2×2) hexagonal, $\gamma = 30°$ [148] $\gamma = 15°$ [4] $\gamma = 20°$ [88] $\gamma = 20°$ [149] Mixture of: (2×2) structure, $(2\sqrt{3} \times 9)$ unit cell, $(2\sqrt{3} \times 8)$ unit cell [148]	
1,1',4',1''-Terphenyl-4-thiol (TPT)	[150]	$(\sqrt{3} \times \sqrt{3})$ structure $(2\sqrt{3} \times \sqrt{3})$ unit cell $\gamma = 20°$ [88]	
2-Naphthalenethiol (NPTH) 2-Naphthyl mercaptan Thio-2-naphthol (β)	[151]	$(\sqrt{3} \times \sqrt{3})$ structure $(2\sqrt{3} \times \sqrt{3})$ unit cell	

A.2. LAMMPS input scripts and tools

Molecular dynamics simulations have been performed with LAMMPS by Sandia Gov. [22]. In order to provide the possibility of reproduction of the presented results, the input scripts used to generate outputs like visualizations, atom coordinates and Young's moduli can be requested by e-mail from `dissertation@jehrens.de`. Input scripts are partly generated with other tools like moltemplate [140], VMD [138] and Pizza.py Toolkit [152]. Further post-processing configurations and scripts for Blender [139], Ovito [130], VMD [138] and PACKMOL [141] can be used to produce intermediate results and images found in this dissertation.

A digital copy of this thesis in PDF-format can be accessed via the University of Bielefeld PUB archive: `https://pub.uni-bielefeld.de/`.

List of Figures

List of Tables

Bibliography

[1] Julian Ehrens, Florian Gayk, Patrick Vorndamme, Tjark Heitmann, Niklas Biere, Dario Anselmetti, Xianghui Zhang, Armin Gölzhäuser, and Jürgen Schnack. Theoretical formation of carbon nanomembranes under realistic conditions using classical molecular dynamics. *Physical Review B*, 103(11):115416, 2021.

[2] Florian Gayk, Julian Ehrens, Tjark Heitmann, Patrick Vorndamme, Andreas Mrugalla, and Jürgen Schnack. Young's moduli of carbon materials investigated by various classical molecular dynamics schemes. *Physica E: Low-dimensional Systems and Nanostructures*, 99:215 – 219, 2018.

[3] Florian Gayk. Simulation von Kohlenstoff-Nanomembranen mittels klassischer Molekulardynamik unter Verwendung des „environment-dependent interaction potential". Master's thesis, Bielefeld University, 2018.

[4] W. Geyer, V. Stadler, W. Eck, M. Zharnikov, A. Gölzhäuser, and M. Grunze. Electron-induced crosslinking of aromatic self-assembled monolayers: Negative resists for nanolithography. *Applied Physical Letters*, 75:2401–2403, 1999.

[5] Andrey Turchanin. Graphene Growth by Conversion of Aromatic Self-Assembled Monolayers. *Annalen der Physik*, 529(11):1700168, 2017. 1700168.

[6] Carla de Tomas, Alireza Aghajamali, Jake L. Jones, Daniel J. Lim, Maria J. López, Irene Suarez-Martinez, and Nigel A. Marks. Transferability in interatomic potentials for carbon. *Carbon*, 155:624 – 634, 2019.

[7] Petr Dementyev, Timo Wilke, Daniil Naberezhnyi, Daniel Emmrich, and Armin Gölzhäuser. Vapour permeation measurements with free-standing nanomembranes. *Physical Chemistry Chemical Physics*, 21:15471–15477, 2019.

[8] Andreas Winter, Yasin Ekinci, Armin Gölzhäuser, and Andrey Turchanin. Free-standing carbon nanomembranes and graphene monolayers nanopatterned via EUV interference lithography. *2D Materials*, 6:021002, 2019.

[9] Zoran Jaksic and Olga Jaksic. Biomimetic Nanomembranes: An Overview. *Biomimetics*, 5:24, 2020.

[10] Andrey Turchanin, André Beyer, Christoph T. Nottbohm, Xianghui Zhang, Rainer Stosch, Alla Sologubenko, Joachim Mayer, Peter Hinze, Thomas Weimann, and Armin Gölzhäuser. One Nanometer Thin Carbon Nanosheets with Tunable Conductivity and Stiffness. *Advanced Materials*, 21:1233–1237, 2009.

[11] Polina Angelova, Henning Vieker, Nils-Eike Weber, Dan Matei, Oliver Reimer, Isabella Meier, Simon Kurasch, Johannes Biskupek, Dominik Lorbach, Katrin

Wunderlich, Long Chen, Andreas Terfort, Markus Klapper, Klaus Müllen, Ute Kaiser, Armin Gölzhäuser, and Andrey Turchanin. A Universal Scheme to Convert Aromatic Molecular Monolayers into Functional Carbon Nanomembranes. *ACS Nano*, 7:6489–6497, 2013.

[12] Andrey Turchanin and Armin Gölzhäuser. Carbon Nanomembranes. *Advanced Materials*, 28:6075–6103, 2016.

[13] Andreas Mrugalla and Jürgen Schnack. Classical molecular dynamics investigations of biphenyl-based carbon nanomembranes. *Beilstein Journal of Nanotechnology*, 5:865–871, 2014.

[14] Xianghui Zhang, Andre Beyer, and Armin Gölzhäuser. Mechanical characterization of carbon nanomembranes from self-assembled monolayers. *Beilstein Journal of Nanotechnology*, 2:826–833, 2011.

[15] Changgu Lee, Xiaoding Wei, Jeffrey W. Kysar, and James Hone. Measurement of the Elastic Properties and Intrinsic Strength of Monolayer Graphene. *Science*, 321:385–388, 2008.

[16] Raphael Dalpke. *Transport Behavior of Tailored Carbon Nanomembranes*. PhD thesis, Bielefeld University, 2020.

[17] Yang Yang, Petr Dementyev, Niklas Biere, Daniel Emmrich, Patrick Stohmann, Riko Korzetz, Xianghui Zhang, André Beyer, Sascha Koch, Dario Anselmetti, and Armin Gölzhäuser. Rapid Water Permeation Through Carbon Nanomembranes with Sub-Nanometer Channels. *ACS Nano*, 12(5):4695–4701, 2018. PMID: 29741359.

[18] Yang Yang, Roland Hillmann, Yubo Qi, Riko Korzetz, Niklas Biere, Daniel Emmrich, Michael Westphal, Björn Büker, Andreas Hütten, André Beyer, Dario Anselmetti, and Armin Gölzhäuser. Ultrahigh Ionic Exclusion through Carbon Nanomembranes. *Advanced Materials*, 32:1907850, 2020.

[19] Xianghui Zhang, Emanuel Marschewski, Paul Penner, Thomas Weimann, Peter Hinze, André Beyer, and Armin Gölzhäuser. Large-area all-carbon nanocapacitors from graphene and carbon nanomembranes. *ACS Nano*, 12(10):10301–10309, 2018.

[20] Andrey Turchanin, Daniel Käfer, Mohamed El-Desawy, Christof Wöll, Gregor Witte, and Armin Gölzhäuser. Molecular Mechanisms of Electron-Induced Cross-Linking in Aromatic SAMs. *Langmuir*, 25:7342–7352, 2009.

[21] Wolfgang Eck, Volker Stadler, Wolfgang Geyer, Michael Zharnikov, Armin Gölzhäuser, and Michael Grunze. Generation of Surface Amino Groups on Aromatic Self-Assembled Monolayers by Low Energy Electron Beams—A First Step Towards Chemical Lithography. *Advanced Materials*, 12(11):805–808, 2000.

[22] S. Plimpton. Fast Parallel Algorithms for Short-Range Molecular Dynamics. *Journal of Computational Physics*, 117:1–19, 1995. `http://lammps.sandia.gov`.

[23] N. A. Marks. Generalizing the environment-dependent interaction potential for carbon. *Physical Review B*, 63:035401, 2000.

[24] Jacob W. Martin, Carla de Tomas, Irene Suarez-Martinez, Markus Kraft, and Nigel A. Marks. Topology of Disordered 3D Graphene Networks. *Physical Review Letters*, 123:116105, 2019.

[25] Radu Iftimie, Peter Minary, and Mark E. Tuckerman. Ab initio molecular dynamics: Concepts, recent developments, and future trends. *Proceedings of the National Academy of Sciences*, 102(19):6654–6659, 2005.

[26] Weile Jia, Han Wang, Mohan Chen, Denghui Lu, Lin Lin, Roberto Car, Weinan E, and Linfeng Zhang. Pushing the Limit of Molecular Dynamics with Ab Initio Accuracy to 100 Million Atoms with Machine Learning. In *Proceedings of the International Conference for High Performance Computing, Networking, Storage and Analysis*, SC '20. IEEE Press, 2020.

[27] David Ceperley. Interatomic Potentials. `https://courses.physics.illinois.edu/phys466/fa2016/lnotes/pot.PDF`, 2016. [Accessed: 2021-09-17].

[28] Viktor Hornak, Robert Abel, Asim Okur, Bentley Strockbine, Adrian Roitberg, and Carlos Simmerling. Comparison of multiple Amber force fields and development of improved protein backbone parameters. *Proteins: Structure, Function, and Bioinformatics*, 65(3):712–725, 2006.

[29] William L Jorgensen, David S Maxwell, and Julian Tirado-Rives. Development and testing of the OPLS all-atom force field on conformational energetics and properties of organic liquids. *Journal of the American Chemical Society*, 118(45):11225–11236, 1996.

[30] J. Tersoff. New empirical approach for the structure and energy of covalent systems. *Physical Review B*, 37:6991–7000, 1988.

[31] Donald W. Brenner. Empirical potential for hydrocarbons for use in simulating the chemical vapor deposition of diamond films. *Physical Review B*, 42:9458–9471, Nov 1990.

[32] Steven J. Stuart, Alan B. Tutein, and Judith A. Harrison. A reactive potential for hydrocarbons with intermolecular interactions. *The Journal of Chemical Physics*, 112:6472–6486, 2000.

[33] José Fernando "Jfmelero" Melero. Orbital hybridisation sp. `https://en.wikipedia.org/wiki/File:AE2h.svg`, 2011. [Accessed: 2021-08-21].

[34] José Fernando "Jfmelero" Melero. Orbital hybridisation sp2. `https://en.wikipedia.org/wiki/File:AE3h.svg`, 2011. [Accessed: 2021-08-21].

[35] José Fernando "Jfmelero" Melero. Orbital hybridisation sp3. `https://en.wikipedia.org/wiki/File:AE4h.svg`, 2011. [Accessed: 2021-08-21].

[36] Donald W Brenner, Olga A Shenderova, Judith A Harrison, Steven J Stuart, Boris Ni, and Susan B Sinnott. A second-generation reactive empirical bond order (REBO) potential energy expression for hydrocarbons. *Journal of Physics: Condensed Matter*, 14:783, 2002.

[37] Albert P Bartók, Mike C Payne, Risi Kondor, and Gábor Csányi. Gaussian approximation potentials: The accuracy of quantum mechanics, without the electrons. *Physical Review Letters*, 104(13):136403, 2010.

[38] Raji Heyrovska. Atomic structures of graphene, benzene and methane with bond lengths as sums of the single, double and resonance bond radii of carbon. *arXiv preprint arXiv:0804.4086*, 2008.

[39] Carla de Tomas, Irene Suarez-Martinez, and Nigel A Marks. Graphitization of amorphous carbons: A comparative study of interatomic potentials. *Carbon*, 109:681–693, 2016.

[40] Daan Frenkel and Berend Smit, editors. *Understanding Molecular Simulation: From Algorithms to Applications.* Academic Press, Inc., Orlando, FL, USA, 1st edition, 1996.

[41] P. Bastian et al. High Performance Computing in Science and Engineering Garching/Munich 2018. `https://www.lrz.de/services/compute/supermuc/magazinesbooks/2018_SuperMUC-Results-Reports.pdf`, 2018. [Accessed: 2021-09-07].

[42] C.E. Shannon. Communication in the Presence of Noise. *Proceedings of the IRE*, 37(1):10–21, 1949.

[43] LAMMPS Documentation. boundary command. `https://docs.lammps.org/boundary.html`, 2021.

[44] Pepa Cabrera-Sanfelix, Andres Arnau, and Daniel Sanchez-Portal. First-principles investigation of electron-induced cross-linking of aromatic self-assembled monolayers on Au(111). *Physical Chemistry Chemical Physics*, 12:1578–1584, 2010.

[45] LAMMPS Documentation. fix nve command. `https://docs.lammps.org/fix_nve.html`. [Accessed: 2021-09-20].

[46] LAMMPS Documentation. fix nvt command. `https://docs.lammps.org/fix_nh.html`. [Accessed: 2021-09-20].

[47] LAMMPS Documentation. fix temp/berendsen command. `https://docs.lammps.org/fix_temp_berendsen.html`. [Accessed: 2021-09-20].

[48] LAMMPS Documentation. fix langevin command. `https://docs.lammps.org/fix_langevin.html`. [Accessed: 2021-09-20].

[49] LAMMPS Documentation. fix npt command. `https://docs.lammps.org/fix_nh.html#fix-npt-command`. [Accessed: 2021-09-17].

[50] LAMMPS Documentation. fix press/berendsen command. `https://docs.lammps.org/fix_press_berendsen.html`. [Accessed: 2021-09-20].

[51] LAMMPS Documentation. fix nph command. `https://docs.lammps.org/fix_nh.html#fix-nph-command`. [Accessed: 2021-09-17].

[52] Michael Griebel, Stefan Knapek, Gerhard Zumbusch, and Attila Caglar. *Numerische Simulation in der Moleküldynamik*. Springer, 2004.

[53] Alexy K. Mazur. Common Molecular Dynamics Algorithms Revisited: Accuracy and Optimal Time Steps of Störmer–Leapfrog Integrators. *Journal of Computational Physics*, 136(2):354–365, 1997.

[54] William C. Swope, Hans C. Andersen, Peter H. Berens, and Kent R. Wilson. A computer simulation method for the calculation of equilibrium constants for the formation of physical clusters of molecules: Application to small water clusters. *The Journal of Chemical Physics*, 76(1):637–649, 1982.

[55] Jules Jacobs. Leapfrog and Verlet are the same method. `https://julesjacobs.com/2019/03/15/leapfrog-verlet.html`, Mar 2019. [Accessed: 2021-08-28].

[56] Kerson Huang. *Statistical Mechanics*. Wiley, 2nd edition, 1991.

[57] R. K. Pathria. *Statistical Mechanics*. Butterworth Heinemann, 1972.

[58] H.J. Lüdde M. Keim. Kanonische Bewegungsgleichung - Hamiltons Formulierung. `https://itp.uni-frankfurt.de/~luedde/Lecture/Mechanik/Intranet/Skript/Kap8/node7.html`. [Accessed: 2021-09-30].

[59] Aidan P. Thompson, Steven J. Plimpton, and William Mattson. General formulation of pressure and stress tensor for arbitrary many-body interaction potentials under periodic boundary conditions. *The Journal of Chemical Physics*, 131(15):154107, 2009.

[60] Philippe H Hünenberger. Thermostat algorithms for molecular dynamics simulations. *Advanced Computer Simulation*, pages 105–149, 2005.

[61] H. J. C. Berendsen, J. P. M. Postma, W. F. van Gunsteren, A. DiNola, and J. R. Haak. Molecular dynamics with coupling to an external bath. *The Journal of Chemical Physics*, 81(8):3684–3690, 1984.

[62] Shuichi Nosé. A unified formulation of the constant temperature molecular dynamics methods. *The Journal of Chemical Physics*, 81(1):511–519, 1984.

[63] William G. Hoover and Brad Lee Holian. Kinetic moments method for the canonical ensemble distribution. *Physics Letters A*, 211(5):253–257, 1996.

[64] Cameron Abrams. Molecular Dynamics at Constant Pressure: The Berendsen Barostat. `http://www.pages.drexel.edu/~cfa22/msim/node36.html`. [Accessed: 2021-09-21].

[65] William G. Hoover. Canonical dynamics: Equilibrium phase-space distributions. *Physical Review A*, 31:1685, 1985.

[66] Hans C. Andersen. Molecular dynamics simulations at constant pressure and/or temperature. *The Journal of Chemical Physics*, 72(4):2384–2393, 1980.

[67] M. Parrinello and A. Rahman. Polymorphic transitions in single crystals: A new molecular dynamics method. *Journal of Applied Physics*, 52(12):7182–7190, 1981.

[68] Shuichi Nosé and M.L. Klein. Constant pressure molecular dynamics for molecular systems. *Molecular Physics*, 50(5):1055–1076, 1983.

[69] David Ceperley. Advanced molecular dynamics techniques. `https://sites.engineering.ucsb.edu/~shell/che210d/Advanced_molecular_dynamics.pdf`, 2019. [Accessed: 2021-09-17].

[70] Jin Zhang, Haiyang Zhang, Tao Wu, Qi Wang, and David van der Spoel. Comparison of Implicit and Explicit Solvent Models for the Calculation of Solvation Free Energy in Organic Solvents. *Journal of Chemical Theory and Computation*, 13(3):1034–1043, 2017. PMID: 28245118.

[71] Ramu Anandakrishnan, Aleksander Drozdetski, Ross C. Walker, and Alexey V. Onufriev. Speed of Conformational Change: Comparing Explicit and Implicit Solvent Molecular Dynamics Simulations. *Biophysical Journal*, 108(5):1153–1164, 2015.

[72] Yaoyi Chen, Andreas Krämer, Nicholas E. Charron, Brooke E. Husic, Cecilia Clementi, and Frank Noé. Machine learning implicit solvation for molecular dynamics. *The Journal of Chemical Physics*, 155(8):084101, Aug 2021.

[73] H. J. C. Berendsen, J. P. M. Postma, W. F. van Gunsteren, and J. Hermans. *Interaction Models for Water in Relation to Protein Hydration*, pages 331–342. Springer Netherlands, Dordrecht, 1981.

[74] Michael F. Harrach and Barbara Drossel. Structure and dynamics of TIP3P, TIP4P, and TIP5P water near smooth and atomistic walls of different hydroaffinity. *The Journal of Chemical Physics*, 140(17):174501, 2014.

[75] LAMMPS Documentation. pair_style hybrid command. `https://docs.lammps.org/pair_hybrid.html`. [Accessed: 2021-09-11].

[76] LAMMPS Documentation. compute pressure command. `https://docs.lammps.org/Howto_spc.html`. [Accessed: 2021-09-11].

[77] LAMMPS Documentation. TIP3P water model. `https://docs.lammps.org/Howto_tip3p.html`. [Accessed: 2021-09-11].

[78] LAMMPS Documentation. TIP4P water model. `https://docs.lammps.org/Howto_tip4p.html`. [Accessed: 2021-09-11].

[79] Yuriy Khalak, Björn Baumeier, and Mikko Karttunen. Improved general-purpose five-point model for water: TIP5P/2018. *The Journal of Chemical Physics*, 149(22):224507, 2018.

[80] K. Hahn and J. Kärger. Molecular Dynamics Simulation of Single-File Systems. *The Journal of Physical Chemistry*, 100(1):316–326, 1996.

[81] B. Lee and F.M. Richards. The interpretation of protein structures: Estimation of static accessibility. *Journal of Molecular Biology*, 55(3):379–IN4, 1971.

[82] Benedetta Mennucci. Polarizable continuum model. *Wiley Interdisciplinary Reviews: Computational Molecular Science*, 2(3):386–404, 2012.

[83] Maria G. Fyta, Simone Melchionna, Efthimios Kaxiras, and Sauro Succi. Multiscale Coupling of Molecular Dynamics and Hydrodynamics: Application to DNA Translocation through a Nanopore. *Multiscale Modeling & Simulation*, 5(4):1156–1173, Jan 2006.

[84] Xianghui Zhang, Christof Neumann, Polina Angelova, André Beyer, and Armin Gölzhäuser. Tailoring the Mechanics of Ultrathin Carbon Nanomembranes by Molecular Design. *Langmuir*, 30(27):8221–8227, 2014. PMID: 24946144.

[85] Wolfgang Eck, Alexander Küller, Michael Grunze, Berthold Völkel, and Armin Gölzhäuser. Freestanding nanosheets from crosslinked biphenyl self-assembled monolayers. *Advanced Materials*, 17(21):2583–2587, 2005.

[86] Petr Dementyev, Daniil Naberezhnyi, Michael Westphal, Manfred Buck, and Armin Gölzhäuser. Carbon Nanomembranes from Aromatic Carboxylate Precursors. *ChemPhysChem*, 21(10):1006, 2020.

[87] W.N. Unertl. Chapter 1 - Surface Crystallography. In W.N. Unertl, editor, *Physical Structure*, volume 1 of *Handbook of Surface Science*, pages 3–49. North-Holland, 1996.

[88] S. Frey, V. Stadler, K. Heister, W. Eck, M. Zharnikov, M. Grunze, B. Zeysing, and A. Terfort. Structure of Thioaromatic Self-Assembled Monolayers on Gold and Silver. *Langmuir*, 17(8):2408–2415, 2001.

[89] S Rousset, V Repain, G Baudot, Y Garreau, and J Lecoeur. Self-ordering of Au(111) vicinal surfaces and application to nanostructure organized growth. *Journal of Physics: Condensed Matter*, 15(47):S3363, 2003.

[90] Andrey Turchanin, André Beyer, Christoph T. Nottbohm, Xianghui Zhang, Rainer Stosch, Alla Sologubenko, Joachim Mayer, Peter Hinze, Thomas Weimann, and Armin Gölzhäuser. One Nanometer Thin Carbon Nanosheets with Tunable Conductivity and Stiffness. *Advanced Materials*, 21(12):1233–1237, 2008.

[91] Armin Gölzhäuser. Discussion on CNMs from aliphatic molecules. Personal communication.

[92] André Beyer, Henning Vieker, Robin Klett, Hanno Meyer zu Theenhausen, Polina Angelova, and Armin Gölzhäuser. Imaging of carbon nanomembranes with helium ion microscopy. *Beilstein Journal of Nanotechnology*, 6(1):1712–1720, 2015.

[93] E. Hernández, C. Goze, P. Bernier, and A. Rubio. Elastic Properties of C and $B_x C_y N_z$ Composite Nanotubes. *Physical Review Letters*, 80:4502–4505, May 1998.

[94] Claude A. Klein and Gregory F. Cardinale. Young's modulus and Poisson's ratio of CVD diamond. *Diamond and Related Materials*, 2:918 – 923, 1993.

[95] André Beyer, Christoph Nottbohm, Alla Sologubenko, Inga Ennen, Andreas Hütten, Harald Rösner, Joachim Mayer, and Armin Gölzhäuser. Novel carbon nanosheets as support for ultrahigh resolution structural analysis of nanoparticles. In Martina Luysberg, Karsten Tillmann, and Thomas Weirich, editors, *EMC 2008 14th European Microscopy Congress 1–5 September 2008, Aachen, Germany*, pages 803–804, Berlin, Heidelberg, 2008. Springer Berlin Heidelberg.

[96] Martin Kind. IRRAS. `https://www.uni-frankfurt.de/53623116/Infrarot_Reflexions_Absorptions_Spektroskopie`. [Accessed: 2021-08-28].

[97] Peter Hollins. *Infrared Reflection–Absorption Spectroscopy*. American Cancer Society, 2006.

[98] Li Cui, Holly J Butler, Pierre L Martin-Hirsch, and Francis L Martin. Aluminium foil as a potential substrate for ATR-FTIR, transflection FTIR or Raman spectrochemical analysis of biological specimens. *Analytical Methods*, 8(3):481–487, 2016.

[99] E. B. Wilson, J. C. Decius, P. C. Cross, and Benson R. Sundheim. Molecular Vibrations: The Theory of Infrared and Raman Vibrational Spectra. *Journal of The Electrochemical Society*, 102(9):235C, 1955.

[100] Martin Thomas, Martin Brehm, Reinhold Fligg, Peter Vöhringer, and Barbara Kirchner. Computing vibrational spectra from ab initio molecular dynamics. *Physical Chemistry Chemical Physics*, 15:6608–6622, 2013.

[101] M. Brehm, M. Thomas, S. Gehrke, and B. Kirchner. TRAVIS—A free analyzer for trajectories from molecular simulation. *The Journal of Chemical Physics*, 152(16):164105, 2020.

[102] Florian Gayk. Discussion on simulated IR spectra. Personal communication.

[103] Matthew S Joens, Chuong Huynh, James M Kasuboski, David Ferranti, Yury J Sigal, Fabian Zeitvogel, Martin Obst, Claus J Burkhardt, Kevin P Curran, Sreekanth H Chalasani, et al. Helium Ion Microscopy (HIM) for the imaging of biological samples at sub-nanometer resolution. *Scientific reports*, 3(1):1–7, 2013.

[104] Joseph I. Goldstein, Dale E. Newbury, Patrick Echlin, David C. Joy, Charles E. Lyman, Eric Lifshin, Linda Sawyer, and Joseph R. Michael. *The SEM and Its Modes of Operation*, pages 21–60. Springer US, Boston, MA, 2003.

[105] Henning Vieker, Natalie Frese, and Armin Gölzhäuser. Das Heliumionen-Mikroskop. *Physik in unserer Zeit*, 46:168–173, 07 2015.

[106] Hylke Akkerman and Bert Boer. TOPICAL REVIEW: Electrical conduction through single molecules and self-assembled monolayers. *Journal of Physics-condensed Matter - J PHYS-CONDENS MATTER*, 20, 01 2008.

[107] Roghayeh Ghasempour and Hamid Narei. 1 - CNT Basics and Characteristics. In Roham Rafiee, editor, *Carbon Nanotube-Reinforced Polymers*, Micro and Nano Technologies, pages 1–24. Elsevier, 2018.

[108] C.N.R. Rao and Kanishka Biswas. Characterization of Nanomaterials by Physical Methods. *Annual Review of Analytical Chemistry*, 2(1):435–462, 2009. PMID: 20636070.

[109] Min Ai, S. Shishatskiy, J. Wind, Xianghui Zhang, Christoph T. Nottbohm, Nils Mellech, A. Winter, H. Vieker, J. Qiu, K. Dietz, A. Gölzhäuser, and A. Beyer. Carbon nanomembranes (CNMs) supported by polymer: mechanics and gas permeation. *Advanced Materials*, 26 21:3421–6, 2014.

[110] M. Aliofkhazraei and N. Ali. 7.09 - AFM Applications in Micro/Nanostructured Coatings. In Saleem Hashmi, Gilmar Ferreira Batalha, Chester J. Van Tyne, and Bekir Yilbas, editors, *Comprehensive Materials Processing*, pages 191–241. Elsevier, Oxford, 2014.

[111] James R. Chelikowsky, Dingxin Fan, Alex J. Lee, and Yuki Sakai. Simulating noncontact atomic force microscopy images. *Physical Review Materials*, 3:110302, Nov 2019.

[112] Shohei Ogura and Katsuyuki Fukutani. Thermal Desorption Spectroscopy. In The Surface Science Society of Japan, editor, *Compendium of Surface and Interface Analysis*, pages 719–724. Springer Singapore, Singapore, 2018.

[113] Claudia Prosenjak, Ana-Maria Banu, Alistair D. Gellan, and Tina Düren. Hydrogen thermal desorption spectra: insights from molecular simulation. *Dalton Transactions*, 41:3974–3984, 2012.

[114] Fred A. Stevie and Carrie L. Donley. Introduction to X-ray photoelectron spectroscopy. *Journal of Vacuum Science & Technology A*, 38(6):063204, 2020.

[115] Polina Angelova and Armin Gölzhäuser. Carbon Nanomembranes. *Physical Sciences Reviews*, 2(3):20160105, 2017.

[116] Joachim Stöhr. *NEXAFS Spectroscopy*. Springer Nature, 1996.

[117] L. Amiaud, J. Houplin, M. Bourdier, V. Humblot, R. Azria, C.-M. Pradier, and A. Lafosse. Low-energy electron induced resonant loss of aromaticity: consequences on cross-linking in terphenylthiol SAMs. *Physical Chemistry Chemical Physics*, 16:1050–1059, 2014.

[118] Horst Conrad and Martin E. Kordesch. High Resolution Electron Energy Loss Spectroscopy, Applications. In John C. Lindon, George E. Tranter, and David W. Koppenaal, editors, *Encyclopedia of Spectroscopy and Spectrometry (Third Edition)*, pages 47–57. Academic Press, Oxford, third edition edition, 2017.

[119] Xianghui Zhang and André Beyer. Mechanics of free-standing inorganic and molecular 2D materials. *Nanoscale*, 13:1443–1484, 2021.

[120] JJ Vlassak and WD Nix. A new bulge test technique for the determination of Young's modulus and Poisson's ratio of thin films. *Journal of Materials Research*, 7(12):3242–3249, 1992.

[121] Sukky Jun, Tenzin Tashi, and Harold S Park. Size dependence of the nonlinear elastic softening of nanoscale graphene monolayers under plane-strain bulge tests: A molecular dynamics study. *Journal of Nanomaterials*, 2011, 2011.

[122] Xianghui Zhang, Emanuel Marschewski, Paul Penner, André Beyer, and Armin Gölzhäuser. Investigation of electronic transport through ultrathin carbon nanomembrane junctions by conductive probe atomic force microscopy and eutectic Ga–In top contacts. *Journal of Applied Physics*, 122(5):055103, 2017.

[123] Asif Bashir, Waleed Azzam, Michael Rohwerder, and Andreas Terfort. Polymorphism in Self-Assembled Terphenylthiolate Monolayers on Au(111). *Langmuir*, 29(44):13449–13456, 2013. PMID: 24083467.

[124] M.A. Khusenov, E.B. Dushanov, Kh.T Kholmurodov, M.M. Zaki, and N.H. Sweilam. On Correlation Effect of the Van-der-Waals and Intramolecular Forces for the Nucleotide Chain - Metallic Nanoparticles - Carbon Nanotube Binding. *The Open Biochemistry Journal*, 10:17–26, 2016.

[125] Xianghui Zhang, Henning Vieker, André Beyer, and Armin Gölzhäuser. Fabrication of carbon nanomembranes by helium ion beam lithography. *Beilstein Journal of Nanotechnology*, 5(1):188–194, 2014.

[126] LAMMPS Documentation. Example scripts. `https://lammps.sandia.gov/doc/Examples.html`. [Accessed: 2021-08-04].

[127] Mark A. Tschopp. LAMMPS tutorials for Beginners. `https://github.com/mrkllntschpp/lammps-tutorials`. [Accessed: 2021-09-11].

[128] Thomas Williams, Colin Kelley, and many others. Gnuplot 5.2: an interactive plotting program. `http://gnuplot.sourceforge.net/`, July 2020.

[129] LAMMPS Documentation. compute stress/atom command. `https://docs.lammps.org/compute_stress_atom.html`. [Accessed: 2021-09-17].

[130] Alexander Stukowski. Visualization and analysis of atomistic simulation data with OVITO – the Open Visualization Tool. *Modelling and Simulation in Materials Science and Engineering*, 18:015012, 2010.

[131] LAMMPS-Mailing list. [lammps-users] Fluctuations in Stress - Young's Modulus. `https://sourceforge.net/p/lammps/mailman/message/36945415/`. [Accessed: 2021-09-17].

[132] Filip Vukovic. Discussion on molecular dynamics best practices for elasticity, ring statistics and general dynamics. Personal communication.

[133] J. Christopher Love, Lara A Estroff, Jennah K. Kriebel, Ralph G. Nuzzo, and George M. Whitesides. Self-assembled monolayers of thiolates on metals as a form of nanotechnology. *Chemical Reviews*, 105(4):1103–1170, 2005.

[134] Carla de Tomas, Irene Suarez-Martinez, and Nigel A. Marks. Graphitization of amorphous carbons: A comparative study of interatomic potentials. *Carbon*, 109:681 – 693, 2016.

[135] LAMMPS Documentation. fix indent command. `https://docs.lammps.org/fix_indent.html`. [Accessed: 2021-09-17].

[136] Xianghui Zhang. *Mechanical Characterization of Carbon Nanosheets*. PhD thesis, Bielefeld University, 2010.

[137] Tadeusz Marek Krygowski and H. Szatylowicz. Aromaticity: What does it mean? *ChemTexts*, 1(3):1–10, 2015.

[138] William Humphrey, Andrew Dalke, and Klaus Schulten. VMD – Visual Molecular Dynamics. *Journal of Molecular Graphics*, 14:33–38, 1996.

[139] Blender Online Community. *Blender - a 3D modelling and rendering package*. Blender Foundation, Stichting Blender Foundation, Amsterdam, 2020.

[140] Andrew I. Jewett, David Stelter, Jason Lambert, Shyam M. Saladi, Otello M. Roscioni, Matteo Ricci, Ludovic Autin, Martina Maritan, Saeed M. Bashusqeh, Tom Keyes, Remus T. Dame, Joan-Emma Shea, Grant J. Jensen, and David S. Goodsell. Moltemplate: A Tool for Coarse-Grained Modeling of Complex Biological Matter and Soft Condensed Matter Physics. *Journal of Molecular Biology*, 433(11):166841, 2021. Computation Resources for Molecular Biology.

[141] Leandro Martínez, Ricardo Andrade, Ernesto G Birgin, and José Mario Martínez. PACKMOL: a package for building initial configurations for molecular dynamics simulations. *Journal of Computational Chemistry*, 30(13):2157–2164, 2009.

[142] R. Saito, R. Matsuo, T. Kimura, G. Dresselhaus, and M.S. Dresselhaus. Anomalous potential barrier of double-wall carbon nanotube. *Chemical Physics Letters*, 348(3):187–193, 2001.

[143] Kerstin Falk, Felix Sedlmeier, Laurent Joly, Roland R. Netz, and Lydéric Bocquet. Molecular Origin of Fast Water Transport in Carbon Nanotube Membranes: Superlubricity versus Curvature Dependent Friction. *Nano Letters*, 10(10):4067–4073, 2010. PMID: 20845964.

[144] Patrick Vorndamme. Discussion on brute-force hole searching algorithms. Personal communication.

[145] Levin Mihlan. Kohlenstoff-Nanomembranen: Analyse von Lochverteilungen und Untersuchungen von finite-size-Effekten bei Bestimmung des Elastizitätsmoduls. Bachelor's thesis, Bielefeld University, 2021.

[146] Richard Wilhelm. On the highly charged ion transmission spectroscopy applied to 2D materials. *Journal of Physics: Conference Series*, 1412:062010, 01 2020.

[147] Sigma-Aldrich. Biphenyl-4-thiol. `https://www.sigmaaldrich.com/catalog/product/aldrich/752207`. [Accessed 2018-08-28].

[148] D. G. Matei, H. Muzik, A. Gölzhäuser, and A. Turchanin. Structural Investigation of 1,1'-Biphenyl-4-thiol Self-Assembled Monolayers on Au(111) by Scanning Tunneling Microscopy and Low-Energy Electron Diffraction. *Langmuir*, 28(39):13905–13911, 2012. PMID: 22953697.

[149] Georg Heimel, Lorenz Romaner, Jean-Luc Brédas, and Egbert Zojer. Odd-Even Effects in Self-Assembled Monolayers of ω-(Biphenyl-4-yl)alkanethiols: A First-Principles Study. *Langmuir*, 24(2):474–482, 2008. PMID: 18072797.

[150] Sigma-Aldrich. 1,1',4',1"-Terphenyl-4-thiol. `https://www.sigmaaldrich.com/catalog/product/aldrich/708488`. [Accessed 2018-08-28].

[151] Sigma-Aldrich. 2-Naphthalenethiol. `https://www.sigmaaldrich.com/catalog/product/aldrich/270849`. [Accessed 2018-08-28].

[152] Steve Plimpton. *Pizza.py Toolkit — analysis/plotting/viz for LAMMPS, Chem-Cell, SPPARKS, SPARTA, GPL license.* Sandia National Laboratories, 2020.